DIFFERENTIAL CROSS SECTION FOR THE NEUTRON-INDUCED DEUTERON BREAKUP REACTION AT E_n = 13.0 MeV

by

Henry Rossignol Setze III

Department of Physics
Duke University

Date: July 22, 1994

Approved:

Calvin R. Howell
Calvin R. Howell, Supervisor

Robert P. Behringer
Robert P. Behringer

N. Russell Roberson
N. Russell Roberson

Roxanne P. Springer
Roxanne P. Springer

Henry R. Weller
Henry R. Weller

Dissertation submitted in partial fulfillment of
the requirements for the degree of Doctor
of Philosophy in the Department of
Physics in the Graduate School
of Duke University

1994

DIFFERENTIAL CROSS SECTION FOR THE NEUTRON-INDUCED DEUTERON BREAKUP REACTION AT $E_n = 13.0$ MeV

by

Henry Rossignol Setze III

The discrepancy between low-energy neutron-deuteron (nd) breakup cross-section data and calculations which include only nucleon-nucleon (NN) interactions has been cited as a possible signature of three-nucleon force (3NF) effects. Because 3NF effects are expected to be strongly dependent on the geometrical arrangement of the three particles in the exit channel, it may be possible to choose kinematic configurations in the breakup reaction which are sensitive to these effects. The "star" and "collinear" configurations are expected to exhibit this sensitivity. In a star configuration the three outgoing particles have momenta equal in magnitude and separated by 120° in the center-of-mass system. For the "space-star" configuration, the plane of the star is perpendicular to the incident beam direction and for the "coplanar-star" configuration the incident beam direction lies in the plane of the star. In a collinear configuration one of the particles in the exit channel is at rest in the center-of-mass system and the other two particles exit in opposite directions with equal momenta. The space-star configuration is particularly well-suited for this type of study because it has been shown to have only a modest sensitivity to the details of the NN potential.

Because these results are important to understanding the size of the effects to be expected from a 3NF, we have measured the nd breakup differential cross section at 13.0 MeV for the space star, coplanar star and two collinear configurations to a statistical accuracy of about ±5% for 0.5 MeV bins along the kinematic locus. All measurements were performed at the Triangle Universities Nuclear Laboratory using a shielded neutron source. The 13 MeV neutrons were produced using the ^{2}H(d,n)^{3}He reaction initiated with a dc deuteron beam incident on a 3-cm long cell filled with 7.8 atmospheres absolute of deuterium gas. The scatterer was a 4-cm diameter × 6-cm high C_6D_{12} liquid deuterated scintillator (NE-232). The neutrons were detected with

an array of eleven liquid scintillators. All three emitted particles were detected to kinematically over-determine the reaction. Simultaneous measurement of nd elastic scattering provided the absolute normalization of the breakup cross section.

The experiment was simulated via the Monte-Carlo method to determine the correction for attenuation of the scattered neutron flux. The absolute neutron detection efficiencies for the eleven liquid scintillators were obtained from an independent measurement. No attempt was made to extract a point-geometry cross section from our data by correcting for the finite geometry effects of the experimental setup. Instead the theoretical calculations using the Bonn-B OBEPQ were performed over the finite geometry of the experiment. The data and calculations were then identically projected onto the point-geometry kinematic locus for comparison.

The cross section for the space-star configuration was found to be $\sim$20% higher than calculations using the Bonn-B OBEPQ. These results were consistent with a previous measurement at this energy (Sträte, et al., Nuclear Physics **A508**, 1989). The cross section for each of the collinear configurations was found to be in good agreement with the Bonn-B calculations and did not exhibit the structure obtained from the previous measurement. Due to difficulties involved in detecting the very low energy protons at the coplanar star point, only a portion of the kinematically allowed cross section was obtained. These data were in reasonable agreement with the Bonn-B calculation and were considerably lower than the previous measurement. These results indicate that only two-nucleon forces are needed to describe the collinear configurations while the star configurations suggest 3NFs are needed. Further theoretical studies are necessary before firm conclusions can be drawn regarding the role of 3NF effects in the nd breakup reaction.

ACKNOWLEDGEMENTS

I am indebted to many people for their help in this work. First and foremost I wish to thank my adviser, Dr. Calvin Howell. His enthusiasm never wavered despite various setbacks along the way and his humor helped to overcome these obstacles. Dr. Werner Tornow spent many months writing the Monte-Carlo simulation for this experiment. Without this contribution, this work would have been impossible. He was also a valuable resource for me for all aspects of nuclear physics. The theoretical calculations which were performed for comparison to the experimental results were provided by Dr. Henryk Witała. He also provided some valuable discussions about three-body forces. In order to know accurately the size of our deuterium target, Dr. Carey Floyd was kind enough to take the time to x-ray the target and analyze the results. Many of the visitors to TUNL also provided some assistance on this undertaking and so I would like to thank Dr. Ivo Ŝlaus, Dr. Jim Lambert, Dr. Ahmed Hussein and Dr. Gerulf Mertens.

A nuclear physics experiment is a group effort. I would like to thank the other members of the neutron-time-of-flight group, Dr. Richard Walter, Dr. John Hanly, Dr. Paul Felsher, Dr. Gary Weisel, Dr. Mohammed Al-Ohali, Dr. Mahmud Nagadi, Richard Braun, Frank Salinas, Chris Roper, Dinko Gonzalez and Dr. Branko Vlahovic for the effort they made to help me along the way. The technical support staff at TUNL also deserves recognition for their contributions in maintaining and operating the lab: Paul Carter for keeping the accelator and the associated equipment together, and Sidney Edwards and Patrick Mulkey for designing and maintaining the electronic components in the lab. I also wish to thank the rest of the faculty and staff at TUNL for their help and consideration, in particular, Chris Keith and Paul Huffman, who gave me an office to myself every day at 5 p.m.

Recreation is also of tremendous importance in graduate school. For that reason I feel it is necessary to thank the many people who helped to make my time here enjoyable. Although they are too numerous to name, I want to thank all the people who over the years contributed to our departmental IM teams in softball, volleyball and basketball. I would also like to thank all the members of the "Hell Table" (and the staff at Satisfaction's who put up with us) for bizarre conversations and hours of euchre. My most entertaining hours away from the Physics Department were spent at the Hideaway. It was made entertaining by the people I met from different parts

of the university. Many of these people have been very good friends when I needed friends. So I offer a special salute to Dr. Lee Jones, Steve Aubochon, Bill "G" Kramer, Laura Coltrane, Allison Aschman, Leo Bass, Jay Baruch and Daniel Graham. One more select group must be mentioned by name. They seem to fall into most of these categories and therefore were present throughout most of the interesting parts of my graduate studies. Thank you very much Richard Braun, Dr. Bob Chasteler (Bobber), Dr. Dave Clarkson (Harley Dave), Dr. Zandy Williams (Zanj), Keener Hughen, Brett Hooper (Dad), Rick Leone, Dr. Zeid Ayre and Bobo (Jeff Olafsen) for all the laughter we have shared over the years.

Finally, I would like to thank my family. Although they have never fathomed my interest in physics, nor completely understood what my research entailed, they have been unflagging in their moral support throughout my education.

Contents

List of Figures

List of Tables

Chapter 1

Introduction

Low-energy nuclear physics is generally described by the non-relativistic Schrödinger equation employing nucleon-nucleon (NN) potentials. The potentials which most realistically model the NN interaction are based on meson-exchange theory. These semi-phenomonological potentials reproduce the experimental NN data for bound states and scattering states very well. The next test of these potentials is the three nucleon (3N) system. Tests in the 3N system are important for several reasons:

- it provides a measure of the off-energy-shell NN interaction;
- some 3N observables are more sensitive to parts of the NN interaction than 2N observables [How88];
- it is the simplest system in which three-nucleon forces can be studied.

The agreement between rigorous neutron-deuteron (nd) calculations (see Chap. 4) which use meson-exchange based NN potentials to describe the dynamics of the underlying 2N subsystems, and 3N data is impressive [Glö90]. However there are some serious discrepancies between data and calculations (see Table 1.1). The most obvious difficulty is their inability to reproduce the triton binding energy. It has been demonstrated [Gib88] that both the point-nucleon ^{3}H rms radius and the doublet nd scattering length ($^2a_{nd}$) scale with the binding energy. The major possible causes of these discrepancies are threefold.

Potential Model	^{3}H B.E. (MeV)	^{3}H $\langle r^2 \rangle^{\frac{1}{2}}$ (fm)	$^2a_{nd}$ (fm)	Reference
RSC	7.35	1.67	1.76	[Day81]
SSCC	7.53	1.68	1.32	[deT73]
AV14	7.67	1.67	1.35	[Wir84]
Bonn-B	8.13	–	–	[Mac89]
Paris	7.64	1.66	–	[Lac80]
experiment	8.48(2)	1.61(6)	0.65(4)	

Table 1.1: Calculations of the triton binding energy, point-nucleon ^{3}H radius, and the doublet nd scattering length for four NN potential models in a 34-channel approximation in comparison to experiment. RSC = Reid Soft Core, SSCC = Super-Soft-Core C, AV14 = Argonne V14. The experimental value for the triton binding energy is from [Gib88], the rms radius is from [Mar86] and the doublet nd scattering length is from [Dil71].

1. Three-nucleon forces (3NF) are not accounted for in the calculations. Such forces depend on the simultaneous positions and momenta of the three interacting particles when only nucleon degrees-of- freedom are considered,

2. Relativistic corrections are non-neglible,

3. The off-energy-shell behavior of the NN force is not correctly described by the NN potentials.

These three categories are not in any way distinct and in many cases cannot be separated. There is still much debate as to whether these are the only causes of the discrepancies. For example, calculations made with the Bonn-A one-boson-exchange-potential (OBEPQ) reproduces the triton binding energy fairly well. This is presumably due to the weaker than usual tensor force of this potential (4.4% D-state probability for the deuteron from the Bonn-A potential versus 5.8% for the D-state probability from the Paris potential [Glö90]).

The long-range part of the NN interaction is well described by a one-pion-exchange potential. Groups which attempt to construct a model for 3NF then assume that the long-range part of the 3NF will be approximated by a two-pion-exchange. Because the Δ- isobar dominates πN scattering below 300 MeV, it is assumed to be the

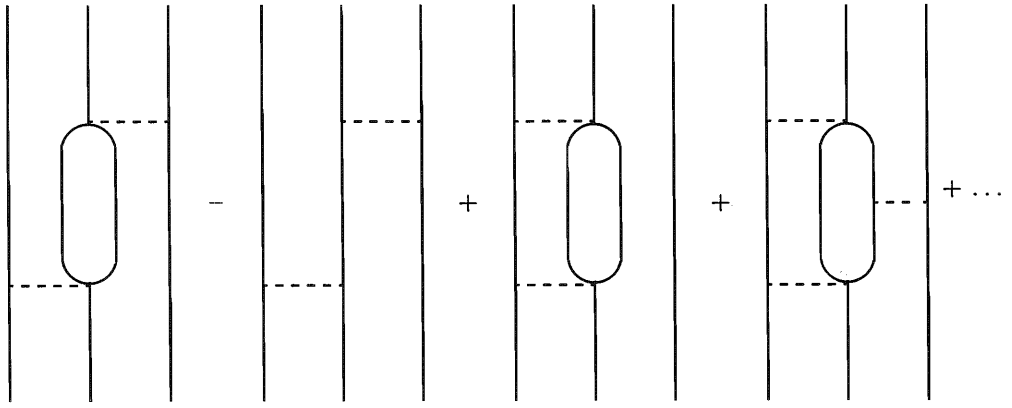

Figure 1.1: Multi-pion-exchange contributions to the 3NF. The first term is the Δ-isobar contribution to the 3NF. The second term represents the subtraction of the iterated two-nucleon force to prevent double counting. The third term assumes that Δ degrees- of-freedom are not included in the 2N force and the fourth term is the inclusion of a missing term (the NΔ interaction) due to the truncation to at most one pion exchange.

dominant term in the 3NF. Figure 1.1 shows the expansion of the multi-pion-exchange contributions to the 3NF as assumed in the Hannover group's model of the 3NF [Sau86]. It has recently been shown [Pic92] that this simple model does not have much affect on the triton binding energy due to cancellation between the repulsive Δ dispersive effects in the 2N force and attractive Δ 3NF effects. Because the three-nucleon bound states provide only limited information on these effects, it is necessary to turn to three-nucleon scattering observables to obtain more information.

Calculations are critical in the interpretation of data from 3N scattering experiments. Rigorous calculations for nucleon-deuteron elastic scattering and breakup using short range NN potentials in non-relativistic Hamiltonians can be made to a numerical accuracy of $\sim$1% [Wit88b, Wit89a, Fri90]. These calculations assume charge symmetry for all NN angular momentum states and charge independence for states with $l \geq 1$. The latest calculations use realistic NN potentials based on a meson-exchange theory. However, the Coulomb force has not yet been included in an exact way due to the long range nature of the force. For meaningful comparisons between calculations and data at low energies nd scattering data must be used rather than proton-deuteron (pd) scattering data.

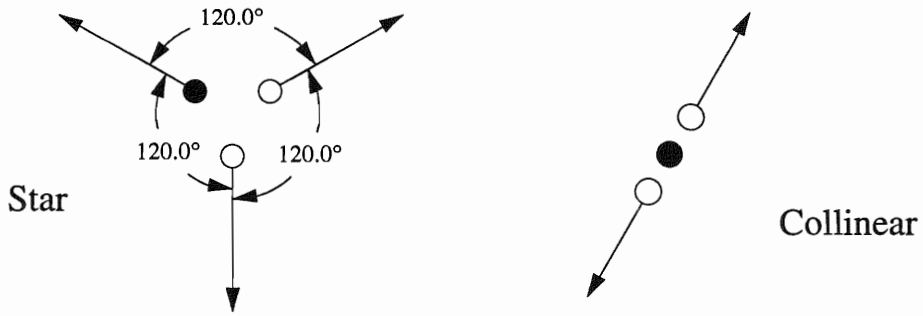

Figure 1.2: Kinematic relationships of the particles in the exit channel of the nd breakup reaction in the center-of-mass system.

Because 3NF effects are expected to be strongly dependent on the geometry of the three interacting particles, it is desirable to measure 3N observables for a variety of these geometries [Fri83]. The nd breakup reaction provides a good tool for searching for scattering observables which show sensitivity to three-nucleon forces, because the kinematics of the reaction permits the geometry of the nucleons in the exit channel to be continuously varied. To exploit this feature of the nd breakup reaction we have measured nd breakup cross sections for two extreme geometries of the particles in the exit channel. The two geometries are the "star" and "collinear" configurations (see Fig. 1.2) and they are expected to exhibit measurable 3NF effects [Mei84b].

In a star configuration the three outgoing particles have momenta equal in magnitude and separated by 120° in the center-of-mass system. Star configurations are further divided into the case where the incident beam direction is perpendicular to the plane of the star (space star) and the case where the beam axis lies in the plane of the star (coplanar star). Because the space-star configuration is insensitive to the details of the NN potential [Wit88b], it is expected to be particularly useful for identifying 3NF effects. By specifying the incident neutron energy and the angles of the two neutrons in the exit channel, a kinematic locus is defined in the $E_{n1} - E_{n2}$ plane (see Fig. 1.3). Observables are then plotted as a function of arc-length (S) along this locus, with S=0 being defined as the point at which E_{n1} is a maximum for $E_{n2} = 0$ and with S increasing in a counter-clockwise manner. Figure 1.4 shows the insensitivity of the space-star cross section to the details of the NN interaction. All four calculations predict the same cross section for the space-star configuration to within 1.2%. In a collinear configuration one of the particles in the exit channel

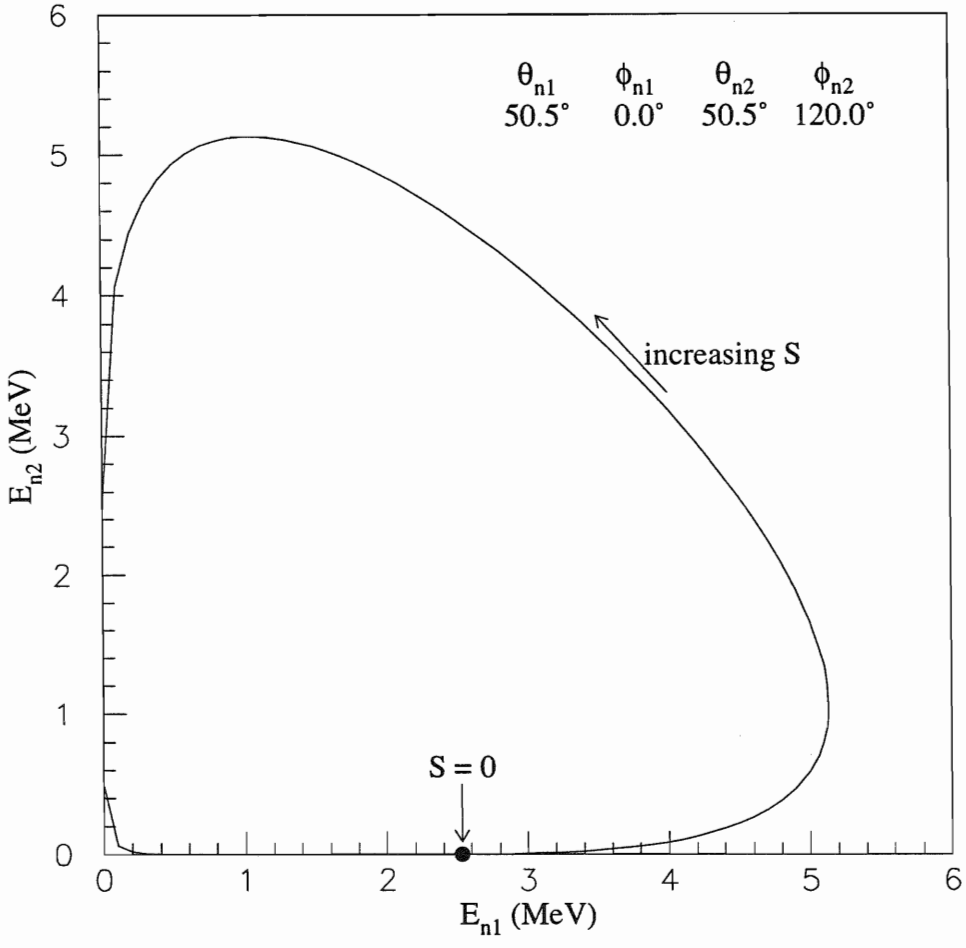

Figure 1.3: Kinematic locus for the space-star configuration. The locus is determined by the incident neutron energy and the two neutron detector angles. Cross sections are presented as a function of the arc-length (S) along the locus.

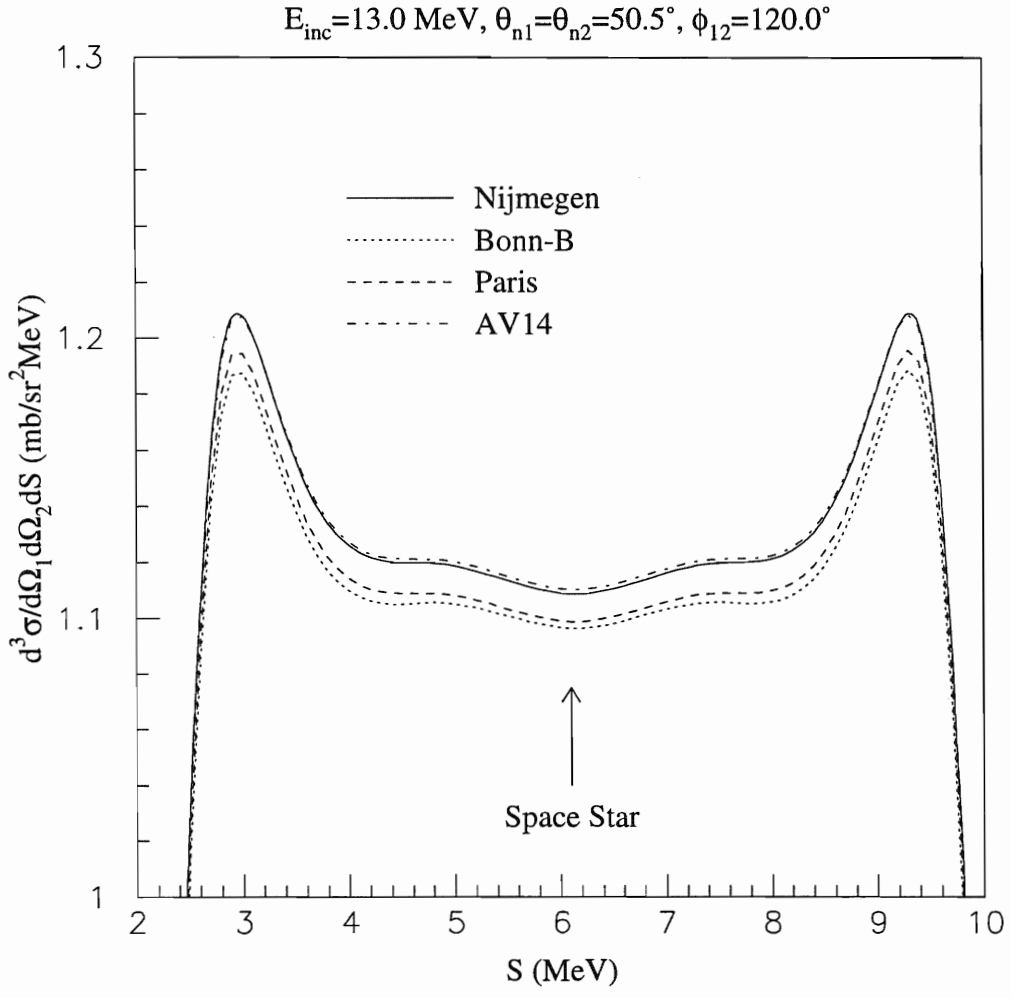

Figure 1.4: Space-star cross-section calculations using four NN potentials. Note the suppressed zero on the vertical axis.

is at rest in the center-of-mass system and the other two particles exit in opposite directions with equal momenta. The influence of three-nucleon forces on observables for this configuration should differ from those in the star configuration.

Recent cross-section measurements of these configurations have produced ambiguous results. At 10.3 MeV two independent measurements [Ste89, Geb93] of the nd breakup cross section for the space star agree fairly well with calculations using only NN forces. At 13 MeV the cross-section data [Str89] for the space-star configuration in nd breakup are ~30% higher than the calculations. Measurement of the pd breakup cross section [Rau91] for the space-star configuration at the same energy produced results which were ~10% lower than the calculation (see Fig. 1.5). Some of the difference for the pd case could be due to the Coulomb interaction [Alt94]. Recent pd breakup cross-section measurements for the space-star configuration at 10.5 and 19.0 MeV [Gro94, Pat94] are also lower than predicted by nd calculations, which use only 2N forces. This trend suggests that Coulomb effects are important for this configuration. The situation is similarly confusing for the collinear configuration. A measurement at 13 MeV [Str89] shows an enhancement at the collinear point which is not predicted by the calculation (see Fig. 1.6).

Because these results are important to understand the size of the effects to be expected from a 3NF, we have measured the nd breakup differential cross section at 13 MeV for the space star, coplanar star and two collinear configurations to a statistical accuracy of about ±5% for 0.5 MeV bins along the kinematic locus. The normalization or scale uncertainty in all our data is ±5%. All measurements were performed at the Triangle Universities Nuclear Laboratory using a shielded neutron source. The 13 MeV neutrons were produced using the ^{2}H(d,n)^{3}He reaction initiated with a dc deuteron beam incident on a 3-cm long cell filled with 7.8 atmospheres absolute of deuterium gas. The scatterer was a 4-cm diameter × 6-cm high cylinder of C_6D_{12} liquid deuterated scintillator (NE-232) in which the recoiling charged particles were detected. The neutrons were detected with an array of eleven liquid scintillators. All three emitted particles were detected to kinematically over-determine the reaction. Simultaneous measurement of nd elastic scattering provided the absolute normalization of the breakup cross section.

The experiment was simulated via the Monte-Carlo method to determine the correction for attenuation of the scattered neutron flux. The absolute neutron detection

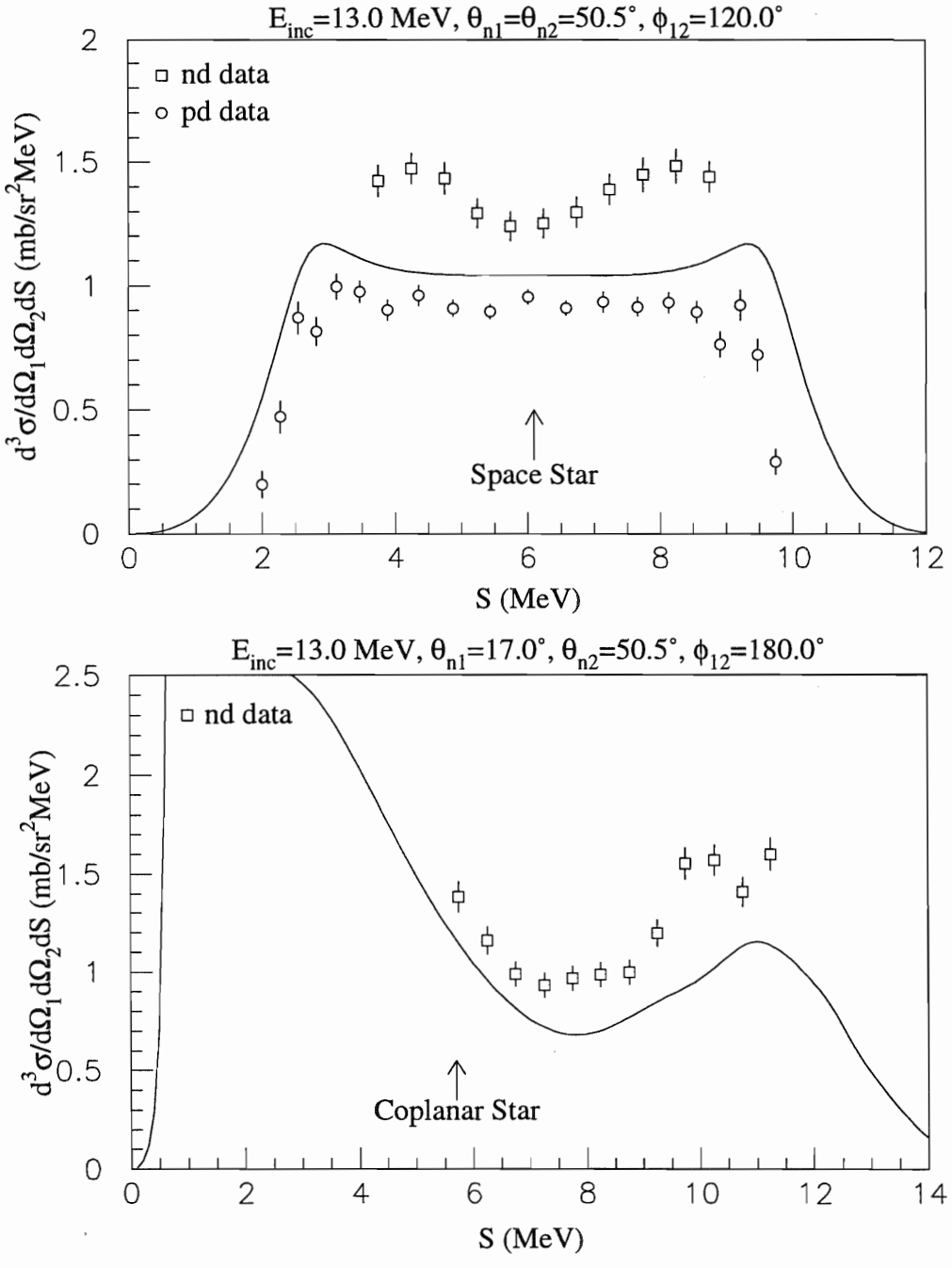

Figure 1.5: Differential cross sections for the space star (top) and coplanar star (bottom) configurations. The solid curve is a point geometry calculation made using the Bonn-B potential. The nd data is from [Str89] and the pd data is from [Rau91].

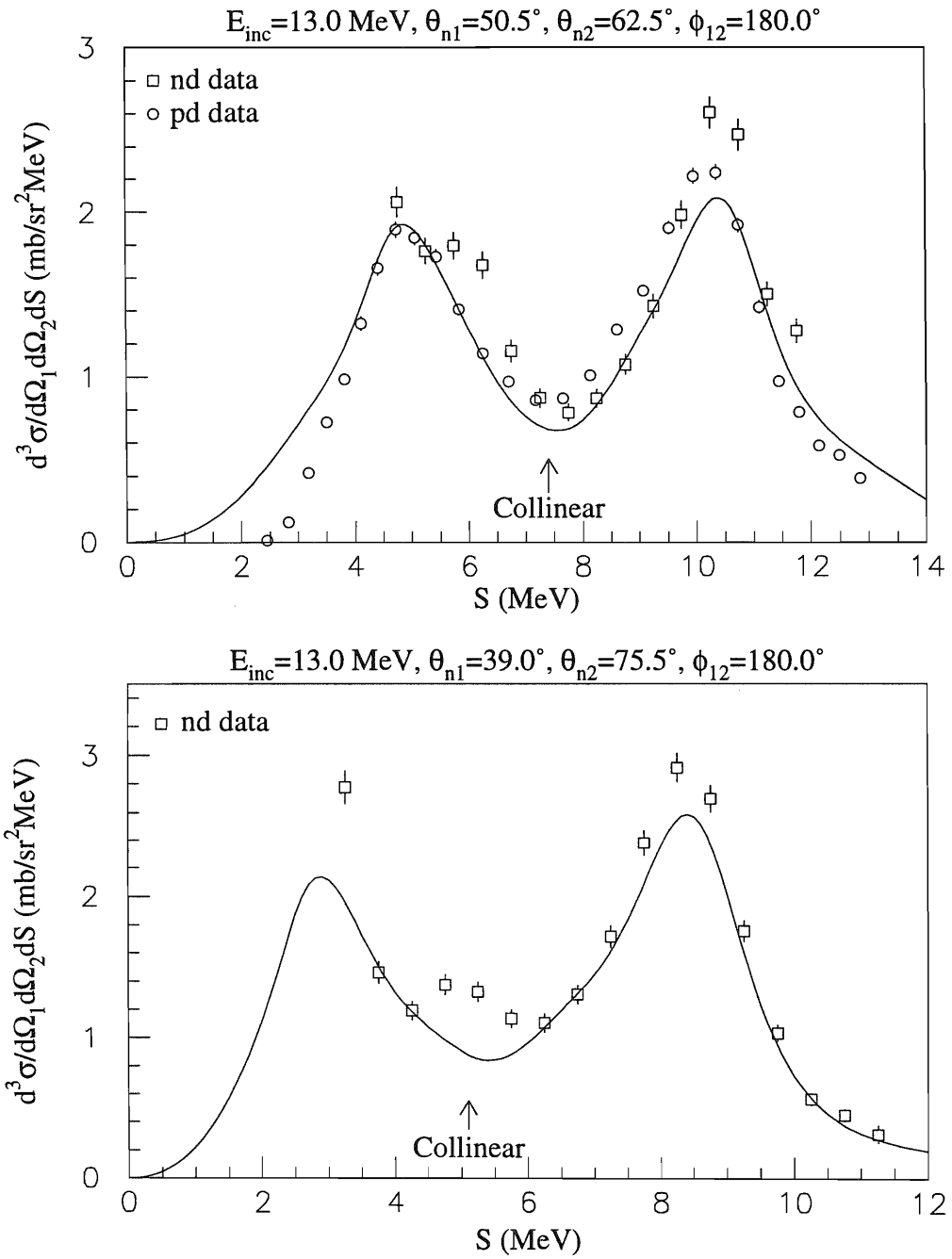

Figure 1.6: Differential cross sections for two collinear configurations. The solid curve is a point geometry calculation made using the Bonn-B potential. The nd data is from [Str89] and the pd data is from [Rau91].

efficiencies for the eleven liquid scintillators were obtained in an independent measurement. No attempt was made to extract a point-geometry cross section from our data by correcting for the finite geometry effects of the experimental setup. Instead the nd breakup calculations using the Bonn-B OBEPQ were performed over the finite geometry of the experiment. The data and calculations were then identically projected onto the point geometry locus for comparison.

Chapter 2

Experimental Details

2.1 Introduction

Differential cross sections for the neutron-induced deuteron breakup reaction at an incident neutron energy of 13 MeV have been measured for four kinematic configurations: the space star (SST), the coplanar star (CST), and two collinear configurations (COLLa, COLLb). All three outgoing particles were detected: the two emitted neutrons in an array of eleven liquid-organic scintillators and the recoil proton in a fully-deuterated, liquid-organic scintillator which served as the deuterium scatterer. The detection of all three particles kinematically over-determines the reaction. Simultaneous measurement of neutron-deuteron (nd) elastic scattering provided the absolute normalization for the breakup cross section. All measurements were performed at Triangle Universities Nuclear Laboratory (TUNL). These data were accumulated over 14 months and represent 2200 hours of actual accelerator time, half of which was spent on development and half on production.

The Direct Extraction Negative Ion Source (DENIS II) was used to produce a 50 keV deuteron beam. This beam was accelerated by the FN tandem Van de Graaff accelerator to 10.4 MeV and directed to a deuterium gas cell on the 20° beam leg with a nominal beam current of 1.5 μA. Since the ion source, accelerator and beam transport systems have been well described in previous papers [Gus82, How84, Hon86], this work will give details only on new developments or those necessary to understand later experimental results.

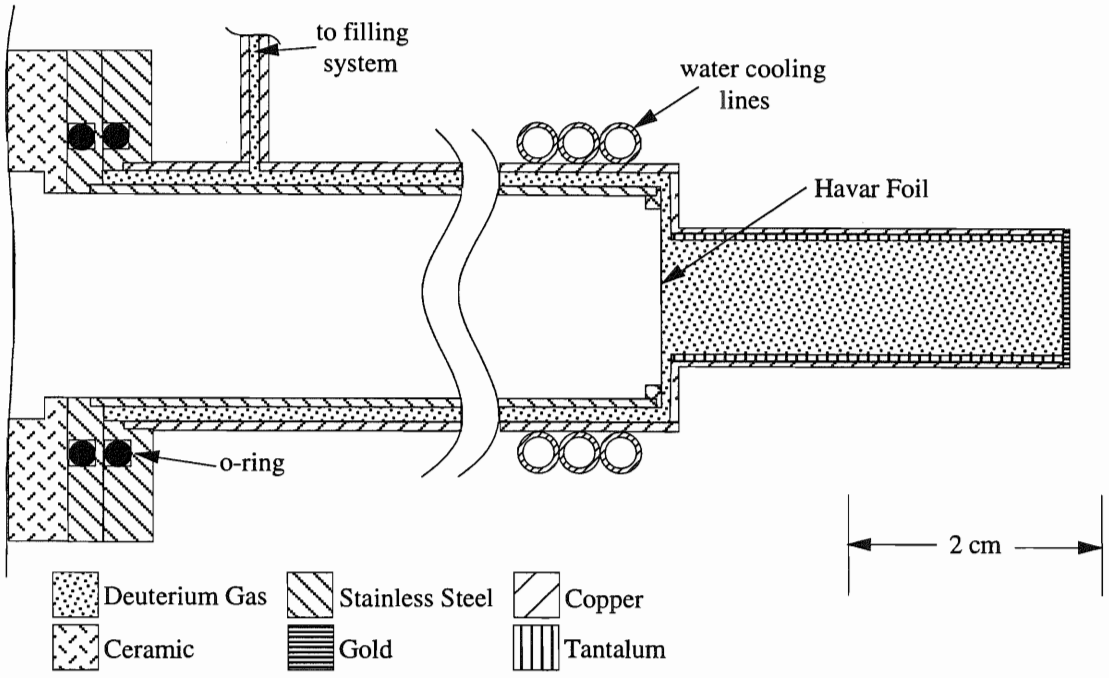

Figure 2.1: Deuterium gas cell used in ^{2}H(n,nnp) cross section measurements.

2.2 Neutron Production and Collimation

2.2.1 Neutron Production

The dc deuteron beam from the accelerator was used to produce a 13.0 MeV neutron beam via the ^{2}H(d,n)^{3}He reaction. This reaction has a high cross section for neutron production in the energy range of interest [Dro78]. The most energetic neutrons produced emerge at a production angle of 0° and are nearly monoenergetic. Both the neutron energy and the cross section decrease rapidly with increasing angle, which makes this reaction well suited for use as a collimated neutron source. Another feature of this reaction that makes it a good source of monoenergetic neutrons is the +3.3 MeV Q-value of the reaction. The positive Q-value causes approximately 5 MeV separation between the monoenergetic neutron group at 0° and the continuum neutrons from the three- and four-body breakup reactions, ^{2}H(d,n)pd and ^{2}H(d,n)ppn, respectively.

The deuterium gas cell used for these measurements is shown in Fig. 2.1. The gas cell was dimensionally the same as that described in [Hon86] with a few modifications

in the materials used and the attachment of the beam stop to the body of the cell. In anticipation of higher deuteron beam currents than used in uncollimated neutron sources at TUNL, the beam stop was soldered to the body of the cell which was made of copper to provide good heat conduction between the beam stop and cooling coils [Wei93]. Distilled water was pumped through the cooling coils and the distilled water was in turn cooled by the laboratory 50° F circulating water system. Air flow was also directed to the gas cell for further cooling. The beam stop was 0.051 cm thick and made of gold to provide good heat conduction while minimizing the background in the neutron beam. The gas cell was isolated from the beam line vacuum by a 1/4 mil Havar entrance foil. The cell was filled to 7.8 atmospheres absolute with deuterium gas. This pressure in the gas cell resulted in a spread in the neutron energy of 400 keV due to energy losses of the deuteron beam through the gas and the Havar foil. The cell was electrically isolated and the charge deposited in the stop by the beam was sent to ground via a beam current integrator. The integrator gave one pulse per fixed amount of charge. These output pulses (BCI) were counted in a scaler.

2.2.2 Neutron Shielding and Collimation

Although the ^{2}H(d,n)^{3}He reaction cross section decreases rapidly with increasing angle, a substantial number of neutrons was still produced at all angles. It was necessary to shield the neutron detectors from the direct flux of neutrons from the production target to reduce the accidental counting rate. For this reason the gas cell on the 20° beam leg was located on one side of a shielding wall and the scatterer was located on the other side. As shown in Fig. 2.2 the shielding wall consisted of a composite of concrete, heavy metals (i.e. steel, iron), lead and paraffin.

A collimator was inserted in the shield wall along the beam axis. Details of the collimator are shown in Fig. 2.3. It was about 115 cm long and consisted of three sections. The two sections closest to the deuterium gas cell were made of copper and the last section was about 32 cm long and made of polyethylene. The collimator was designed to allow the full illumination of the scatterer by the direct forward-angle neutron flux, but to minimize the amount of neutron in-scattering from the sides of the collimator [Gla74]. To achieve this goal the sides of the collimator closest to the gas cell were tapered to an angle so that it could not be directly seen by an observer

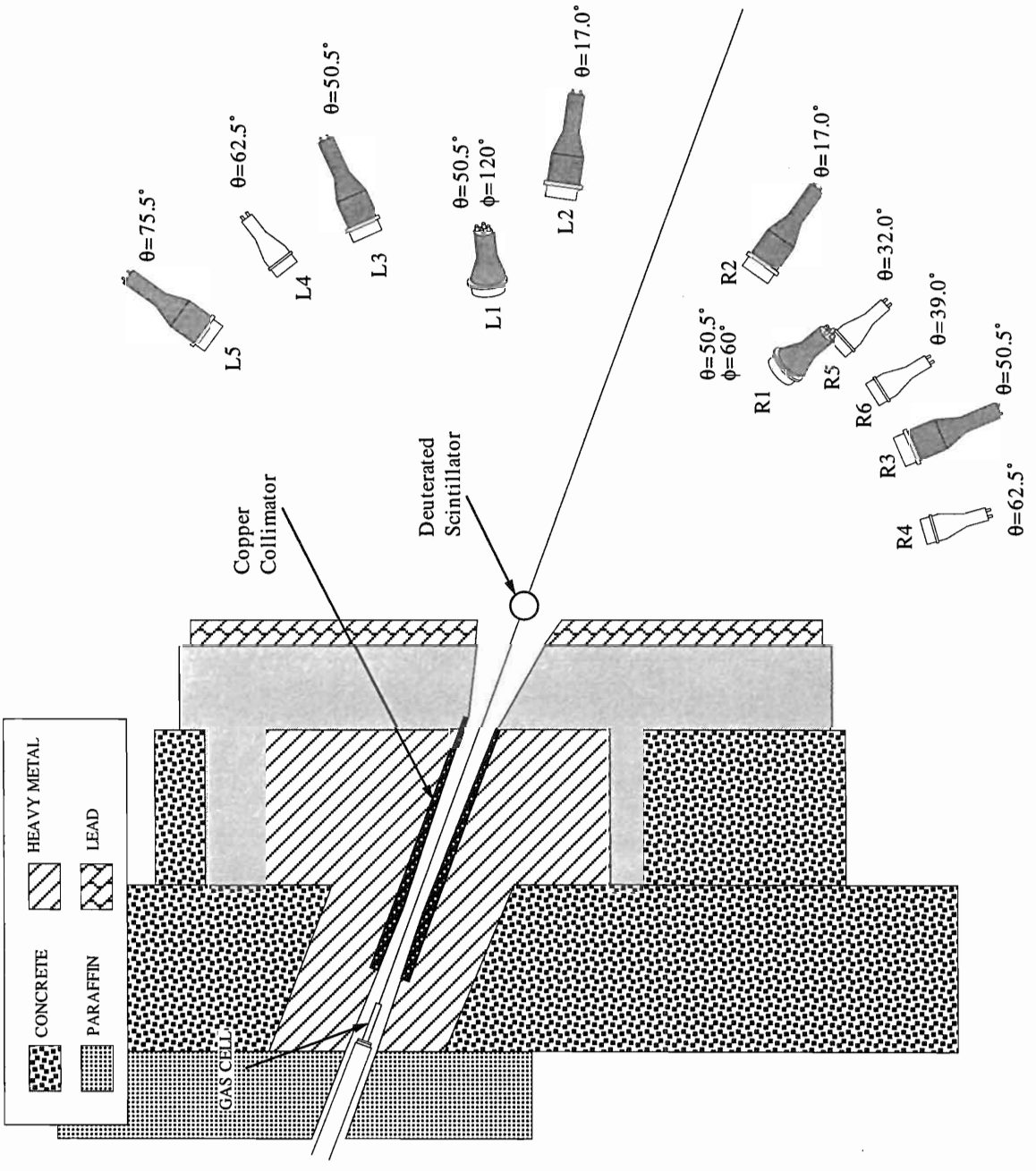

Figure 2.2: Experimental setup for ^{2}H(n,nnp) cross section measurements. Drawing is not to scale.

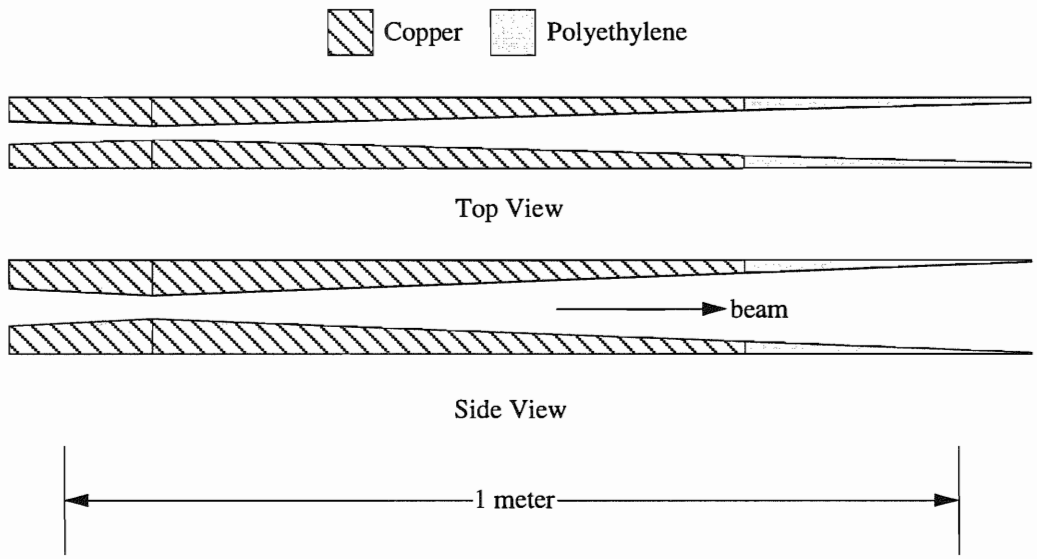

Figure 2.3: Neutron collimator.

at the location of the scatterer. The second half of the collimator was tapered in the opposite direction to hide this portion of the collimator from the direct neutron flux. The net result is that the section of the collimator that is brightly illuminated by the direct neutrons from the source is hidden from the scatterer, and the portion facing the scatterer is hidden from the source. With this design, neutrons that scatter at small angles from the collimator cannot reach the scatterer without passing through some length of shielding material. The throat of the collimator was located 48.2 cm from the center of the gas cell and 123.8 cm from the center of the scatterer.

After installation of the collimator, the beam profile was measured for 13 MeV neutrons at the position of the scatterer using a 0.25 inch wide $\times$ 1 inch high plastic scintillator. As shown in Fig. 2.4 the shield and collimator reduced the neutron intensity outside the central beam by more than three orders of magnitude for 13 MeV neutrons.

2.3 Experimental Setup

The detector setup is shown in Fig. 2.2. The target detector was a thin-walled glass circular cylinder. The detector was 4.19 cm diameter $\times$ 6.39 cm high with a wall

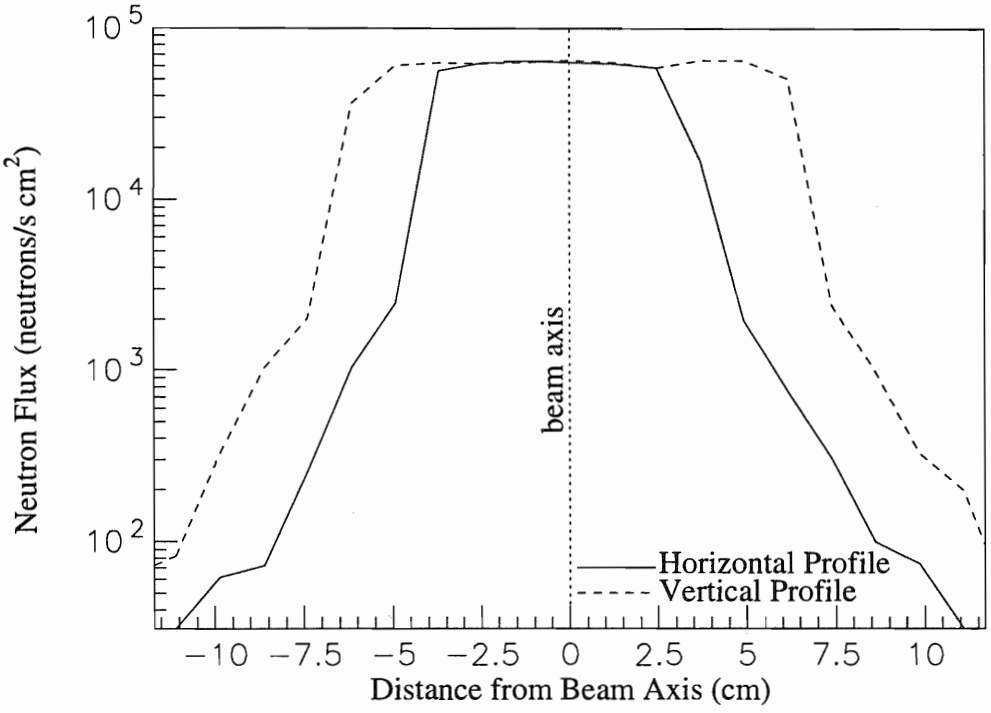

Figure 2.4: Neutron beam profile of collimated neutron source. Measurements were made using 13 MeV neutrons.

thickness of 2 mm. The actual dimensions of the scatterer were measured by the use of a digital X-ray machine located at the Duke University Medical Center. The center of the scatterer was positioned to coincide with the center of the neutron beam profile and approximately 10 cm from the shielding wall. This detector fulfilled the dual purpose of serving as a deuteron scatterer and as a detector for recoil charged particles. The detector was directly mounted on a two inch photomultiplier tube (PMT). Throughout the rest of this work this detector will be referred to as the center detector since it was located at the center of the arc formed by the neutron detectors.

Two types of neutron detectors were used for this experiment. Details about

detector	θ	ϕ	flightpath (cm)	diameter (cm)	fluid type
R1	50.5°	60°	149.8	12.7	BC 501
R2	17.0°	0°	152.2	12.7	BC 501
R3	50.5°	0°	151.8	12.7	BC 501
R4	62.5°	0°	153.2	11.4	NE 213
R5	32.0°	0°	154.0	11.4	NE 213
R6	39.0°	0°	151.6	11.4	NE 213
L1	50.5°	120°	149.9	12.7	BC 501
L2	17.0°	180°	152.9	12.7	BC 501
L3	50.5°	180°	154.2	12.7	BC 501
L4	62.5°	180°	176.9	11.4	NE 213
L5	75.5°	180°	162.9	12.7	BC 501

Table 2.1: Neutron detector setup. Detectors 1-4 were mirrored about the beam axis. Because of the beam angle relative to the wall, 75.5° could only be achieved on the left side. The 39.0° detector was chosen to complement the 75.5° detector kinematically. The 32.0° detector was used for development of future experiments and for nd elastic scattering.

the detectors are given in Table 2.1 along with geometry information describing the experimental setup. For convenience, some of the information shown in Fig. 2.2 are repeated in Table 2.1. The angles theta and phi are the usual polar and azimuthal scattering angles, respectively. The angle θ is measured relative to the incident beam direction and the angle ϕ is measured up from the horizontal plane with $\phi = 0°$ to the right of the beam axis and $\phi = 180°$ to the left of the beam axis. All angles are measured to the center of the detectors. Seven of the detectors were 12.7 cm diameter $\times$ 5.08 cm thick and mounted directly on 12.7 cm diameter PMT. These detectors were filled with BC-501 scintillator fluid. The remaining four detectors were 11.43 cm diameter $\times$ 5.08 cm thick coupled to a 5.08 cm diameter PMT by a 5.08 cm high truncated-cone light guide. These detectors were filled with NE-213 scintillator fluid. The two types of scintillator fluid are similar. There is a slight difference in the hydrogen-to-carbon (H-C) ratio between the two types which results in a difference in the detector efficiencies between the two types (see App. A). Both types of fluid exhibit a difference in anode signal decay times between events from γ-rays and neutrons which makes pulse shape discrimination possible (see Sec. 3.1.2).

Because these detectors are filled with a liquid, some compensation must be al-

Configuration	θ_{n1}	θ_{n2}	ϕ_{12}	Detectors
SST	50.5°	50.5°	120.0°	R1 - L3
				R3 - L1
CST	17.0°	50.5°	180.0°	R2 - L3
				R3 - L2
COLLa	50.5°	62.5°	180.0°	R3 - L4
				R4 - L3
COLLb	39.0°	75.5°	180.0°	R6 - L5

Table 2.2: Detectors associated with each configuration. Descriptions of the configurations are given in Chap. 1.

lowed for expansion and contraction due to temperature changes. The seven 12.7 cm diameter detectors and the center detector were built with an expansion region which could not be seen by the PMT. With this design the active volume of the detector remains constant. However, temperature changes can affect the neutron detector efficiencies and the total number of target nuclei in the center detector due to density changes. Throughout the data acquisition, the temperature in the target area was continuously monitored by four thermistors. The signals from these thermistors were sent to the computer and stored for each run. The temperature in the target area was stable to within half a degree Fahrenheit throughout the experiment. The stability of the temperature in the target area made it possible to neglect any effects due to density changes in the detectors with an expansion volume.

The four 11.43 cm detectors had no expansion chamber for the fluid, so a small bubble of nitrogen gas was left in the scintillator volume. The bubble occupied about 2.5% of the total cell volume. The detection efficiency of these detectors is unaffected by temperature changes because there is no change in the amount of fluid viewed by the PMT. The solid angle of these detectors is, however, slightly smaller than if the entire volume were filled with fluid. The combined effects of the lower H-C ratio and the presence of the nitrogen bubble in the cell caused the detectors filled with NE-213 fluid to be about 5% less efficient than those filled with BC-501 fluid. The stability of the temperature in the target area made it possible to neglect any effects on the solid angle of these detectors.

Table 2.2 shows the detectors associated with the kinematic configurations of interest. Three of the four configurations were duplicated on each side of the beam axis

to decrease the amount of accelerator time necessary to reach the desired statistical accuracy. Due to the angle of the beam through the shielding wall it was not possible to place a detector at 75.5° on the right side of the beam axis.

2.3.1 LED Pulsers

In order to check the gain stability of the neutron detectors and to measure the complete dead-time of the system (both computer and electronics), LED pulser signals were fed into the PMT's of six detectors via fiber optic cable. The gain of the LED was stabilized by a PIN photodiode [Rei80b, Rei80a]. Due to limitations on the number and length of the fiber optic cables, it was necessary to use two LED driver systems. Both systems were triggered by a common oscillator (see Fig. 2.5) to stagger the arrival of the two light signals at the center detector . This was accomplished by strobing one pulser module with the delayed output ($\sim$500 μs) of the other pulser module. The sync outputs of each pulser module were used to provide routing information for the data analysis software. The gains of the two pulsers were adjusted so that a gate in the upper quarter of the center detector pulse height spectrum could be used to distinguish between the two pulsers.

While the system was operational throughout the data acquisition phase of this experiment, it was used only infrequently. It was found more efficient and convenient to check gain stabilities using a ^{137}Cs source rather than to introduce an additional 3% computer dead-time due to pulser events.

2.4 Detection Electronics and Data Acquisition

Data acquisition at TUNL was controlled by a DEC VAXStation 3200. The VAXStation was interfaced to two daisy-chained CAMAC crates via a MBD-11 Microprogrammed Branch Driver (MBD) [Rob81]. All software routines made use of the TUNL XSYS data acquisition and analysis package [Gou81]. All the data were stored in an event-by-event mode directly to magnetic tape to allow off-line sorting to be performed (see Sec. 3.1). The neutron time-of-flight (TOF) and pulse shape (TPSD) were digitized by a Phillips Model 7186 16-channel, 12-bit Time-to-Digital Converter (TDC). The detector pulse height signals were sent to two EG&G ORTEC Model AD413A

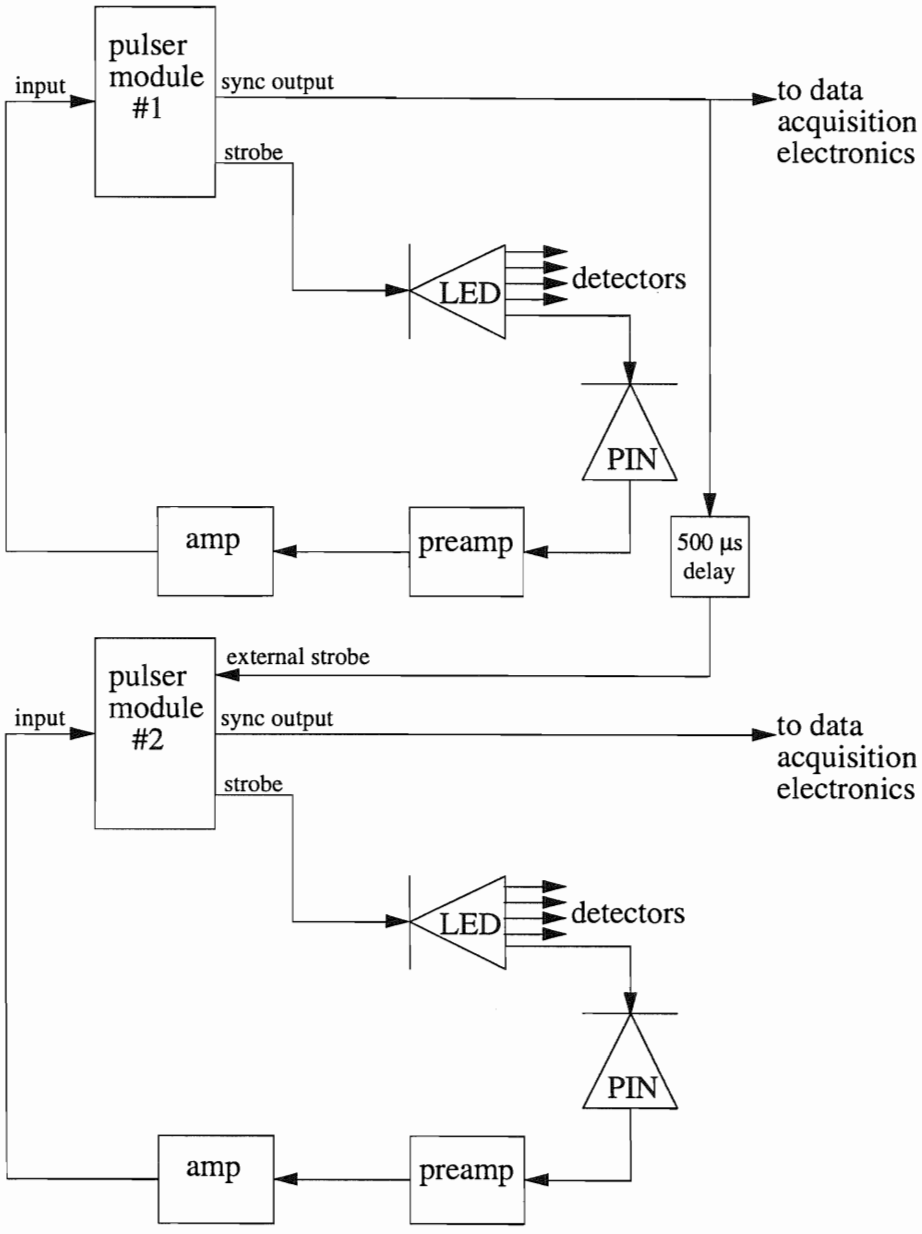

Figure 2.5: LED pulser setup.

Pair Number	Detector	Pulser
1	R1	
	R5	√
2	R2	√
	R3	
3	R4	√
	R6	
4	L1	√
	L5	
5	L3	√
	L4	
6	L2	√

Table 2.3: Neutron detector pairs. The √ in the pulser column indicates the detector in the pair equipped with a fiberoptics cable to receive the LED signals.

4-channel, 13-bit Analog-to-Digital Converters (ADC). Routing for each event was controlled by a Bi Ra Model 2351 12-bit input register (hit register). Twenty-two words of data were stored per event:

- 6 neutron detector pulse heights
- 2 center detector pulse heights
- 6 neutron time-of-flight signals
- 6 neutron detector pulse shape signals
- routing from hit register
- routing from TDC hit register

2.4.1 Neutron Detectors

To economize, the signals from two neutron detectors were summed into one set of electronics for the *pair* of detectors. With eleven detectors there were five pairs plus one lone detector (see Table 2.3). The single detector will be referred to as a "pair" to provide consistency in the discussion. The choice of which detectors to place in

each pair was made so as to minimize the number of kinematic configurations which were lost. One detector in each pair was provided with an LED pulser signal.

Fig. 2.6 shows the electronics setup for a pair of neutron detectors. The dynode signals were summed in an integrating preamp. The paired dynode signal was then amplified and sent to the ADC. The detector anode signals were sent two places. First, they were summed in a LeCroy 428F linear fan-in and sent to the Canberra 2160 PSD module. It was found that the quality of the pulse shape spectrum was better when taken using a LeCroy 428F linear fan rather than a Phillips 740 linear fan. The output of the PSD module was then sent to the TDC to generate the pulse shape spectrum (see Sec. 3.1.2). Second, the anode signal of each detector was sent to an individual constant fraction discriminator (CFD). One output from each CFD was sent to the hit register to tag which detector fired. Having a separate CFD for each detector made it possible to individually set the lower threshold level for each detector. The hardware thresholds were set to less than one eighth of the Compton recoil edge produced by the γ-rays from a ^{137}Cs source ($< \frac{1}{8}$ x Cs). This bias level corresponds to neutron energies of < 250 keV.

For each detector pair the output of the two CFDs were then OR'ed together. This signal was used in four places:

1. provided the stop signals to TDC for TOF measurements of each pair,
2. used to strobe the PSD module,
3. used to form the coincidence between each neutron detector pair and the center detector,
4. used to form the logical OR of all the neutron detectors (see Sec. 2.4.3 and Fig. 2.6).

The alignment of the input signals to the logic module used to form the coincidence between the neutron detectors and the center detector is shown in the top half of Fig. 2.7. The alignment of the routing signals from the neutron detectors with the strobe to the hit register is shown in the lower half of Fig. 2.7. It should be noted that the hit register functionally duplicated the coincidence between the neutron and center detectors. Therefore, care was taken to ensure that the earlier coincidence which produced the P#C signals was the more restrictive of the two coincidences.

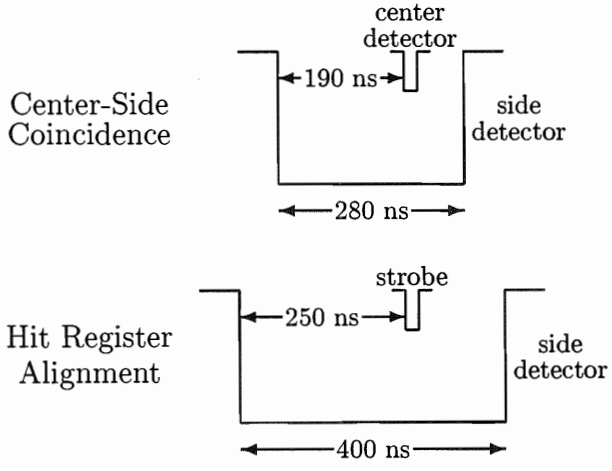

Figure 2.7: Top: Signal alignment for neutron detector-center detector coincidence. Bottom: Signal alignment at input to hit register. Alignment shown for signals generated by the LED pulser.

The coincidence timing in both cases was set using the LED pulsers (see Sec. 2.3.1) and the signals shown in Fig. 2.7 are for pulser timing. The pulsers produced the same timing, within about 5 ns, as a γ-ray event in the TOF spectra. The 190 ns to the left of the center detector signal was set to ensure that enough time was allowed for the lowest energy neutrons to reach the neutron detector. The time to the right was used to give information on accidental coincidences (see Sec. 3.1.1).

2.4.2 Center Detector

The electronics for the center detector are shown in Fig. 2.8. The detection of both recoil protons and deuterons over the range of reaction and scattering angles of interest in these measurements required a large dynamic range for the center detector pulse height. This was accomplished by using two dynode circuits (only one is shown) with different gains. The high gain circuit was taken from the tenth dynode in the PMT dynode chain. The low gain circuit was taken from the ninth dynode.

Due to the high rate in the center detector ($\sim$500 kHz) and the long integration time ($\sim$10 μs) of spectroscopy amplifiers, it was necessary to gate the linear signals prior to amplification. The gate signal (T1) was generated by the coincidence between

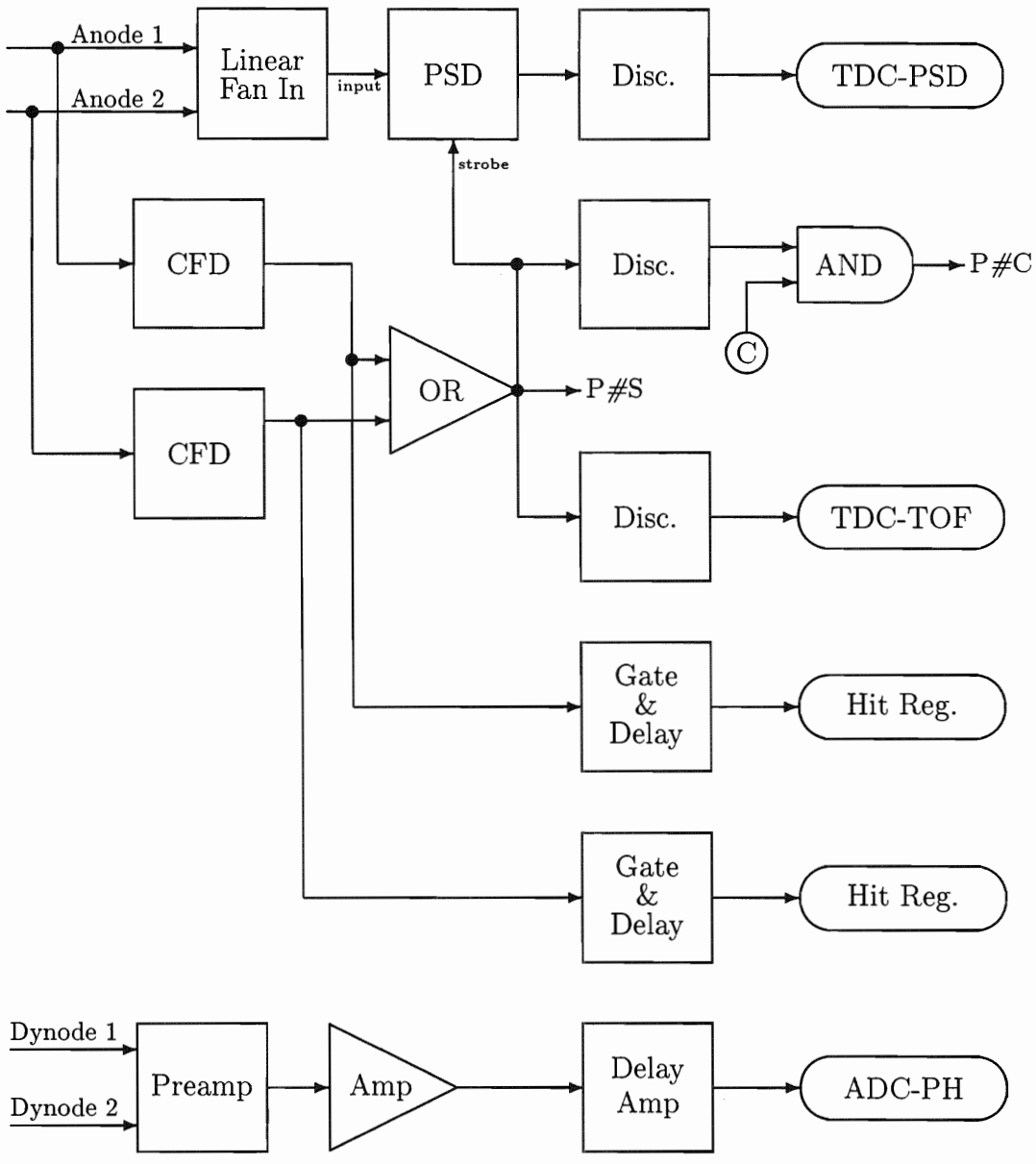

Figure 2.6: Detection electronics for a pair of neutron detectors

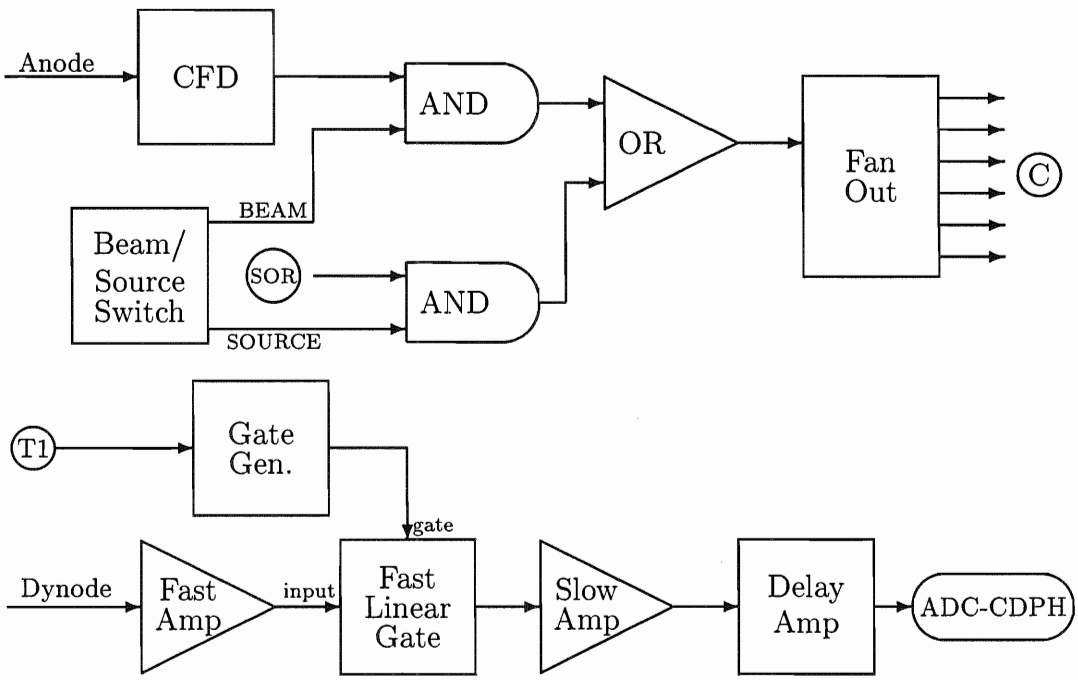

Figure 2.8: Electronics for the center detector.

the neutron detectors and the center detector (see Fig. 2.9). Linear signals passing the gate requirement were amplified and sent to the ADC. One amplified center detector dynode signal was sent to each of the two ADCs. This arrangement forced a non-zero value to be digitized by both ADCs ensuring that *both* ADCs generated a LAM for every event.

The anode was sent to a CFD where a bias of $\sim\frac{1}{20}$ x Cs was set. This extremely low bias was necessary due to the low proton recoil energy of the CST configuration. During data acquisition, the CFD output was AND'ed with a dc level (see Sec. 2.4.3) and then fanned out to the neutron detector coincidences.

2.4.3 Beam/Source Switch

During the course of the experiment, the gain settings and lower level thresholds of the CFDs used for the neutron detectors were checked daily using a ^{137}Cs source. In order to store these spectra in the computer without changing the electronics, it was necessary to produce a false coincidence between the neutron detectors and the

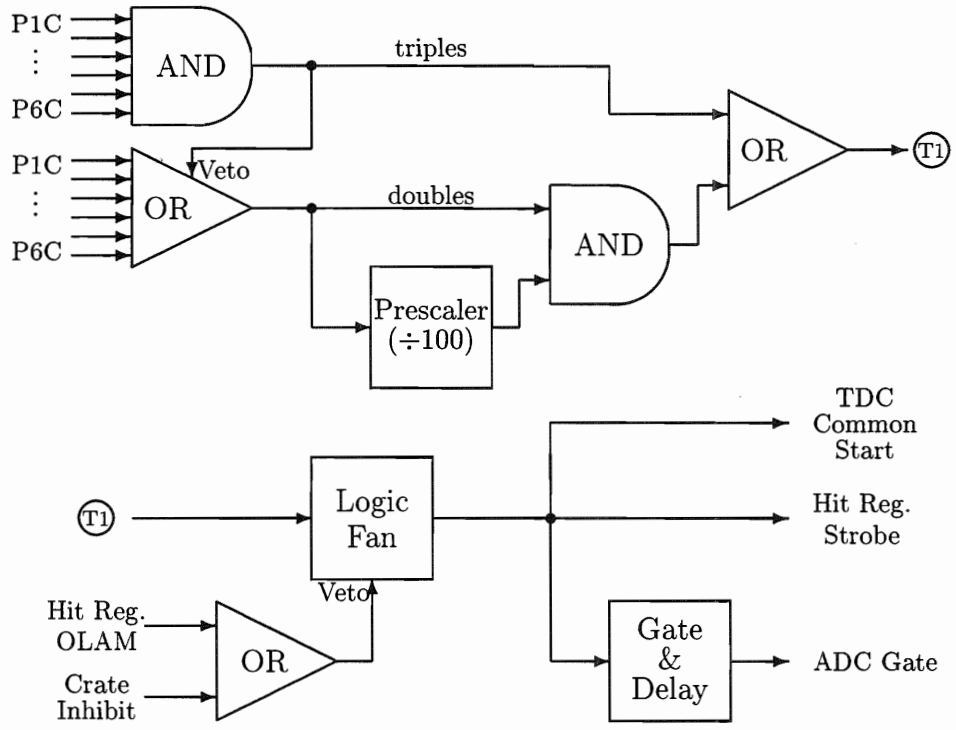

Figure 2.9: Computer trigger circuit.

center detector. For this reason the beam/source switch was installed. This module served the simple function of switching a dc level between two outputs, either the beam position or the source position.

In the beam position, the -6V dc level was ANDed with the output of the center detector CFD . The output of the AND circuit was fanned to form center-side coincidences. When using the Cs source for gain checks there was no real coincidence between the neutron detectors and the center detector. In the source position the -6V dc level was ANDed with the OR of all the neutron detectors, i.e. the OR of all the P#S signals thereby putting each neutron detector in coincidence with itself to generate the trigger signal to the computer.

2.4.4 Computer Trigger

The computer trigger circuit made use of modules that employ majority logic. These modules have multiple inputs and a switch that determines the number of inputs at

a logic "true" level needed to produce an output. For example, the OR at the top left of Fig. 2.9 represents a module with six inputs which requires only one to be "true" to produce an output. The AND just above that represents a module with six inputs which requires two overlapping "true" inputs to generate an output. This diagram has been simplified for clarity because the actual modules used have only four inputs. The actual circuit consisted of ANDs and ORs as required to produce what is represented in the figure.

The signals P#C were the coincidences between one neutron detector pair and the center detector. The output of the AND implies that more than one neutron detector pair met this requirement. The signals from this branch of the circuit will be referred to as the "triples", since three detectors were in coincidence (i.e. the center detector and at least two neutron detectors). The output of the OR was vetoed by the triple-coincidence signal so that only double coincidences ("doubles") could occur in this branch. The doubles were scaled by a factor of 100 to reduce the rate of triggers to the computer. The scaled doubles signal was then ORed with the triples to produce the signal "T1".

The T1 signal was used to gate the center detector linear signals before amplification and was sent to the interface to form the computer trigger. At the interface T1 was vetoed by two signals:

1. the Crate Inhibit signal.

2. the OLAM generated by the hit register.

The Crate Inhibit was raised whenever data acquisition was turned off. The hit register OLAM was raised whenever the hit register recorded an event and remained raised until the event was processed by the MBD. The software package read all other CAMAC modules before reading the hit register to ensure that all the data from one event was processed before the next event could trigger the digitizers.

The output of the logic fan supplied the trigger to the four modules in the CAMAC crate: the hit register strobe, the TDC common start, and the master gate on each of the two ADC's.

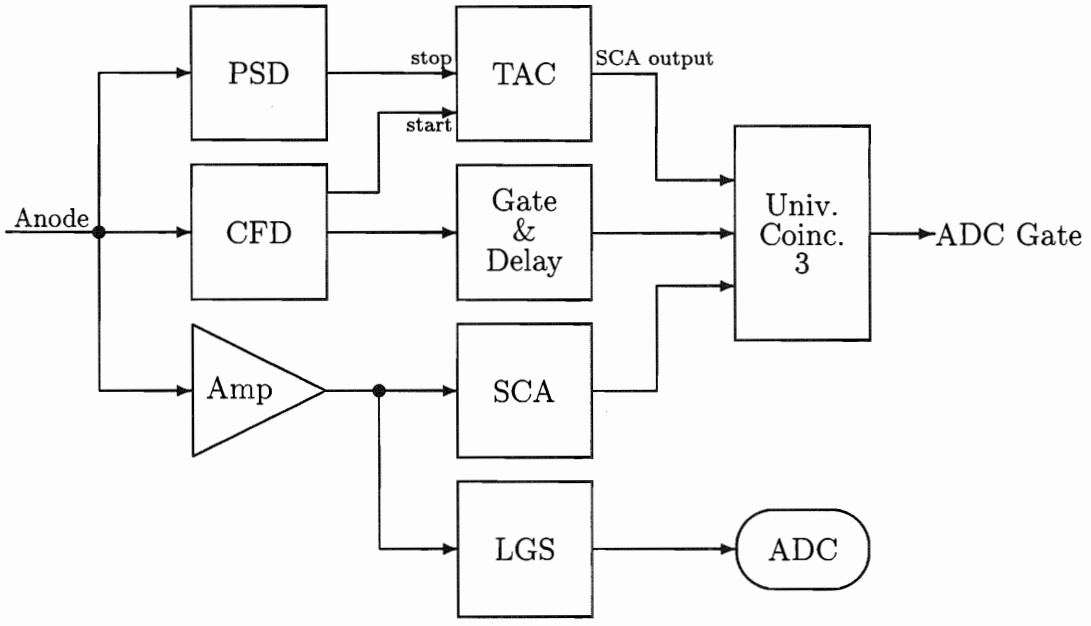

Figure 2.10: Zero degree monitor electronics.

2.4.5 Monitor Detector

Although beam current integration techniques were employed, a neutron detector was positioned at 0° to monitor the direct neutron flux. The monitor detector was a 45 mm × 158 mm × 76 mm rectangular NE-213 scintillator coupled via a light guide to a 5.08 cm diameter PMT. The detector was mounted at the same height as the scatterer and approximately 4 m downstream from it.

The electronics for the monitor are shown in Fig. 2.10. The pulse height signal was amplified, stretched and sent to an ADC. Since the detector was exposed to the full 0° neutron flux, very restrictive requirements were imposed on the ADC gate signal. The lower-level threshold was set on the CFD to reject signals caused by neutrons with energies less than 8 MeV. The SCA output of the PSD-TAC was set to eliminate γ-rays. Since the CFD lower level threshold does not produce a sharp cut on the pulse height, the amplifier output was sent to an SCA to set the neutron bias level. All three of these signals- the PSD-TAC SCA output, the CFD output, and the amplifier SCA output were required to gate the computer. The yields within a gate set in the pulse height spectrum were used to monitor the neutron flux during data acquisition.

Chapter 3

Data Sorting, Reduction and Analysis

3.1 Introduction

During the on-line data acquisition the events were tested and sorted into one-dimensional (1D) and two-dimensional (2D) histograms. To minimize the computer "dead-time," i.e. the time in which the computer was unable to handle an incoming event because it was still processing a previous one, on-line testing and sorting was kept to the minimum necessary to allow the experimenters to be confident of the quality of the incoming data. For this reason, the data were stored event-by-event on magnetic tape for a more complete analysis off-line. The event mode storage maintained the relation between the various parameters in each event. In the off-line analysis cuts and tests were put on the parameters to reject background events which otherwise would have to be subtracted from the final spectra. This background rejection is important to reduce the final statistical uncertainty of the results.

A variety of software packages were developed for the analysis of these data. The sorting software packages consisted of a sorting algorithm written in Event Analysis Language (EVAL) [Gou81] along with several FORTRAN subroutines which were called by the EVAL code. The first step in every EVAL code was a call to a subroutine to test the value of the hit register. This was used to determine whether the event was generated by the pulser, a double or a triple coincidence. In the case

of double coincidences it determined the neutron detector involved and in the case of triple coincidences it determined the kinematic configuration. Examples of other subroutines include:

- generation of the PSD spectra
- calculation of the difference in TOF between the two neutrons for triple coincidences
- calculation of all three particle energies for triple coincidences
- projection of the triples data onto the kinematic locus

The first step in the off-line analysis was the data sorting. This consisted of replaying the data event-by-event and applying cuts. Because the full event was stored, the relation between parameters could be tested in various ways. Successive cuts were applied to the data and the spectra generated thereby became more and more restricted.

In the first pass through the breakup data a call to a subroutine wrote selected parameters to a new event file for later analysis. The original version of XSYS did not allow event-mode storage during off-line analysis, so some changes to XSYS were necessary. In XSYS the EVAL code is installed as a subprocess by the code XTPSORT. This code was modified to open and close files in the proper format for event-mode storage. The events were written to the files by a subroutine called from the EVAL code. The user process communicates with the subprocess by means of XTPEVOP. This code was modified to allow the user to instruct the subprocess to open and close event files.

This chapter will describe the methods used in sorting the double- and triple-coincidence data and the handling of the accidentals. Extraction of the yields from the spectra is described as well as the corrections to the yields which were calculated in the Monte-Carlo simulation of the experiment. From the corrected yields, the breakup differential cross section was calculated.

3.1.1 Accidental Coincidences

In a coincidence experiment there is always the possibility of "accidental" coincidences [Leo92]. For example, if two completely random oscillators of rates R_1 and R_2 are

placed in a coincidence of time width τ, then the rate of accidental coincidences, A, will be $A = \tau R_1 R_2$. For this experiment, accidental coincidences occur between the center detector and each of the neutron detectors. The actual random rates (sample uncorrelated) were on the order of a few hertz, which was comparable to the rates due to the scattering processes under investigation.

These accidental coincidences are truly random in time and produce a flat accidental background in the neutron TOF spectra. To determine the contribution due to these random events in the region of the TOF spectrum corresponding to elastic scattering and the breakup reaction a gate was set in a region of the TOF spectrum where no true events can occur, specifically before the peak due to the γ-rays. The events which fell in the accidental gate were treated in the same manner as the events in the gate of interest (i.e. the kinematic regions for the nd elastic scattering and the breakup reaction). Eventually these accidentals events must be subtracted to obtain only the true events. This method is sufficient for the double coincidences, however, it is more complicated for the triple coincidences. In this case either one or both of the neutron coincidences could be due to random coincidences. Therefore, it was necessary to consider all possible combinations (see Sec. 3.3.2).

3.1.2 Pulse Shape Discrimination

Pulse shape discrimination (PSD) with liquid-organic scintillators is made possible by the difference in the decay time of the anode signal produced by γ-rays and neutrons [Can83]. The PSD module, which is manufactured by Canberra Industries, produces an output timing signal which depends on the decay time of the input signal. To generate a PSD spectrum the timing signal from the PSD module is compared in a time-to-digital converter (TDC) to the timing signal from the constant fraction discriminator (CFD), which triggers on the leading edge of the anode signal.

The neutron TOF was measured in a TDC operated in common start mode with the start signal provided by the timing of the center detector CFD and the stop signals from the neutron detector CFDs. The TDC was used to measure the pulse shape spectrum of each neutron detector by stopping the TDC with the output of the PSD module. Because the TDC was started by the center detector CFD output, the raw PSD spectrum for a neutron detector was the sum of the neutron TOF and

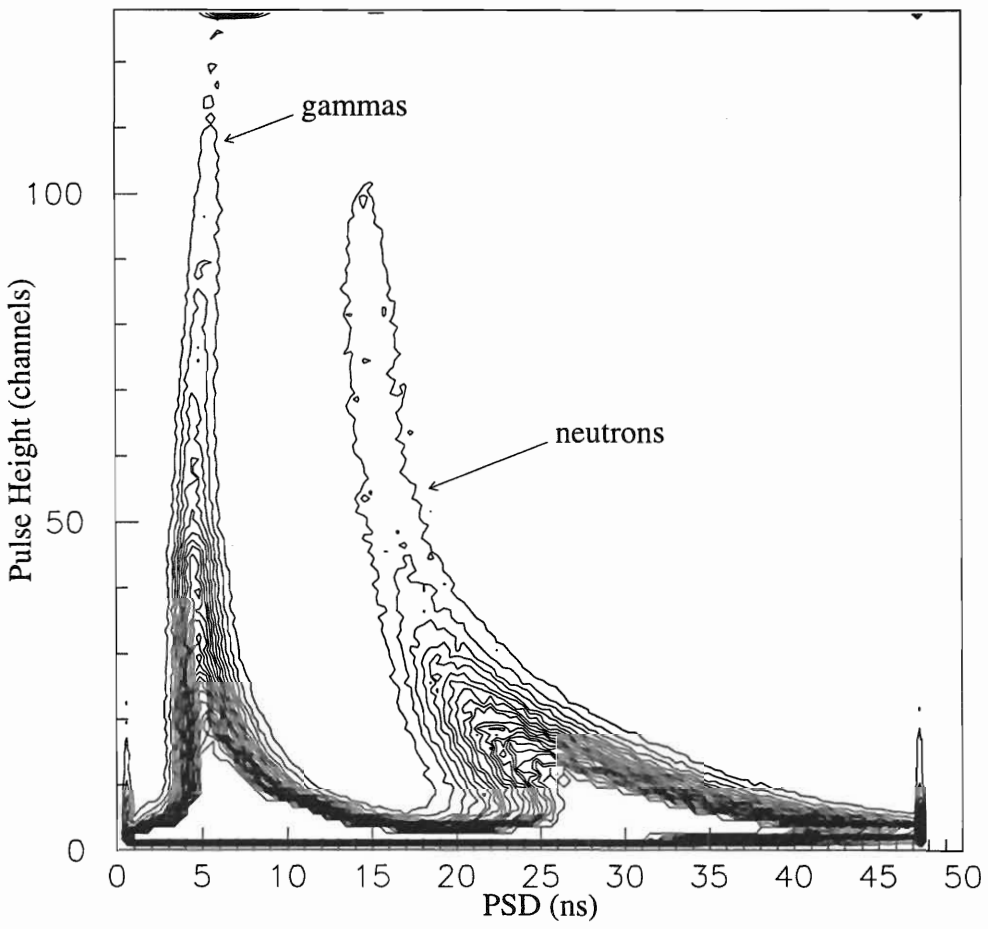

Figure 3.1: PSD *vs.* Pulse Height for a neutron detector. The choice of zero nanoseconds for the PSD is arbitrary.

the pulse shape (PS) and will be referred to as the TPSD spectrum. A 400 ns TDC range was chosen to allow 300 ns for the neutron TOF and 100 ns for the PS.

During the sorting process the PSD spectra were generated by a user-written FORTRAN subroutine which was called from the EVAL code. The TPSD and TOF values from the TDC were passed to the subroutine retaining the full 12-bit resolution of the TDC. The subroutine subtracted the TOF from the TPSD to generate the actual PSD spectrum. The PSD value was then divided by 4 and forced to fit in the channel range from 1 to 120. This compressed spectrum was plotted versus the neutron detector pulse height (see Fig. 3.1) and a 2D gate was used to discriminate against γ-rays.

A software-generated time shift was used to display a 50 ns slice of the PSD spectrum. The full 12-bit resolution of the TDC was used, therefore digitized values ranged from 1 to 4096. When that range is divided by 4 it produces a value between 1 and 1024. This corresponds to the full 400 ns TDC range. However, the PSD spectrum should be $\sim$70 ns. By plotting this value in a 128-channel spectrum only 50 ns are displayed. Therefore, a software time shift was added to display the proper region of the spectrum without further loss of time resolution. The digitized values above channel 120 were set to 120 to ensure that neutrons were not lost in the process.

3.1.3 Finite Geometry Considerations

In an ideal scattering experiment the beam would scatter from a point target and into a point detector. In reality, the target and the detector subtend some finite solid angle. For neutron scattering experiments these effects can be quite important due to the relatively large sizes of the target and the detectors. These effects are divided into three main categories: finite geometry effects, neutron flux attenuation and multiple scattering effects within the target. In order to correct the data for these effects, the entire experiment was simulated by the Monte-Carlo method.

The neutron flux attenuation arises primarily from the large size of the target. However, the attenuation is also caused by the structural materials of the target and the neutron detector and by the air through which the scattered neutron flux passes. Multiple scattering effects are caused by the large volume of the target. In this case a neutron is scattered several times within the target volume. This multiple-scattered

neutron is then detected in one of the neutron detectors. The finite geometry effects arise from uncertainties in the actual scattering angles due to the large size of the target and the detectors.

In the case of the breakup events, the angular uncertainty produces some uncertainty in the kinematic locus associated with each event. For the SST the angular uncertainties were $\pm$ 4.0° in the polar scattering angle (θ) and $\pm$7.2° in the azimuthal scattering angle (ϕ). With three particles in the exit channel, defining the scattering angles of two of the particles determines a kinematic locus of allowed energies for all three particles. The finite geometry introduces some angular uncertainty, which in turn spreads the data about the kinematic locus defined by the point geometry. A portion of the locus for the SST configuration is shown in Fig. 3.2 along with other loci within the angular resolution of the experiment. There is also some uncertainty in the incident neutron energy due to the size of the gas cell. This uncertainty in the incident neutron energy produces a similar effect.

For any single event in this experiment it was possible to determine all three particle energies but it was impossible to determine the "real" kinematic locus with which the event should be correlated. Instead the data were projected onto the "ideal" locus which is determined by the point geometry as defined by the center of the neutron production target, and the center of each detector (see Sec. 3.3.4). The yields were binned in 500-keV steps of arc-length (S) along the locus. These yields were then related to the cross section by:

$$\begin{aligned} Y_{bu} &= \frac{d^3\sigma}{d\Omega_1 d\Omega_2 dS} \cdot d\Omega_1 \cdot d\Omega_2 \cdot dS \cdot \alpha_1\,(E_{n1}) \cdot \alpha_2\,(E_{n2}) \\ &\quad \cdot \epsilon_1\,(E_{n1}) \cdot \epsilon_2\,(E_{n2}) \cdot N_{target} \cdot N_{neutron} \end{aligned} \tag{3.1}$$

where

Y_{bu} = yields for the nd breakup reaction,
$d\Omega$ = solid angle of neutron detectors,
dS = bin width along the locus,
ϵ = neutron detector efficiency,
α = transmission of the scattered neutron flux,
N_{target} = number of target nuclei in the scatterer,
$N_{neutron}$ = number of 13 MeV neutrons incident on the target.

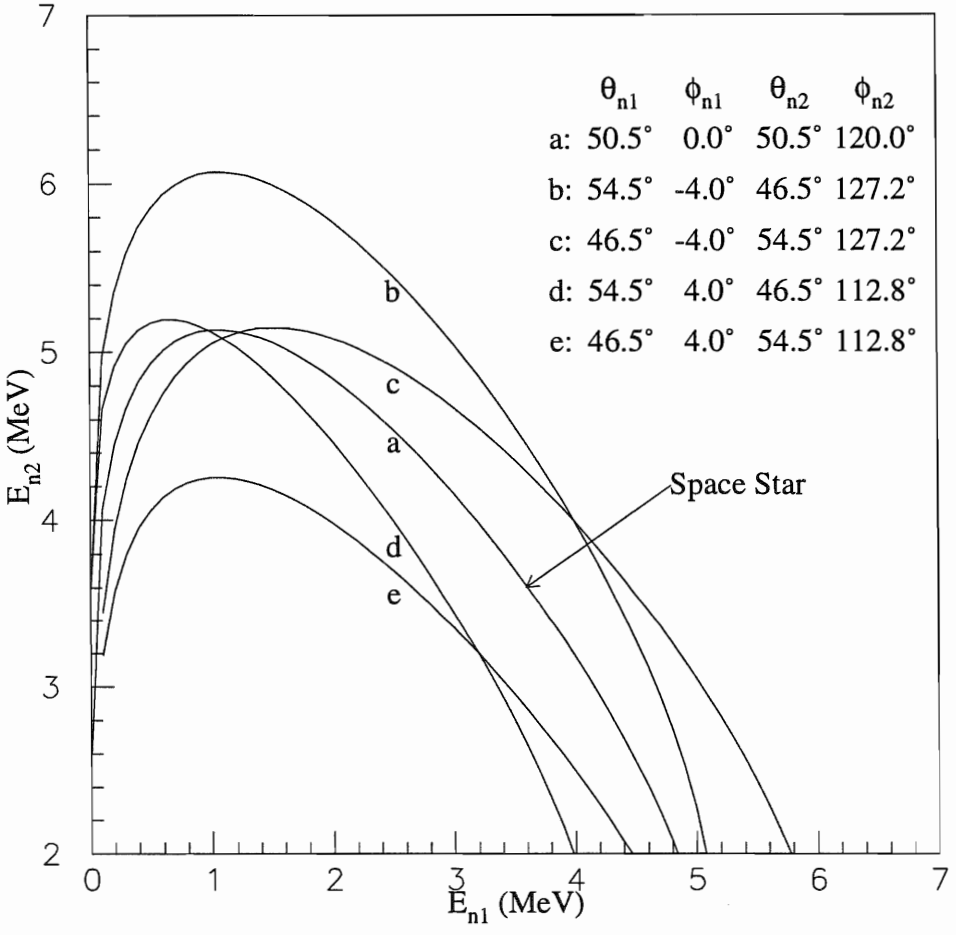

Figure 3.2: Finite geometry effects on kinematics for the SST configuration. All kinematic calculations were made with an incident neutron energy of 13.0 MeV.

The effective transmission and efficiency terms of Eq. 3.1 were calculated in the Monte-Carlo simulation. The details will be described in Sec. 3.3.3. The method used to project the data onto the ideal locus will be discussed in Sec. 3.3.4.

3.2 Elastic Scattering

The elastic scattering data were analyzed using the computer code DOUB.EVL. The pulse-height thresholds for all the neutron detectors were set in software to $\frac{1}{4}$ x Cs. Pulse shape discrimination was accomplished as described in Sec. 3.1.2. After meeting threshold and PSD conditions, a TOF spectrum was generated (see Fig. 3.3). A gate was set on the elastic scattering peak and for all events within that gate the center detector pulse-height (CDPH) spectrum was incremented. A second gate in the TOF spectrum was set on the accidental region before the γ-ray peak. Those events which fell in the accidental gate in the TOF spectrum were used to increment a second CDPH spectrum. The background underneath the true events (singly scattered nd elastic events) are due to accidentals and events which are multiply scattered in the center detector (see Fig. 3.4). After subtracting the accidentals, the multiple-scattering contributions were calculated in the Monte-Carlo simulation and subtracted.

Because the CDPH spectrum was used to determine the yields, it was necessary to consider the influence on the yields due to deuterons which did not deposit all their energy in the center detector. If the elastic scattering reaction takes place near the edge of the center detector, the recoiling deuteron may leave the scintillator cell before depositing all its energy in the detector. As the scattering angle of the neutron increases, the recoil energy of the deuteron also increases, which in turn increases the distance the deuteron must travel in the scintillator volume to deposit all its energy. These "edge effects" were calculated in the Monte-Carlo simulation to determine the percentage of the yields which were lost for each neutron scattering angle.

As can be seen in Fig. 3.6, the triple coincidence TOF spectra also include a peak due to elastic scattering. This peak was caused by a random event in one of the detectors in conjunction with an elastic event in the other. It was empirically determined that these triple coincidences were approximately 1% of the elastic yields for each detector. The coincidence rate between any two detectors depends on the counting rate in each detector (see Sec. 3.1.1), so the actual percentage of elastic yields

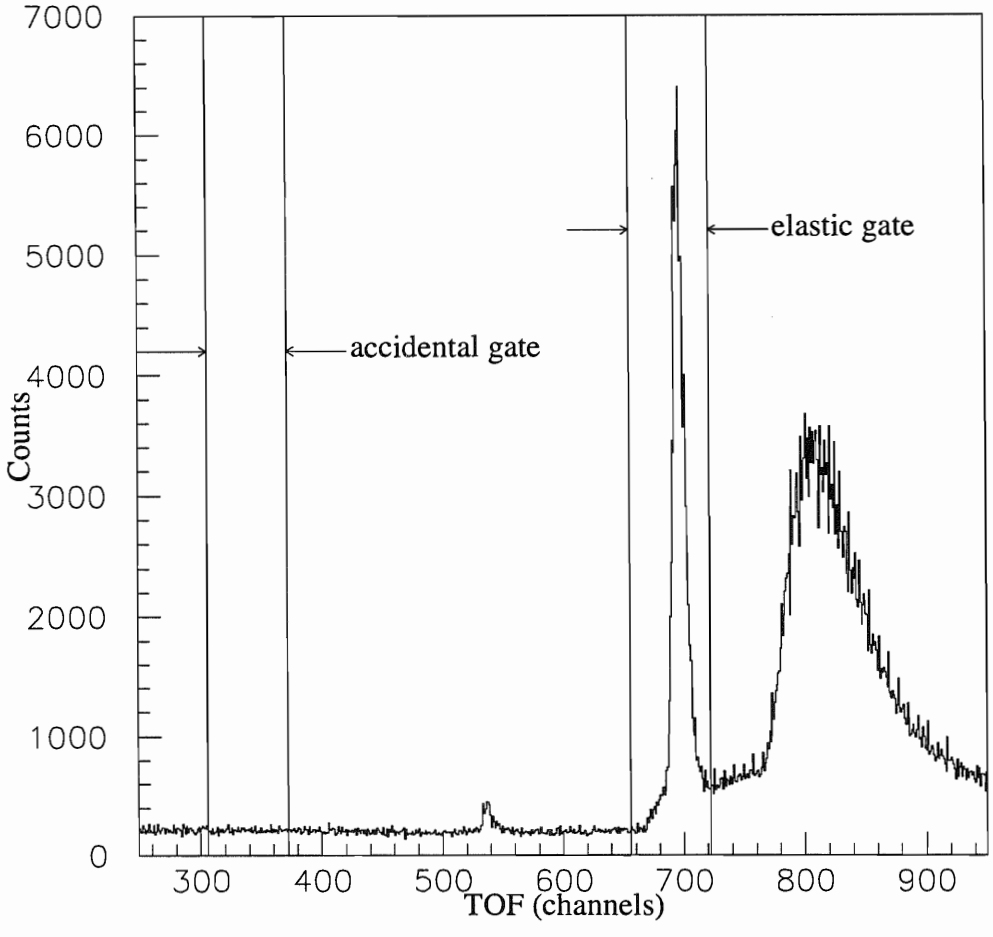

Figure 3.3: TOF spectrum for double coincidences. Time increases from left to right and the time calibration is .2 ns/channel. The small peak between the gates are the γ-rays which leak through the PSD cut. The large mound to the right of the elastic peak is the continuum of neutrons from nd breakup and nd elastic scattering of continuum neutrons from breakup reactions in the gas cell.

lost in this manner varied from detector to detector. During the elastic data sorting these events were recovered by incrementing the TOF spectra for each detector for triple coincidences and also for all double coincidences. The doubles were scaled down by a factor of 96 (see Sec. 3.2.2) during the data acquisition, therefore this same factor was applied to the triple coincidences in software for this analysis. After subtracting accidentals and multiple scattering and correcting for edge effects, the yields were obtained from the CDPH (low gain) spectrum for all but the 17° detectors. The deuteron recoil energy for neutrons scattering to the 17° detectors was below the lower-level threshold of the center detector.

3.2.1 Center Detector Light Response Function

In the analysis of the breakup data, it was necessary to calculate the energy of the proton detected in the center detector (see Sec. 3.3). The energy of the proton is related to the pulse height in the center detector (i.e. the light produced in the scintillator). It has been shown [Tor86] that the light response of an NE-232 scintillator to protons is related to the light response to deuterons by

$$L_p(E) = \frac{1}{2} L_d(2E), \tag{3.2}$$

where $L_p(E)$ is the light output of a proton of energy E and similarly for L_d.

Using the same spectra from which the elastic scattering yields were extracted, the centroid of the pulse-height peak was determined. This was done for all but the 17° detectors and using the center detector low gain pulse height. The 17° detectors were excluded because the recoil deuteron pulse height was below the hardware threshold of the low gain circuit. An unconditional center detector pulse-height spectrum was used to determine the recoil edge for nd elastic scattering to 180°. The centroid channel for each detector and the channel of the 180° recoil edge were plotted versus the recoil deuteron energy for elastic scattering (see Fig. 3.5). These data points were described using two analytical functions. Below 5.6 MeV the points were fit with a quadratic function of E. Above 5.6 MeV they were fit with a linear function of E. These functions were then used to calculate proton energies for the breakup data.

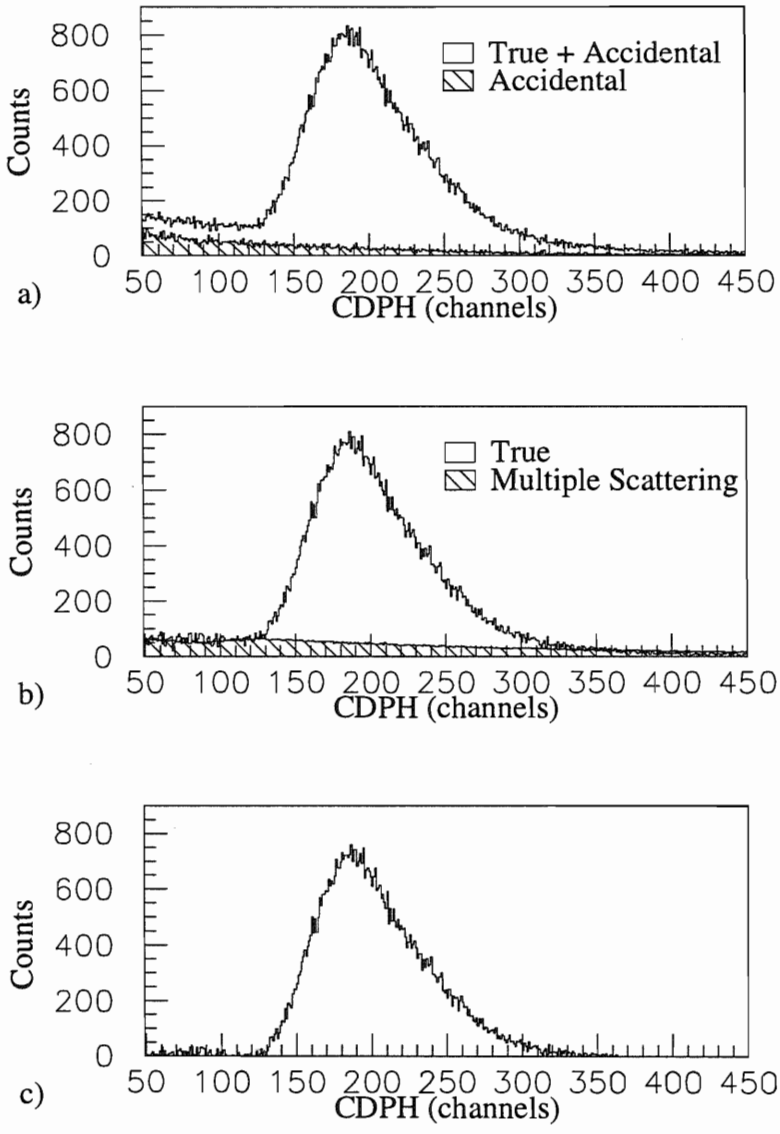

Figure 3.4: CDPH spectra for nd elastic scattering at 50.5°. a) The CDPH spectra for "true + accidental" and "accidental" events. b) The CDPH spectrum after subtraction of counts due to accidental events. The contribution from multiple scattering was calculated in the Monte-Carlo simulation. c) The final spectrum contains only singly scattered events after subtraction of accidentals and multiple scattering.

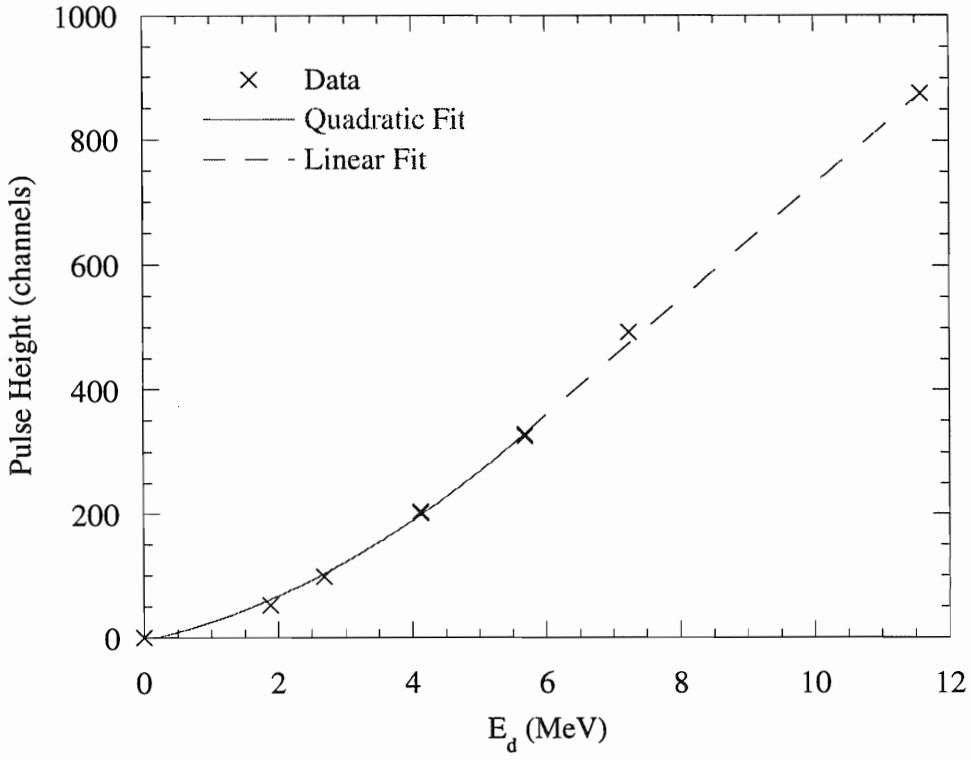

Figure 3.5: Center detector light response function.

3.2.2 Breakup Normalization

The elastic scattering yields at angle θ are related to the differential cross section in the lab by:

$$Y_{elas}(\theta) = \left(\frac{d\sigma}{d\Omega}(\theta)\right)_{lab} \cdot d\Omega \cdot \alpha\ (E_{elas}) \cdot \epsilon\ (E_{elas}) \cdot N_{target} \cdot N_{neutron} \qquad (3.3)$$

Of these factors, only $N_{target} \cdot N_{neutron}$ was unknown: the yields were extracted as explained previously, the differential cross section for elastic scattering is well known for these angles [Wit89b], the neutron detector efficiencies were measured independently (see App. A), the solid angle depends on the detector size and flightpath, and the transmission was calculated in the Monte-Carlo simulation from well-known neutron total cross sections.

The computation of the breakup cross section from the breakup yields also depends on the the product of $N_{target} \cdot N_{neutron}$ (see Eq. 3.1), therefore Eq. 3.3 for nd elastic

scattering was rearranged to extract a value for this product from the elastic yields in each neutron detector, with the exception of the 17° detectors.

$$\beta_{det} \equiv N_{target} \cdot N_{neutron} = \frac{Y_{elas}(\theta)}{\left(\frac{d\sigma}{d\Omega}(\theta)\right)_{lab} \cdot d\Omega \cdot \alpha\ (E_{elas}) \cdot \epsilon\ (E_{elas})} \tag{3.4}$$

Two other corrections were necessary. During the data acquisition the doubles were divided by a factor of ~100 to reduce the data rate at the computer. The actual factor was determined from two scalers. The first scaler counted the input to the divide-down circuit and the second counted the output. The ratio of these two scalers gave the actual scale factor of 96. This scale factor had to be applied to the yields extracted from the data. The second correction was a result of the fact that during data acquisition it was necessary to set the lower-level discriminator of the ADC below the threshold of the neutron detector CFDs. Because of this the ADC would sometimes trigger on a false peak detection signal [Sil93] resulting in a pulse height of zero for the event. The effect was measured using the LED pulsers and checked again using np elastic scattering. The correction factors were extracted from the unconditional pulse-height spectrum for each neutron detector during the analysis and applied to the yields for the corresponding set of runs.

The yields were extracted for each neutron detector from the center detector pulse-height spectrum gated by a window in the TOF spectrum of that neutron detector. Because these data were accumulated over several months, there were slight differences in the gain of the amplifiers for the pulse height. Due to these gain changes the data were analyzed in seven batches. Light response functions were calculated and yields extracted for each batch of data. Yields for each of these batches were then handled separately. Because different batches were for different counting times the normalization factor for each batch of runs was divided by the associated BCI to permit comparison of the factor for different batches. The normalization factor is given below in Eq. 3.5.

$$\beta_{det} = \frac{Y_{elas}(\theta) \cdot \text{scale factor} \cdot \text{ADC correction}}{\left(\frac{d\sigma}{d\Omega}(\theta)\right)_{lab} \cdot d\Omega \cdot \alpha\ (E_{elas}) \cdot \epsilon\ (E_{elas}) \cdot \text{BCI}} \tag{3.5}$$

An advantage of normalizing to the elastic scattering yields was that it enabled the extraction of five independent normalization factors (β_{det}) for each batch of data. Because the value of the normalization factor determined from each detector should be

Runs	kBCI	$\overline{\beta}$	error	deviation
1106–1194	17200	1622.140	± 12.791	± 53.521
1197–1525	64086	1633.279	± 12.879	± 50.026
1540–1743	38727	1637.133	± 12.910	± 55.324
1757–1774	3600	1598.366	± 12.604	± 17.704
1777–1818	8200	1643.523	± 12.960	± 44.914
1824–2201	71700	1667.616	± 13.150	± 55.328
2219–2485	50403	1704.097	± 13.438	± 53.826

Table 3.1: The cross-section normalization calculated for each batch of data with statistical error and standard deviation.

identical, the deviation of the values was a measure of the systematic errors associated with this method. For each batch of data, the individual detector values of β_{det} were statistically averaged to obtain a value for $\overline{\beta}$. The deviance of the values for each detector (β_{det}) from $\overline{\beta}$ was then assigned as the systematic error for $\overline{\beta}$.

Using Eq. 3.5 made it possible to compare the values calculated for each batch of data, however it must be noted that the BCI is related to the neutron flux by the deuterium gas pressure in the neutron production cell. This means that the values of $\overline{\beta}$ calculated for each batch of data could differ by an amount proportional to the average gas cell pressure of each batch. Table 3.1 shows the values and errors for each $\overline{\beta}$.

When calculating the statisical uncertainty for each β_{det} it was found that the errors in the scale factor, ADC correction and the BCI were neglible. The statistical error for each β_{det} is given by

$$\left(\frac{\Delta\beta_{det}}{\beta_{det}}\right)^2 = \left(\frac{\Delta Y_{elas}}{Y_{elas}}\right)^2 + \left(\frac{\Delta\sigma_{elas}}{\sigma_{elas}}\right)^2 + \left(\frac{\Delta d\Omega}{d\Omega}\right)^2 + \left(\frac{\Delta\alpha}{\alpha}\right)^2 + \left(\frac{\Delta\epsilon}{\epsilon}\right)^2$$

The uncertainty in the solid angle was due to the uncertainty in the flightpath which was assumed to be ±5 mm. The shape of the neutron-detection efficiency curve as a function of energy was determined in an independent measurement (see Appendix A to ±1%. The transmission of the scattered neutron flux was calculated to an accuracy of ±1.3%. The main uncertainty in the calculated transmission was due to the uncertainties in the neutron total cross sections for the scatterer constituents (carbon, deuterium, hydrogen, silicon and oxygen). The statistical error in the normalization

was calculated as described above and is shown in Table 3.1. The statistical error for each batch was less than ±0.8%. The deviation of the normalizations was less than ±3.5% and reflects the systematic error associated with this method.

3.3 Breakup Data Analysis

The breakup data reduction was performed using the software code TRIP.EVL. Pulse-shape discrimination was performed as described in Sec. 3.1.2. The pulse-height threshold for each neutron detector was set to $\frac{1}{4}$ x Cs (this corresponds to a neutron energy of about 0.5 MeV) for the SST and COLL configurations and to $\frac{1}{2}$ x Cs (neutron energy of about 1.0 MeV) for the CST configuration. Due to differences in the kinematic constraints of the configurations, the recoil proton pulse height was handled in three different ways. Because in the SST configuration the recoil proton energy is always greater than 3.5 MeV, a lower-level threshold was set on the pulse-height spectrum for the center detector to correspond to approximately 2 MeV protons. For the CST configuration the situation is reversed; the proton energy never exceeds 4 MeV. In this case an upper limit was set at 7 MeV. These values take into consideration the energy resolution of the center detector and finite geometry effects. Each of the COLL configurations was analyzed with no constraints on the proton energy in order to span the dynamic range necessary to cover the kinematic region of interest.

All events which fulfilled all these requirements were used to increment the appropriate TOF spectra. Fig. 3.6 shows the TOF spectra for a configuration. The gates shown in the figure were used to distinguish between accidentals and true events. The gate set around the "True + Accidental" events will be referred to as "gate 1" and the gate around the "Accidental" events will be referred to as "gate 2" in the following discussion.

3.3.1 True + Accidentals

All the events which met the pulse-height and PSD requirements discussed above and which had neutron TOF that fell inside gate 1 for *both* detectors were considered to be the "True + Accidental" events. For those events the difference in the TOF between the two neutrons (ΔTOF) was calculated. (It was originally proposed to use the

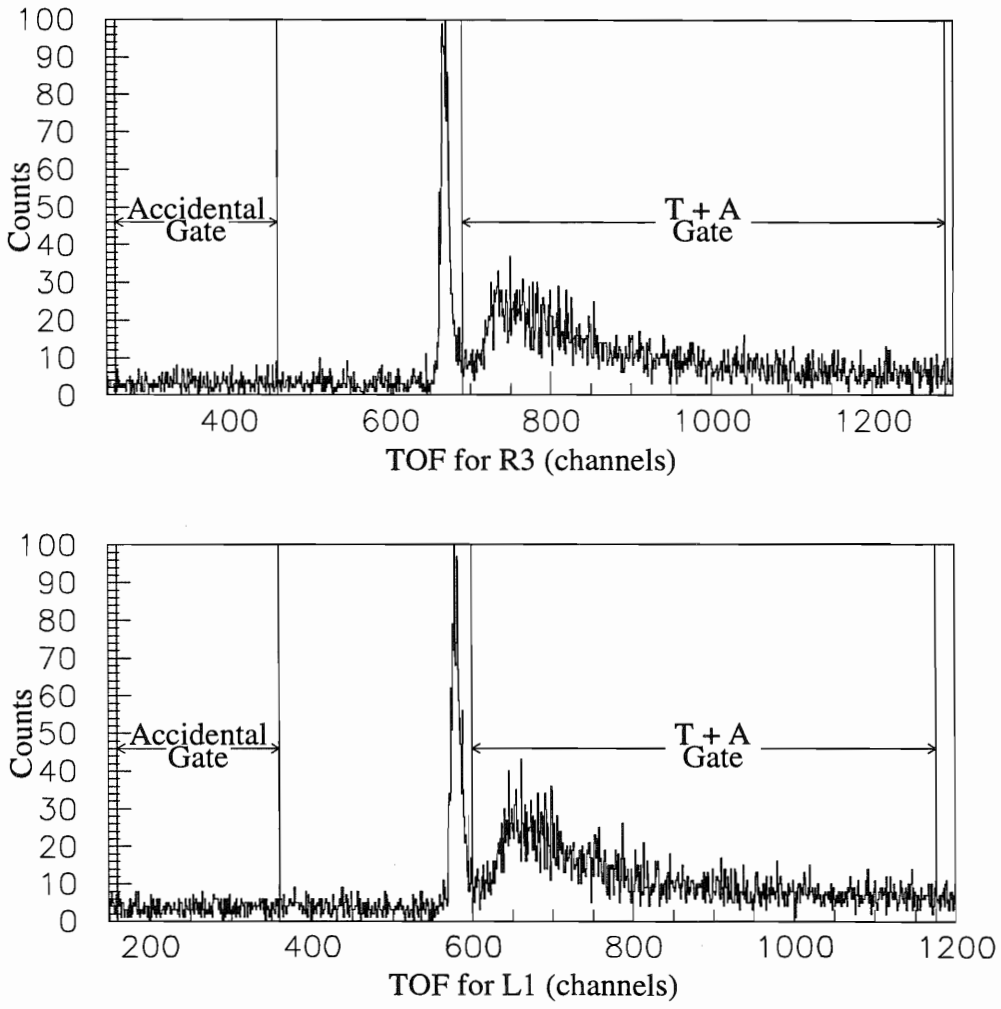

Figure 3.6: Triple-coincidence TOF spectra for the two neutron detectors used in the SST configuration (θ_{R3}=50.5°, ϕ_{R3}=0.0°, θ_{L1}=50.5°, ϕ_{L1}=120.0°). Note: This is only a fraction of the data.

ΔTOF spectra as a means of reducing the accidentals in the region of interest. Later analysis proved this to be unnecessary, however the ΔTOF is mentioned because it was one of the parameters written to the new event file.) The neutron TOF values and the recoil proton pulse height were then passed to a subroutine for conversion to energy. The TOF values were converted to energy using the measured time calibration of the TOF spectra and the average flightpath of each neutron detector (center-to-center distance from the scatterer to each neutron detector). The recoil proton pulse height was converted to energy using the center detector light response function (see Sec. 3.2.1). The subroutine returned all three particle energies and the sum of those energies (total energy).

The total energy was used to increment a spectrum (see Fig. 3.7). A very wide gate was set on this spectrum to reduce the volume of the data, by mainly cutting events produced by gas cell breakup neutrons. For the events which fell inside the total energy gate, six parameters were written to a new event file:

1. A routing signal to identify the detectors involved in the coincidence event (i.e. which kinematic configuration).

2. A routing signal to flag that both neutron TOFs fell inside gate 1.

3. The energy of neutron one.

4. The energy of neutron two.

5. The energy of the proton.

6. The difference in TOF of the neutrons.

By writing these events to a new file there was a tremendous reduction in the volume of the data. The new event files were only six words per event in comparison to twenty-two words per event for the original files. The new files did not contain any double coincidences and only the triples associated with the kinematic configurations of interest. The PSD requirement eliminated almost all events due to γ-rays. The total energy cut removed most of the events caused by neutrons produced by breakup reactions in the gas cell. All these effects reduced the volume of the event files by almost four orders of magnitude.

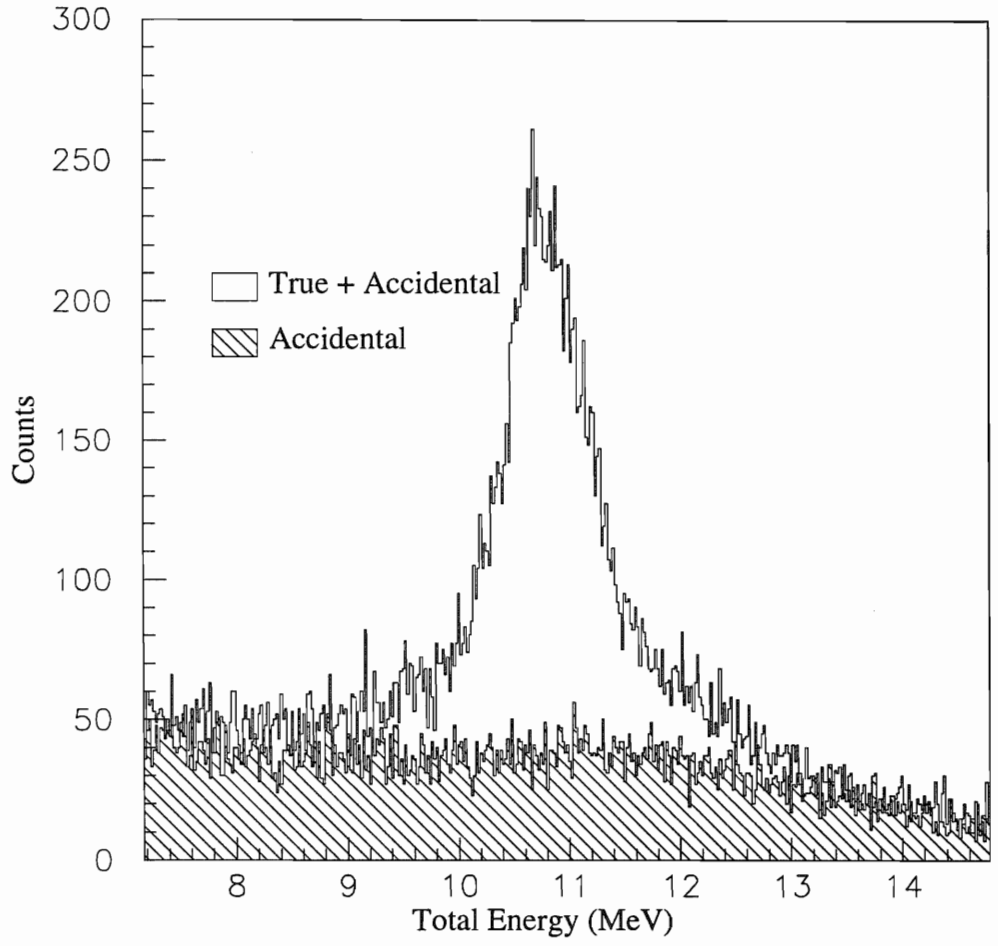

Figure 3.7: Total energy spectrum for SST. The gate on this spectrum used to produce the new event files was wider than the portion of the spectrum shown in this figure.

3.3.2 Accidentals

Gate 2 in each of the TOF spectra was set in the accidental region between the beginning of the TOF spectrum and the position of the γ peak and the gate width was generally 1/2 the width of gate 1 (in some cases it was 1/3 due to the size of the accidental region). Because the events falling inside gate 2 are unphysical (i.e. the TOF is shorter than that of the γ-rays), the energy of these neutrons cannot be determined from their position in the TOF spectrum. To use this portion of the TOF spectrum to obtain information on accidental events, the TOF position of gate 2 must be shifted to cover the same neutron energy range as the events falling in gate 1. In determining the accidental coincidences, three possibilities were considered.

1. an event in gate 1 for the right detector and gate 2 for the left detector.
2. an event in gate 2 for the right detector and gate 1 for the left detector.
3. an event in gate 2 for both detectors.

The first two cases were handled identically. The TOF value from gate 2 was increased by an amount such that it appeared to be in gate 1. For example, if the lowest channel of gate 1 was 700 and the lowest channel of gate 2 was 100, then the TOF was increased by 600 channels. Using the new TOF value the ΔTOF and the particle energies were calculated exactly as for the true + accidental events. All the same cuts were applied to the event until it was eventually written to the new event file with a routing signal to identify it as an accidental event.

Because gate 2 was only half the width of gate 1 this only accounted for the first half of the necessary range of neutron energies. Therefore the TOF for the accidental particle was again increased by an additional offset equal to the width of gate 2. This shifts the TOF value to the other half of gate 1. All the same cuts were again applied until the new event file was written.

If the TOF fell in gate 2 of *both* detectors a somewhat different method was used. The event was processed only once, but the ΔTOF and neutron energies were calculated differently. These values were normally calculated from the TOF channel number by a FORTRAN subroutine. The flightpath of the neutron, the channel number of the γ-ray and the time calibration of the spectrum were known, so it was simple to calculate the neutron TOF (in ns) and from that the neutron energy. For

the events which fell in gate 2 of both detectors, the time calibration was adjusted to cover the same range of TOFs as gate 1 and the TOF values were shifted to cover the same neutron energy range as events in gate 1. The same cuts were applied to these events and they were written to the new event file with a routing signal to identify them as random-random events.

In order to test this method of handling accidentals, data were sorted for triple coincidences involving the out-of-plane detector and the 62.5° detector on the same side of the beam axis (i.e. R1-R4, L1-L4). This configuration is kinematically not allowed, therefore all the events must be from accidental coincidences. After sorting these data as described above, the total-energy spectrum of the accidental events was subtracted from the total-energy spectrum containing the true + accidental events. The resulting difference spectrum was not statistically different from zero.

3.3.3 Monte-Carlo Simulation

One of the reasons for simulating the experiment was to determine the total transmission of the scattered neutron flux to the neutron detectors. The transmission depends on the neutron total cross sections for the materials through which the neutron passes and the distance travelled through those materials. For elastic scattering this was a relatively straightforward computation. In the case of the breakup calculations the spread of the data about the ideal locus complicates the matter. It was decided to calculate the *product* of the transmissions of the two neutrons.

In the Monte-Carlo simulation, points were randomly selected in each of the three detectors. These points determine the neutron scattering angles and with the incident neutron energy they determine a kinematic locus. The three particle energies for a single history were then determined by stepping along the locus in 100 keV steps of arc length, S. For each event-history in the Monte-Carlo simulation, the product of the two neutron transmissions was calculated, however the particle energies (E_{n1},E_{n2},E_p) were not necessarily identical to what would be calculated from the experimental data. The randomly selected points in each detector defined the neutron flightpaths and the neutron energies were used to compute the TOF for each of the neutrons for each history. The experimental data were treated differently. The neutron TOF values were used to calculate the particle energies by assuming the flightpath was the

center-to-center distance from the scatterer to the neutron detector. Therefore, in the Monte-Carlo simulation the real TOF for each history was converted to a new energy (E'_{n1},E'_{n2}) by using the center-to-center distance for the flightpath instead of the distance between the points in the simulation.

The experimental uncertainty in the proton energy was reproduced by fitting the total-energy (E_{tot}) spectrum with a Gaussian distrubution. The proton energy from the Monte-Carlo simulation was smeared such that the sum, $E'_{n1} + E'_{n2} + E'_p$, reproduced the experimental E_{tot} spectrum. These three values were then used to index the product of the transmission values for both neutrons calculated from the real energies and flightpaths: This value for $\overline{\alpha}$ was then averaged into an array indexed by the three particle energies, E'_{n1}, E'_{n2}, E'_p, which was the output of the Monte-Carlo code.

$$\overline{\alpha}\ (E'_{n1}, E'_{n2}, E'_p) \equiv \alpha_1\ (E_{n1}) \cdot \alpha_2\ (E_{n2}) \tag{3.6}$$

By retaining the array in 250 keV energy bins, the transmission could be projected in the same manner as the experimental data.

The product of the two neutron detector efficiencies was similarly indexed by the three particle energies in an output array.

$$\overline{\epsilon}\ (E'_{n1}, E'_{n2}, E'_p) \equiv \epsilon_1\ (E_{n1}) \cdot \epsilon_2\ (E_{n2}) \tag{3.7}$$

Figure 3.8 shows the magnitude of these two corrections (efficiency and transmission) when projected onto the point scattering kinematic locus. The Monte-Carlo code also calculated a weighting factor (w) which was obtained from the normalized Gaussian used to smear the proton energies. The use of these output arrays will be explained in Sec. 3.3.4. Figure 3.9 shows these two output arrays plotted versus the two neutron energies.

Rather than attempting to disentangle the finite geometry effects and extract a point-scattering cross section, it was decided to treat the theoretical calculations in the same manner as the experimental data. Rigorous Faddeev calculations with the Bonn-B OBEPQ were made over the finite geometry of the experiment. Calculations were made at three incident neutron energies, 12.8, 13.0 and 13.2 MeV to cover the neutron energy spread from the gas cell. Table 3.2 shows the angular range and step size for the calculations for each configuration. For each of these angle and energy combinations, the cross section and neutron energies were calculated in 100 keV steps

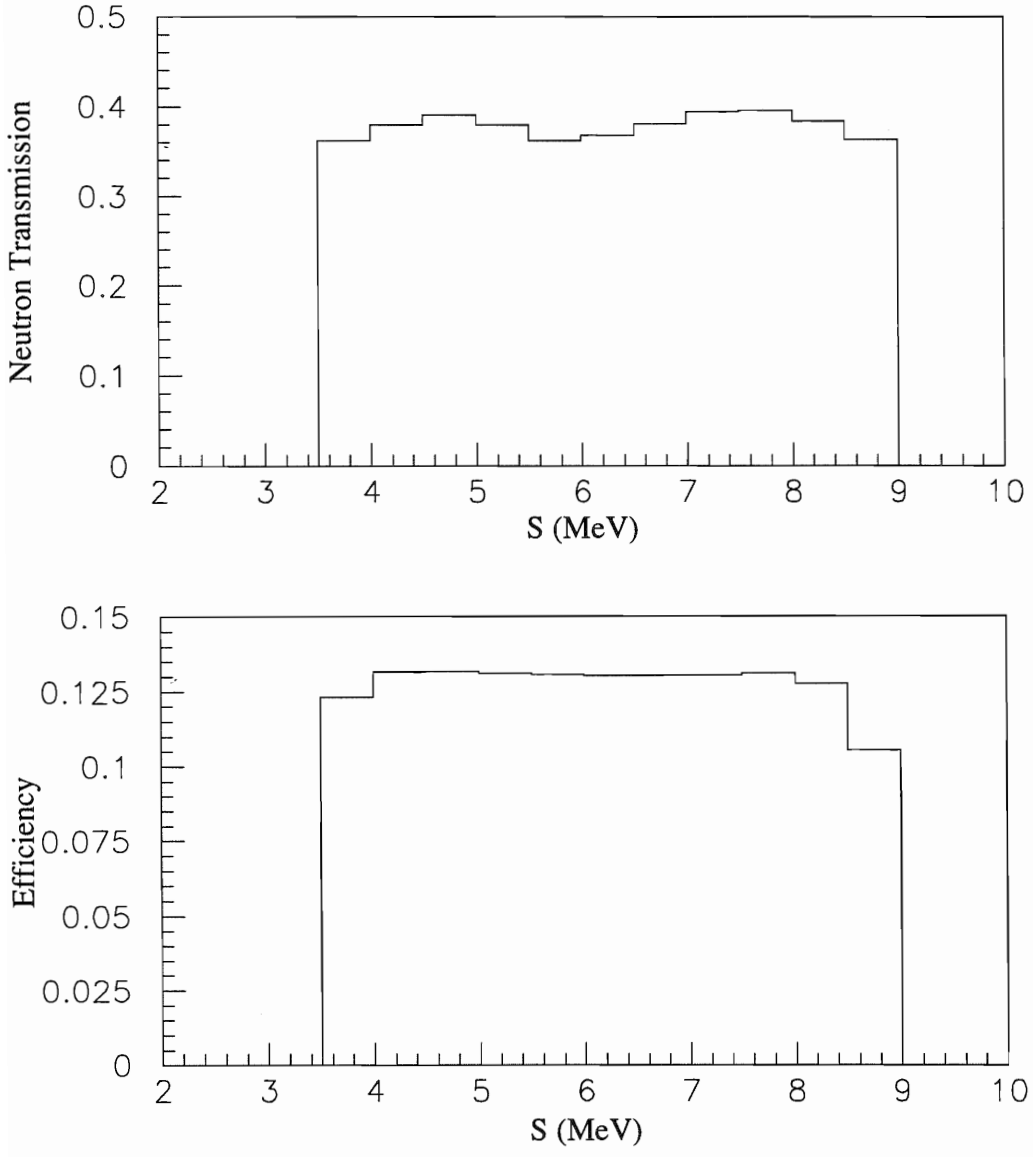

Figure 3.8: (Top) Product of the two neutron transmissions and (bottom) product of the two neutron detector efficiencies for the SST after projection onto the kinematic locus.

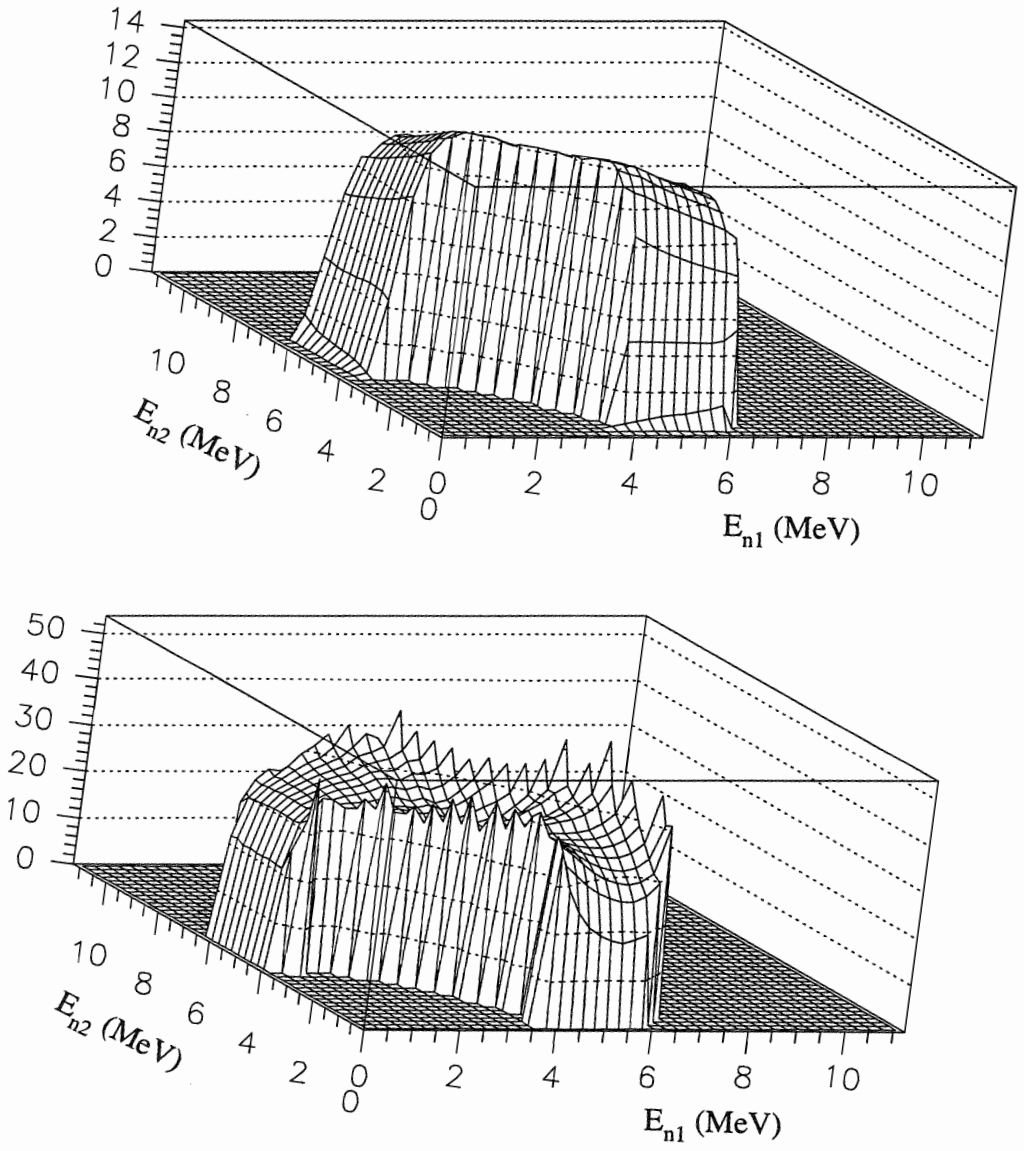

Figure 3.9: Monte Carlo output arrays ($\times$ 100) for detector efficiency (top) and neutron transmission (bottom).

Configuration	θ_{n1}	$\Delta\theta_{n1}$	θ_{n2}	$\Delta\theta_{n2}$	ϕ_{12}	$\Delta\phi_{12}$
SST	46.0°–55.0°	1.5°	46.0°–55.0°	1.5°	104.0°–136.0°	2.0°
CST	12.5°–21.5°	1.5°	46.0°–55.0°	1.5°	165.0°–195.0°	3.0°
COLLa	46.0°–55.0°	1.5°	58.0°–67.0°	1.5°	165.0°–195.0°	3.0°
COLLb	34.5°–43.5°	1.5°	71.0°–80.0°	1.5°	168.0°–192.0°	3.0°

Table 3.2: Angular range and step size for theoretical calculations used to produce Monte-Carlo cross-section libraries.

in arc length along the locus. These files were then used by the Monte-Carlo code as a library of cross-section values as a function of E_{inc}, θ_{n1}, θ_{n2}, and ϕ_{12}. For each angle and energy combination approximately 150 cross section points were calculated and the entire library for each configuration consisted of ~300,000 cross section values.

For each history in the Monte-Carlo simulation the closest values in the library for E_{inc}, θ_{n1}, θ_{n2}, and ϕ_{12} were determined. The code then minimized the difference

$$(E_{n1}^{history} - E_{n1}^{library})^2 + (E_{n2}^{history} - E_{n2}^{library})^2$$

The cross-section value from the library at the minimum point was then multiplied by the weight factor (w). The product ($\mathcal{W}$) was then indexed to an output array in the same manner as the transmission and efficiency.

$$\mathcal{W}(E'_{n1}, E'_{n2}, E'_p) \equiv \sigma(E_{n1}, E_{n2}) \cdot w \tag{3.8}$$

Using all these output arrays, the theoretical cross section could then be projected identically to the experimental data.

$$\frac{d^3\sigma}{d\Omega_1 d\Omega_2 dS}(S) = \frac{\sum_i(\overline{\alpha} \cdot \overline{\epsilon} \cdot \mathcal{W})_i}{\sum_i(\overline{\alpha} \cdot \overline{\epsilon} \cdot w)_i} \tag{3.9}$$

where the summation is over the points from the array projected to each bin in S.

3.3.4 Data Projection and Cross-Section Determination

The data projection onto the ideal locus was accomplished using an EVAL code for each configuration and using the event files generated as described in Sec. 3.3.1. The first step was to calculate the total energy (E_{tot}) and set a tight gate about the

peak at 10.775 MeV. For all events which passed this gate requirement, the three arrays generated by the Monte-Carlo simulation were used to calculate the product, $\overline{\alpha} \cdot \overline{\epsilon} \cdot \omega$. If $\overline{\alpha} \cdot \overline{\epsilon} \cdot \omega$ was zero, then the event was rejected. This was equivalent to using the Monte-Carlo simulation to generate a three dimensional gate over the kinematic region of interest in E_{n1}-E_{n2}-E_p space. If $\overline{\alpha} \cdot \overline{\epsilon} \cdot \omega$ was non-zero, the particle energies were converted to momentum by

$$k_i = \sqrt{2mE_i}$$

where it was assumed that $m_n = m_p$. The event was then projected onto the nearest point on the locus by minimizing the quantity:

$$(k_{n1}^{ideal} - k_{n1})^2 + (k_{n2}^{ideal} - k_{n2})^2 + (k_p^{ideal} - k_p)^2 \tag{3.10}$$

where the superscript *ideal* refers to the point-scattering locus and the terms with no superscript refer to the data event being analyzed. The data were binned in 500-keV steps of arc length S. This method was used to produce both "True + Accidental" and "Accidental" spectra (see Fig. 3.10). After subtraction of accidentals, the yields for the breakup reaction were extracted as a function of S.

Two other arrays were generated as a function of S during the sorting:

$$\mathcal{F}(S) \equiv \sum_i (\overline{\alpha} \cdot \overline{\epsilon} \cdot \omega)_i \tag{3.11}$$

$$\mathcal{G}(S) \equiv \sum_i \omega_i \tag{3.12}$$

where the summation was over each point projected into a specified bin along the S-curve. These two arrays were then used to determine the product of the transmissions and efficiencies for each point on the locus.

Combining Eqs. 3.1, 3.4, 3.6 and 3.7, the cross section can be written as:

$$\frac{d^3\sigma}{d\Omega_1 d\Omega_2 dS} = \frac{Y_{bu} \cdot \text{ADC correction}}{d\Omega_1 \cdot d\Omega_2 \cdot dS \cdot \overline{\alpha} \cdot \overline{\epsilon} \cdot \overline{\beta} \cdot \text{BCI}} \tag{3.13}$$

For each point on the locus:

$$\overline{\alpha} \cdot \overline{\epsilon} = \frac{\mathcal{F}(S)}{\mathcal{G}(S)}$$

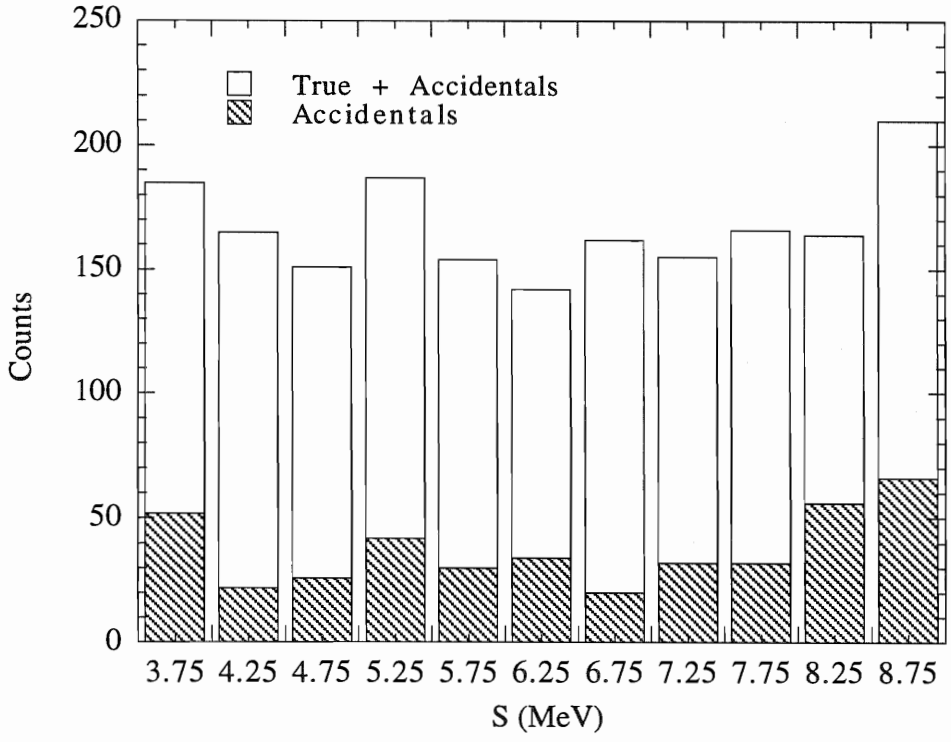

Figure 3.10: "True + Accidental" and "Accidental" yields projected onto the locus for SST. Note: this is only a fraction of the data.

Substituting this into Eq. 3.13, the cross section becomes:

$$\frac{d^3\sigma}{d\Omega_1 d\Omega_2 dS} = \frac{Y_{bu} \cdot \text{ADC correction} \cdot \mathcal{G}(S)}{d\Omega_1 \cdot d\Omega_2 \cdot dS \cdot \mathcal{F}(S) \cdot \overline{\beta} \cdot \text{BCI}} \tag{3.14}$$

The uncertainty in the measured cross section is given by:

$$\left(\frac{\Delta\sigma}{\sigma}\right)^2 = \left(\frac{\Delta Y_{bu}}{Y_{bu}}\right)^2 + \left(\frac{\Delta d\Omega_1}{d\Omega_1}\right)^2 + \left(\frac{\Delta d\Omega_2}{d\Omega_2}\right)^2 + \left(\frac{\Delta\overline{\beta}}{\overline{\beta}}\right)^2 + \left(\frac{\Delta\alpha_1}{\alpha_1}\right)^2 + \left(\frac{\Delta\alpha_2}{\alpha_2}\right)^2 + \left(\frac{\Delta\epsilon_1}{\epsilon_1}\right)^2 + \left(\frac{\Delta\epsilon_2}{\epsilon_2}\right)^2 \tag{3.15}$$

The uncertainties in the solid angles were due to the uncertainty in the flightpaths which were measured to a precision of ± 5 mm. The shape of the neutron-detection efficiency curve as a function of energy was determined as described in Appendix A to an accuracy of $\pm 1\%$. The uncertainty in the calculated transmission of the scattered neutron flux was $\pm 1.3\%$ and was mainly due to the uncertainty in the neutron total cross-section data used in the Monte-Carlo simulation. The uncertainty in the normalization was calculated as described in Sec. 3.2.2 and is shown in Table 3.1. Just as for the elastic scattering data, the cross section was calculated in batches which were then statistically averaged to obtain the final result. Because the data was analyzed in seven batches and the cross section was calculated independently for each batch, the counting statistics dominate the uncertainty for each batch.

Chapter 4

Meson-Exchange Theory and Calculations

Rigorous Faddeev calculations using as the N-N potential the Bonn-B OBEPQ were performed by Dr. Henryk Witała for comparison to the experimental data obtained in this thesis project. This chapter will describe the methods used for these calculations and will give some background on the different meson-exchange potentials, in particular the Bonn-B potential. Before describing the three-nucleon calculations which were performed for this work, a brief review of concepts from two-nucleon scattering will be necessary. Formal development of the concepts discussed here can be found in [Glö83]. These concepts will then be used in the discussion of the methods employed in three-nucleon calculations.

4.1 Meson-Exchange Potentials

In order to create a potential model of the NN interaction it is first necessary to determine what the properties of the interaction must be. There are five empirical features of the NN interaction which must be reproduced by any potential model:

1. The nuclear force is of short range,
2. The nuclear force is attractive in the intermediate range ("intermediate" refers to the total range of the nuclear force, which is subdivided into three parts, short, intermediate and long range),

3. The nuclear force includes a repulsive core,

4. The nuclear force includes a tensor force,

5. The nuclear force includes a strong spin-orbit force.

In the 1930's the most striking feature of the nuclear force was the short range of the interaction. In 1935 Yukawa proposed, in analogy to quantum electrodynamics (QED), that this could be explained by the exchange of a particle of *nonzero* mass. This was the birth of the meson-exchange picture of the nuclear force. Meson-exchange theory was originally believed to represent the strong interaction in strict analogy to QED. Today, however quantum chromodynamics (QCD) is the most widely accepted theory of the strong interaction, and meson-exchange theory is assumed to be an *effective* description which represents the full and fundamental theory in the regime of low-energy nuclear physics.

The next step is to consider real mesons and the effects they will produce. In the mass range below the nucleon mass there are five nonstrange mesons, π, η, ρ, ω and δ. The large mass of the δ and its small coupling constant minimizes its contribution to the force. Similarly, the contribution of the η is generally considered neglible in comparison to the pion contribution. The pion, as the lightest meson, provides the long-range force and due to its pseudoscalar nature, the tensor force. This tensor force is reduced at short range by the ρ meson. The ω creates the spin-orbit force and the short range repulsion.

One important part of the nuclear force is still left unexplained, the intermediate attraction. A boson with a mass of 500-700 MeV could explain this contribution. However there is no experimental evidence to support the existence of such a boson. Therefore in the present picture, the intermediate attraction is provided by 2π exchange terms. For the purpose of creating a one-boson exchange potential, the effects of the multiple-meson exchange can be described with a fictitious scalar boson of mass $\sim$ 500 MeV (commonly called the σ meson). The mass and the coupling constants of the σ meson are free parameters that are adjusted to fit the NN experimental data.

The one-boson-exchange-potentials (OBEPs) from the Bonn group use the above four mesons $(\pi, \rho, \omega, \sigma)$ to fit NN data. The differences between the various Bonn potentials (Bonn-A, Bonn-B and Bonn-C) arise from the different values for the

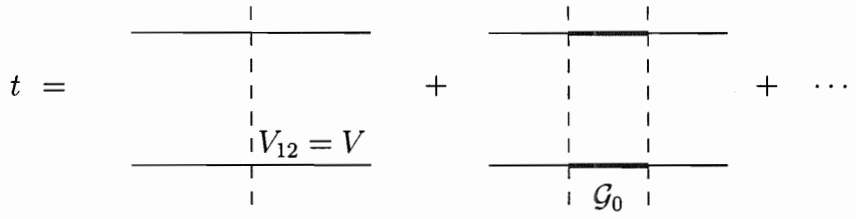

Figure 4.1: Two-Nucleon transition operator. The dashed line indicates the interaction of the two nucleons by the potential, V. Between interactions the particles are assumed to propagate freely with the free particle propagator defined as $\mathcal{G}_0 = (E - i\varepsilon - H_O)^{-1}$.

meson-nucleon coupling constants used for each potential. The values of the coupling constants are constrained by experimental meson-nucleon scattering data. For the Bonn potential, the fictitious σ-meson mass and coupling constant were adjusted and minor adjustments were made to the real meson coupling constants to reproduce n-p phase-shift data. The Paris potential is also based on a meson-exchange picture of the NN interaction. In the case of the Paris potential, the one-pion, two-pion and one-omega exchange contributions are added to a phenomonological core to reproduce p-p phase-shift data. Although the Paris and Bonn-B potentials differ significantly in the details of their origins, both potentials do a superb job of describing NN phase shift data.

4.2 Scattering Theory Review

If it is assumed that the interaction between two particles is finite in range (i.e. the interaction potential, V, goes to zero beyond some bounded domain D in space), we can then assume that the interaction between the two particles is the infinite sum of two-body interactions with free propagation of the particles between the interactions as described by $\mathcal{G}_0$, the free particle propagator. Figure 4.1 shows a diagram of the transition operator, t, for this type of interaction. We can then write the equation for t as

$$t = V + V\mathcal{G}_0V + V\mathcal{G}_0V\mathcal{G}_0V + \ldots \tag{4.1}$$

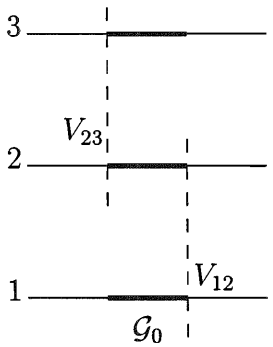

Figure 4.2: For scattering in the three-nucleon system, it is assumed that only two particles interact at any time and the particles freely propagate between the interactions. The nucleons are denoted by the numbers 1, 2 and 3.

or by a simple factoring as

$$t = V + V\mathcal{G}_0(V + V\mathcal{G}_0V + \ldots) \tag{4.2}$$

The infinite sum in parentheses in Eqn. 4.2 can then be recognized as the definition of the transition operator from Eqn. 4.1. We can then write the transition operator as

$$t = V + V\mathcal{G}_0t \tag{4.3}$$

which is the Lippmann-Schwinger equation for the transition operator, t. In practical applications what is needed is an expression for the transition matrix (T-matrix). The cross section is determined through the T-matrix. We can rewrite the Lippmann-Schwinger equation in an integral form which provides us with the T-matrix.

$$T_{q'q} = \langle \vec{q} \mid V \mid \vec{q}\,' \rangle + \lim_{\varepsilon \to 0} \int dq'' \langle \vec{q} \mid V \mid \vec{q}\,'' \rangle \frac{T_{q''q'}}{E_{q'} - i\varepsilon - E_{q''}} \tag{4.4}$$

The relationship between the differential cross section and the T-matrix is given by

$$\frac{d\sigma}{d\Omega} = \frac{(2\pi)}{\hbar} \rho(\vec{q}) \mid T_{q'q} \mid^2 \tag{4.5}$$

where $d\Omega$ is the solid angle into which the particles are scattered and ρ is the density of final states.

4.3 Three Nucleon Scattering

For the case of three nucleons, we use the same basic idea as for two nucleons. The contributions of pairwise interactions, V_{ij}, are summed, with free propagation between the interactions (see Fig. 4.2).

The reordering of these interactions produces the multiple scattering series (MSS) in which the interactions for each pair of nucleons are summed up to infinite order into the two-nucleon transition operators, t_{ij}. This is done by performing partial summations and using the Lippmann-Schwinger equation to relate the potential to the transition operator. However, even the sum of processes with one, two, three, ... 2N transition operators cannot be truncated at low energies due to the strength of the nucleon-nucleon interactions. In the case of scattering a neutron from a deuteron at high energies, we expect the neutron to strike one constituent of the deuteron and then leave without further interactions. This is the kinematical region where the so-called impulse approximation is thought to be valid. However, for lower energies, the probability for two, three, or more collisions increases and the predictions of the impulse-approximation calculations have little resemblance to reality. For this reason the entire MSS must be computed to make valid comparisons to low-energy 3N data.

If it is assumed that nucleons 2 and 3 form the deuteron then the MSS can be described diagrammatically as shown in Fig. 4.3. The infinite sum shown in Fig. 4.3 can be written as

$$\mathrm{T} = t_{12} + t_{13} + t_{23}\mathcal{G}_0 t_{12} + t_{13}\mathcal{G}_0 t_{12} + t_{12}\mathcal{G}_0 t_{13} + t_{23}\mathcal{G}_0 t_{13} + \ldots \tag{4.6}$$

At this point, Faddeev introduced the idea of replacing the MSS with a set of three coupled integral equations [Fad61].

$$\mathrm{T} = \mathrm{T}_1 + \mathrm{T}_2 + \mathrm{T}_3 \tag{4.7}$$

where

$$\begin{aligned} \mathrm{T}_2 &= t_{13} + t_{13}\mathcal{G}_0(\mathrm{T}_3 + \mathrm{T}_1) \\ \mathrm{T}_3 &= t_{12} + t_{12}\mathcal{G}_0(\mathrm{T}_2 + \mathrm{T}_1) \\ \mathrm{T}_1 &= \quad\; t_{23}\mathcal{G}_0(\mathrm{T}_2 + \mathrm{T}_3) \end{aligned} \tag{4.8}$$

Faddeev proved that this set of equations has a unique solution. Until the 1980's, the numerical complexity of the Faddeev equations made it necessary to use finite-rank

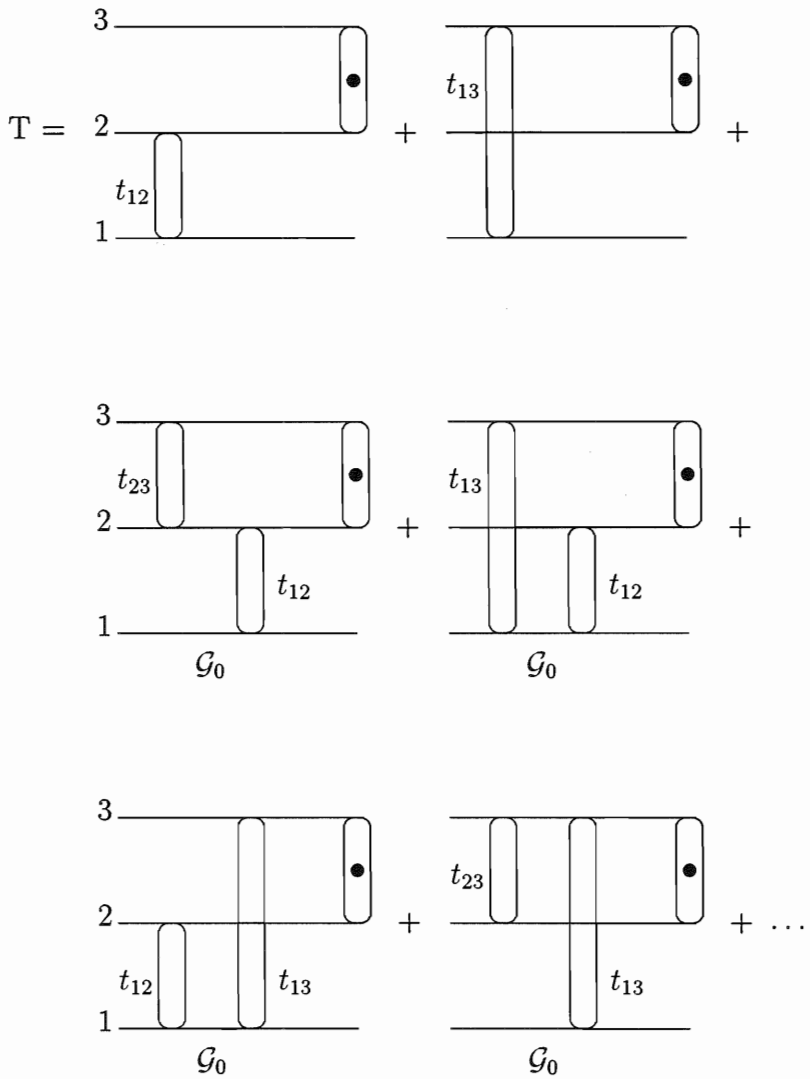

Figure 4.3: Diagram of the multiple scattering series transition operator. Particles 2 and 3 are assumed to form the deuteron (the oval with the black dot on the right side of each term in the series) Note that these diagrams are specifically for the breakup process because the three nucleons in the exit channel are unbound.

representations of the 2N interactions and 2N transition operators. Because of the finite rank of the interactions, these calculations were less than ideal in the effort to determine the size of relativistic effects, three-nucleon force effects and the importance of subnucleonic degrees-of-freedom in the three-nucleon system. However, with the advent of supercomputers, Witała, Glöckle and Cornelius succeeded in solving 3N scattering equations of the Faddeev type for any two-nucleon force (in particular, meson-exchange based potentials) in a numerically precise sense [Wit88a].

4.4 Calculations

The following section describes the method used to solve the Faddeev equations for the breakup process. A more complete description is available in [Wit88a]. Just as in potential scattering, the first step is to introduce transition operators. Using the Alt-Grassberger-Sandhas formalism [Alt67], the elastic scattering transition operator, U, can be written as

$$\mathrm{U} = \mathrm{P}\mathcal{G}_0^{-1} + \mathrm{PT} \tag{4.9}$$

where

$\mathcal{G}_0$ = free particle progagator = $(E + i\epsilon - H_0)^{-1}$,
$E = \frac{3}{4m}q_0^2 + E_d$ ($\hbar = 1$) = total center-of-mass energy, which is fixed by the initial momentum of the neutron relative to the deuteron, $\vec{q}_0$, and the binding energy of the deuteron, E_d,
P = sum of the permutation operators, $\mathrm{P} = \mathrm{P}_{12}\mathrm{P}_{23} + \mathrm{P}_{13}\mathrm{P}_{23}$,
$\mathrm{T} = t\mathrm{P} + t\mathcal{G}_0\mathrm{PT}$,
t is a solution of the Lippmann-Schwinger equation, $t = V + V\mathcal{G}_0 t$.

Once U is known, then the transition operator for the breakup process, U_0, is determined.

$$\mathrm{U}_0 = (1 + \mathrm{P})t\mathcal{G}_0\mathrm{U} \tag{4.10}$$

We then introduce Jacobi momenta and partial wave basis states (see Fig. 4.4). Particles 2 and 3 with relative momentum, p, orbital angular momentum, l, spin, s, and total angular momentum, j, define the two-body subsystem.

$$|\, pq\alpha\rangle = |\, pq(ls)j(\lambda\tfrac{1}{2})\mathrm{IJ}(r\tfrac{1}{2})\mathrm{R}\rangle \tag{4.11}$$

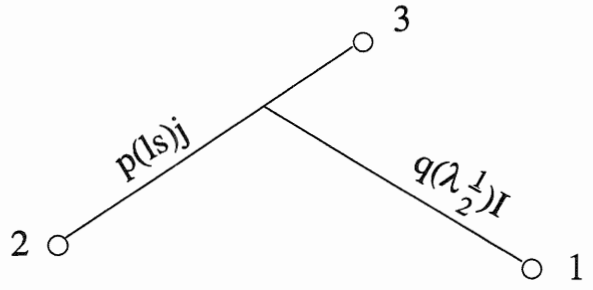

Figure 4.4: Choice of the Jacobi coordinates and the definition of the angular momentum coupling scheme.

Then the transition amplitudes are an infinite system of coupled integral equations.

$$\begin{aligned}\langle pq\alpha \mid \mathrm{T}(E) \mid \phi\rangle = & \quad \langle pq\alpha \mid t\mathrm{P} \mid \phi\rangle \; + \\ & \sum_{\alpha'}\sum_{l_{\bar{\alpha}}} \int_0^\infty dq' q'^2 \int_{-1}^{1} dx \frac{\langle pl_\alpha \mid t^{(\alpha)}(E - \frac{3}{4m}q^2) \mid \pi_1 l_{\bar{\alpha}}\rangle}{\pi_1^{l\bar{\alpha}}} \\ & \times \frac{G_{\bar{\alpha}\alpha'}(q,q',x)}{\pi_2^{l\alpha'}} \frac{\langle \pi_2 q'\alpha' \mid \mathrm{T}(E) \mid \phi\rangle}{E + i0 - q^2 - q'^2 - qq'x}\end{aligned} \tag{4.12}$$

The ket $\mid \phi\rangle = \mid \psi_{m_d}, \vec{q}_0, m_n\rangle$ is the entrance channel for the nd reaction with the neutron and deuteron having spin projections m_n and m_d, respectively. The relative momentum of the neutron to the deuteron is given by $\vec{q}_0$. $G_{\bar{\alpha}\alpha'}(q,q',x)$ is a geometrical factor. The momenta, $\pi_1 = \sqrt{q'^2 + 0.25q^2 + qq'x}$ and $\pi_2 = \sqrt{q^2 + 0.25q'^2 + qq'x}$ are from the matrix elements of the permutation operator, P. The quantum numbers in $\bar{\alpha}$ differ from α only in the orbital angular momentum, l, of the pair. This occurs only when the tensor force is acting.

To calculate the transition amplitudes it is first necessary to truncate the infinite number of channels, α, to a finite one. This is done by assuming that the short-range two-body interaction can be neglected beyond a certain total angular momentum, j_{max}, in the two-body subsystem. The calculations shown in Chapter 5 were done with $j_{max} = 3$. After computing the transition amplitudes, the cross section is calculated as

$$\frac{d^3\sigma}{d\Omega_1 d\Omega_2 dS} = \frac{m}{\hbar^2}\frac{(2\pi)^4}{k_P}\,\rho_1(S,\Omega_1,\Omega_2) \mid \mathrm{M} \mid^2 \tag{4.13}$$

where ρ_1 is the "phase space factor" or "density of final states", $\vec{k}_P$ is the incident neutron momentum in the lab frame ($\hbar = 1$). We can then write the wavefunction

for the incident channel as

$$\mid \phi\rangle = \mid \psi_{deut}\vec{K}sm_s tm_t, \vec{k}_P\sigma\mu_\sigma\tau\mu_{tau}\rangle \tag{4.14}$$

where

ψ_{deut} = the deuteron wavefunction,
$\vec{K}$ = the deuteron momentum,
s = the deuteron spin,
m_s = the deuteron spin projection,
t = the deuteron isospin,
m_t = the deuteron isospin projection,
and similarly for the incident neutron.

This can be simplified by noting that for a deuteron s=1, t=0 and m_t=0 and that for a neutron $\sigma = \frac{1}{2}$, $\tau = \frac{1}{2}$ and $\mu_\tau = -\frac{1}{2}$. Therefore, Eqn. 4.14 becomes

$$\mid \phi\rangle = \mid \psi_{deut}\vec{K}1m_s00, \vec{k}_P\frac{1}{2}\mu_\sigma\frac{1}{2} - \frac{1}{2}\rangle \tag{4.15}$$

Similarly, for the exit channel we can write

$$\mid \phi'\rangle = \mid \vec{k}_1\mu'_{\sigma_1}\mu'_{\tau_1}, \vec{k}_2\mu'_{\sigma_2}\mu'_{\tau_2}, \vec{k}_3\mu'_{\sigma_3}\mu'_{\tau_3}\rangle \tag{4.16}$$

where we have made use of the fact that $\sigma'_i = \tau'_i = \frac{1}{2}$ (and then suppressed these quantum numbers). However it is more appropriate to make use of the Jacobi coordinates which we defined for the exit channel. In that case Eqn. 4.16 becomes:

$$\mid \tilde{\phi'}\rangle = \mid \vec{p}\vec{q}\mu'_{\sigma_1}\mu'_{\sigma_2}\mu'_{\sigma_3}\mu'_{\tau_1}\mu'_{\tau_2}\mu'_{\tau_3}\rangle \tag{4.17}$$

Making use of these wavefunctions, we can then write

$$\mid \mathrm{M} \mid^2 = \frac{1}{6}\sum_{m_s\mu_\sigma}\sum_{\mu'_{\sigma_1}\mu'_{\sigma_2}\mu'_{\sigma_3}} \mid \langle\tilde{\phi'} \mid \mathrm{T} \mid \phi\rangle \mid^2 \tag{4.18}$$

with the summations over the initial and final spin states of the particles. The factor of $\frac{1}{6}$ arises from the spins of the neutron and deuteron in the entrance channel:

$$\frac{1}{6} = \frac{1}{2s+1}\frac{1}{2\sigma+1}$$

The nonrelativistic expression for the available phase space for three particles in the exit channel is given by [Fur72]

$$\delta(E_P + Q - E_1 - E_2 - E_3)\delta(\mathbf{k_P} - \mathbf{k_1} - \mathbf{k_2} - \mathbf{k_3})d\mathbf{k_1}d\mathbf{k_2}d\mathbf{k_3} \tag{4.19}$$

where δ is the delta function, the subscript, P, refers to the projectile, and the numbered subscripts refer to the particles in the exit channel. For a kinematically complete experiment, it is generally of more interest to know the relative probability, ρ_1, of finding E_1 and E_2 along a given element of the kinematically allowed arclength, S. Making use of conservation of momentum and energy, it can be shown that [Mei84a]

$$\rho_1(S, \Omega_1, \Omega_2) =$$

$$\left(\frac{m}{\hbar^2}\right)^2 \frac{k_1^2 k_2^2}{\sqrt{k_1^2(2k_2 - k_P\cos\theta_2 + k_1\cos\theta_{12})^2 + k_2^2(2k_1 - k_P\cos\theta_1 + k_2\cos\theta_{12})^2}} \tag{4.20}$$

where

$\vec{k}_P$ = incident neutron momentum in the lab frame,
$\vec{k}_i$ = momentum of neutron i in the lab,
$\cos\theta_i = \hat{k}_i \cdot \hat{k}_P$,
$\cos\theta_{ij} = \hat{k}_i \cdot \hat{k}_j$.

Using Eqn.4.13 and Eqn.4.20, the transition amplitudes calculated by Dr. Henryk Witała were converted to cross sections for comparison to the results of this experiment.

Chapter 5

Results and Conclusions

As described in Section 2.3, cross-section measurements of three of the four configurations were duplicated on each side of the beam axis. This reduced the amount of accelerator time necessary to make these measurements and also gave a measure of the systematic errors in our experimental techniques. Figures 5.1 to 5.3 show the cross sections for each pair of neutron detectors in coincidence. The dashed curves are the point scattering Bonn-B calculations and the solid curves are Bonn-B calculations smeared over the finite geometry of our experimental setup. The error bars shown are statistical only. Not shown is the scale uncertainty of the measurement. The scale uncertainty results from the systematic error in the normalization derived from the nd elastic scattering and from the uncertainty in the absolute neutron detector efficiency. The scale uncertainty was $\pm 4.6\%$ (see Sec. 3.3.4) and can only affect the magnitude of the cross section, not the shape.

In order to compare the results for the two space-star measurements, the statistical average of the cross section for each detector pair was computed for the five data points centered on the space-star point. The five point average for the R1-L3 detector pair measurement was $1.254 \pm .054$ mb/sr^{2}MeV and the average for the R3-L1 measurement was $1.365 \pm .056$ mb/sr^{2}MeV. Though the difference in the average for the two detector pairs was found to differ from zero by 1.43 standard deviations, the two measurements differed by only 0.111 mb/sr^{2}MeV which is well within the systematic uncertainty of the measurements. The points at the extremes were excluded because they are highly sensitive to the efficiency values at low neutron energies, which makes them extremely sensitive to the pulse-height threshold set on each detector. The

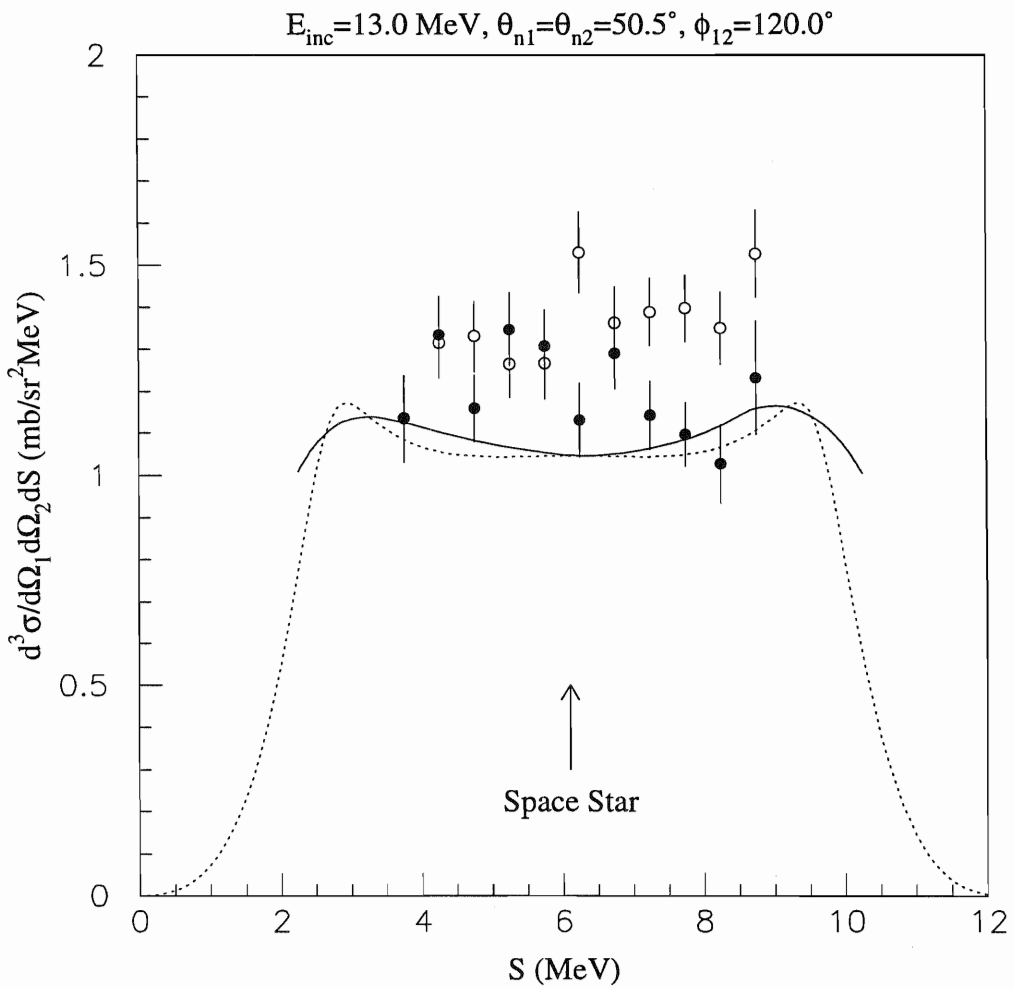

Figure 5.1: Comparison of results for SST for two pairs of neutron detectors in coincidence. Solid circles: R1–L3, open circles: R3–L1. The detectors are as described in Section 2.3.

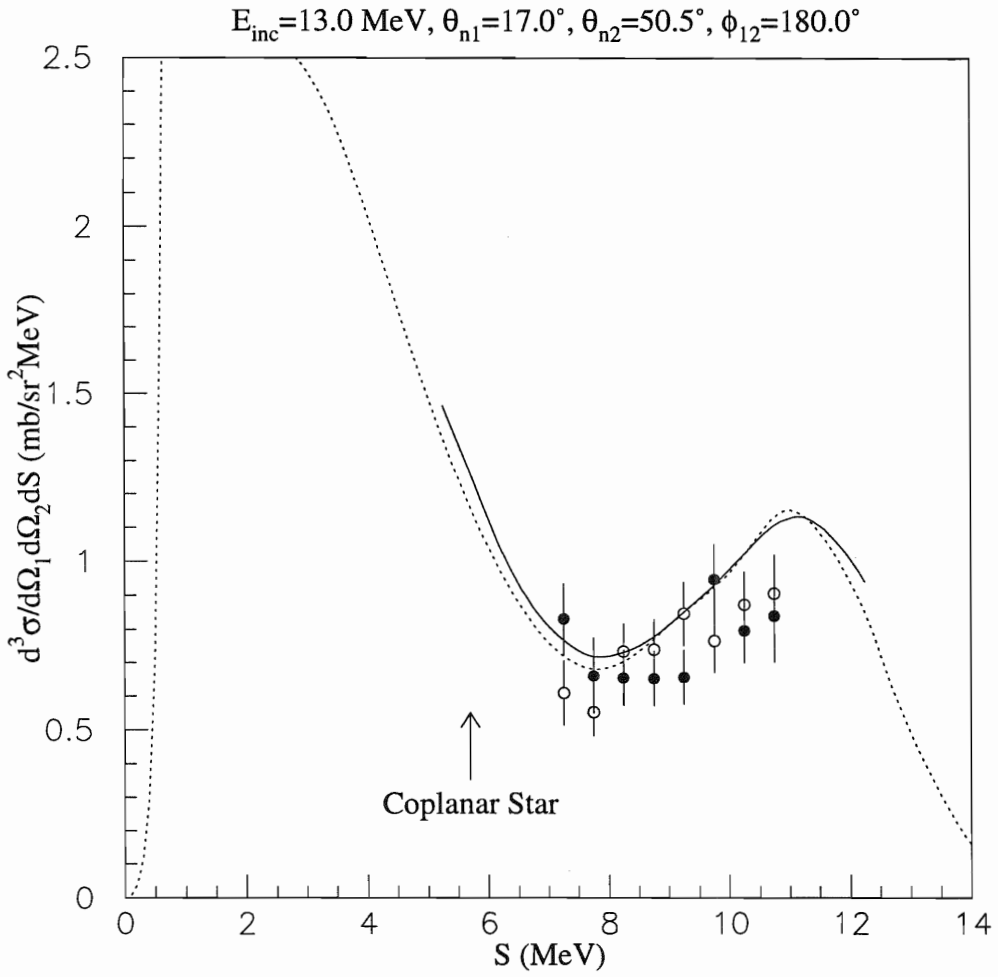

Figure 5.2: Comparison of results for CST for two pairs of neutron detectors in coincidence. Solid circles: R2–L3, open circles: R3–L2. The detectors are as described in Section 2.3.

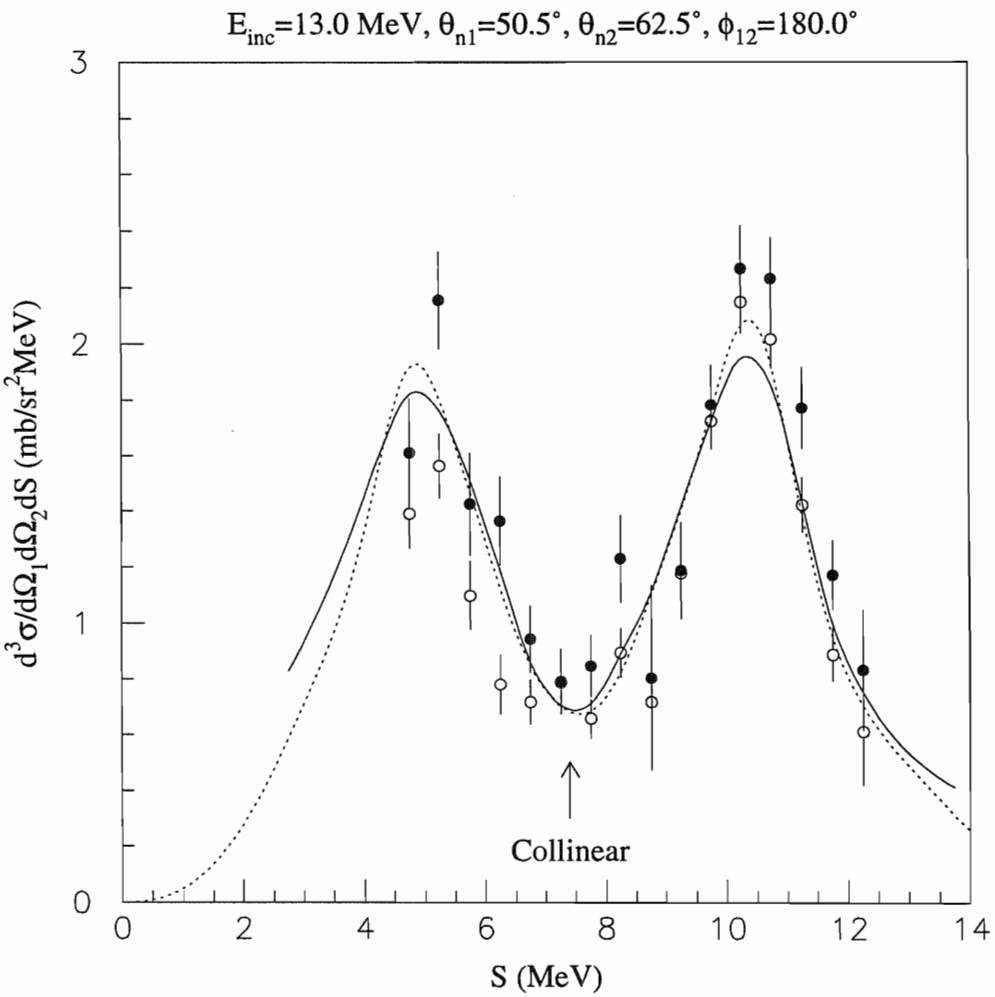

Figure 5.3: Comparison of results for COLLa for two pairs of neutron detectors in coincidence. Solid circles: R3–L4, open circles: R4–L3. The detectors are as described in Section 2.3.

same method was used to compare the coplanar-star results. All the data points were used because the data points corresponding to low neutron energies had already been excluded for other reasons. In this case the difference between the two pairs of detectors was statistically equivalent to zero ($\Delta\sigma = 0.0078 \pm 0.0591$ mb/sr^{2}MeV). For the collinear configuration which was mirrored about the beam axis (COLLa), the shape of the cross section as a function of the arc length along the locus made it necessary to only consider three points centered on the collinear point. In this case the cross section for the two detector pairs differed from zero by 1.6 standard deviations ($\Delta\sigma = 0.143 \pm 0.0869$ mb/sr^{2}MeV). Again the duplicate measurements agree to within the systematic uncertainty in the experimental technique.

The results of the cross-section measurements described in this work are shown in Figs. 5.5 to 5.7. The previous nd data shown in the figures are from [Str89] and the pd data are from [Rau91]. The solid circles in each figure are the results of the experiment described in this work. The dashed curve in each figure is a rigorous point geometry nd calculation using the Bonn-B OBEPQ to describe the underlying two-nucleon subsystem. The solid curve in each figure is also a rigorous nd calculation but smeared over the finite geometry of our experiment. The Bonn-B OBEPQ was also used for these calculations to represent the 2N interactions. As indicated by the two calculations, the size of finite geometry effects is neglible at the point of interest along the locus for both of the collinear configurations and for the space star configuration. For the coplanar-star configuration the finite geometry effects cause a slight increase in the cross section at the coplanar star point.

For COLLa we found very good agreement with the calculation at the collinear point. For the three points about the collinear point, the difference between the data and calculation were not statistically different from zero. However comparison to the previous nd results found the results of [Str89] to be 2.4 standard deviations higher than our results in the region of the collinear point when both statistical and systematic uncertainties were considered.

For COLLb we found differences between our data and both the calculation and the previous measurement. For the five data points centered on the collinear point, our data were 3.3 standard deviations lower than the calculation and 4.1 standard deviations below the data of [Str89]. Most significantly, the shape of our data agrees with the Bonn-B prediction in that we found no enhancement in the cross section

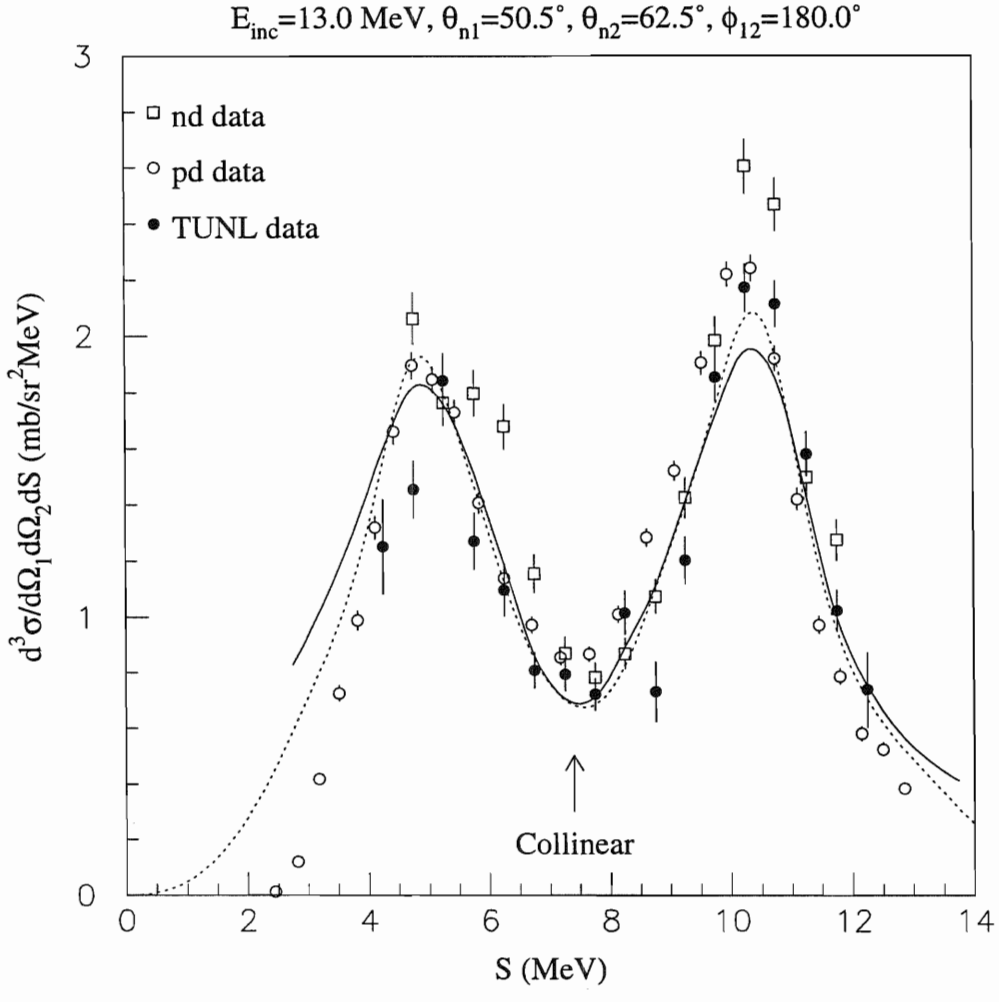

Figure 5.4: Results for COLLa. Dashed curve is point scattering calculation. Solid curve is finite geometry calculation. Previous nd data are from [Str89]. Previous pd data are from [Rau91].

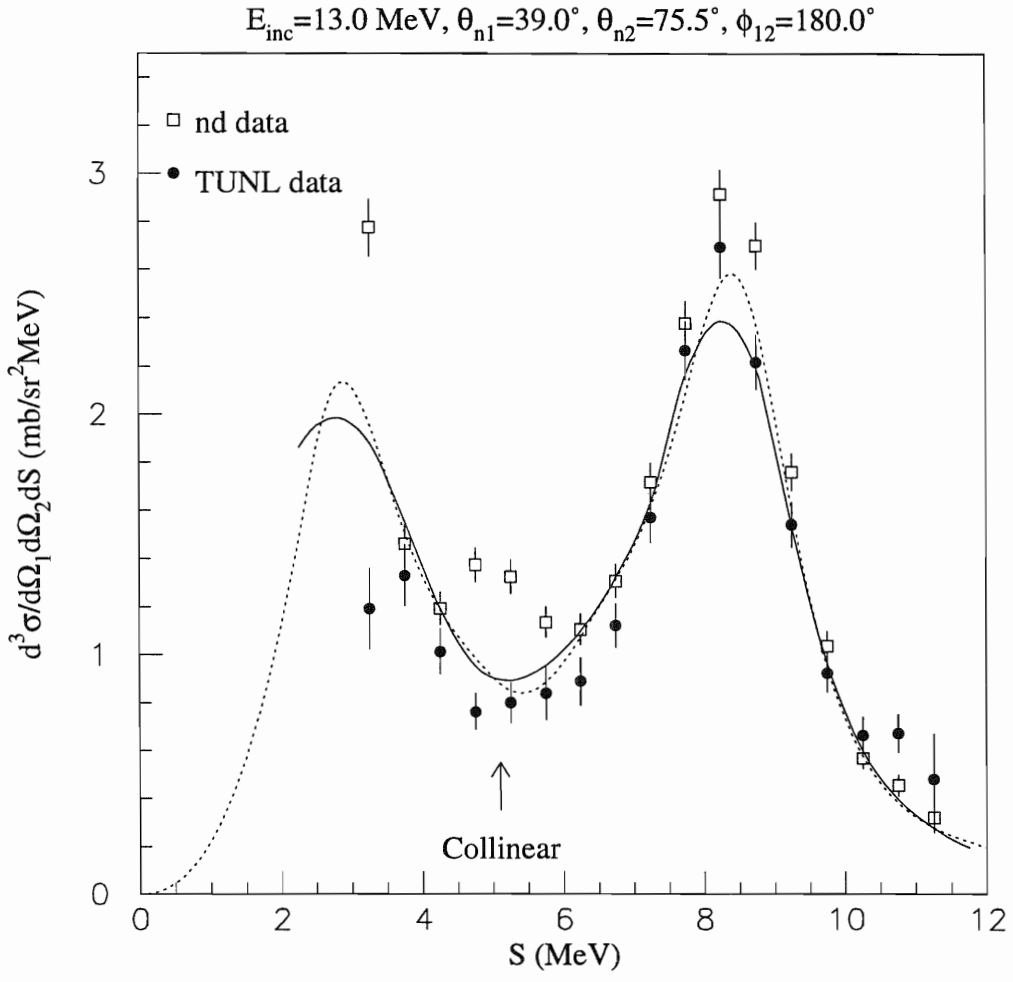

Figure 5.5: Results for COLLb. Dashed curve is point scattering calculation. Solid curve is finite geometry calculation. Previous nd data are from [Str89].

at the collinear point as indicated by the previous results of [Str89]. In addition we found good agreement between the nd and pd data for the collinear configuration (COLLa). This finding indicates that Coulomb effects are small for this configuration. In the region where the cross section is most strongly peaked, our data are higher than the finite geometry calculations. The peaks in the cross section on either side of the collinear point are due to neutron-proton final-state interactions (FSI). In a FSI two of the particles in the exit channel have a very low relative momentum (almost identical momenta) causing the particles in the pair to interact strongly and consequently producing an enhancement in the breakup cross section. In neither case, COLLa or COLLb, were the kinematic requirements met to observe the full cross-section enhancement from the FSI.

The minimum obtainable proton energy defined the portion of the kinematic locus for the coplanar star configuration we were able to measure. At the coplanar-star point the proton energy is less than 0.5 MeV (see Table C.2). To reduce the accidental event rate and the electronic dead-time it was necessary to raise the lower-level threshold on the discriminator for the center detector above the minimum level needed to obtain the coplanar star point. Though the threshold on the discriminator for the center detector was set at about 0.4 MeV protons, counts were lost at the coplanar-star point due to the finite energy resolution of the detector. Our results for this configuration were 1.0 standard deviation below the calculation, but were 6.0 standard deviations below the data of [Str89].

While our results for the coplanar-star and both collinear configurations appear to be consistently lower than the calculation, there still remains the 5% scale uncertainty. This scale uncertainty cannot affect the shape of the cross section as a function of arc length, but could affect the magnitude of the cross section. The data of [Str89] also includes a 5% scale uncertainty. However, for the previous data the shape of the cross sections for the coplanar star and one of the collinear configurations (COLLb) are not the same as the calculation. For these three configurations, we find no evidence to support the need for addition of a 3NF to the potential used to make the calculations.

In the space-star configuration our data was not statistically different from zero when compared with the previous measurement [Str89]. However, when compared to the calculations, our data were 9.5 standard deviations higher than the Bonn-B prediction. These results confirm that the nd data for the space-star configuration are

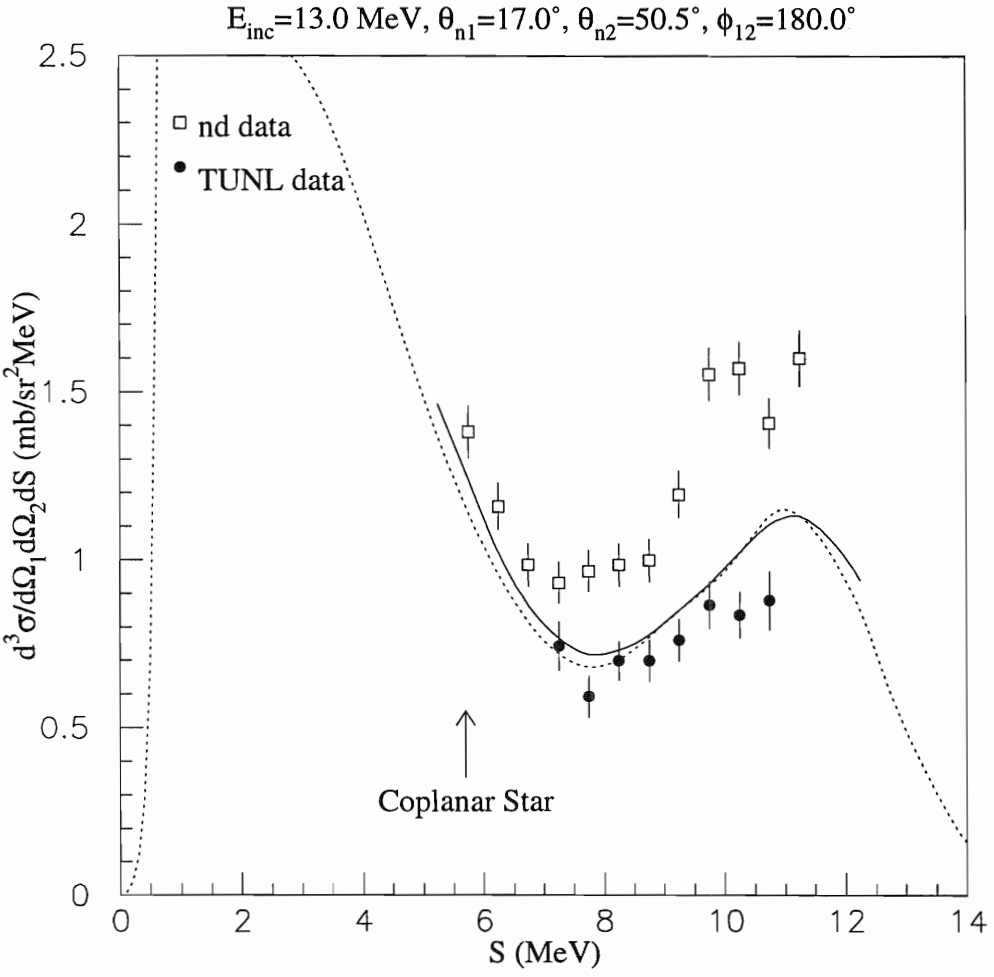

Figure 5.6: Results for CST. Dashed curve is point scattering calculation. Solid curve is finite geometry calculation. Previous nd data are from [Str89].

$\sim$20% higher than the calculations. While these findings would seem to indicate some effect due to a 3NF, a recent computational study [Hüb93] found a different effect. In that study comparisons were made between rigorous nd continuum calculations which used realistic 2N forces with and without the inclusion of a simple 2π-exchange 3NF [Coo79]. They found that the simple 3NF *reduced* the cross section for the space-star configuration. The results of this first model study for 3NF effects and the present data seem to indicate a definite need for more theoretical study of the space star cross section. Because the experimentally determined cross section at 10.3 MeV agrees with calculations, it is necessary to understand why the energy dependence of the cross section calculated with only 2N forces differs from that of the experimentally determined cross section.

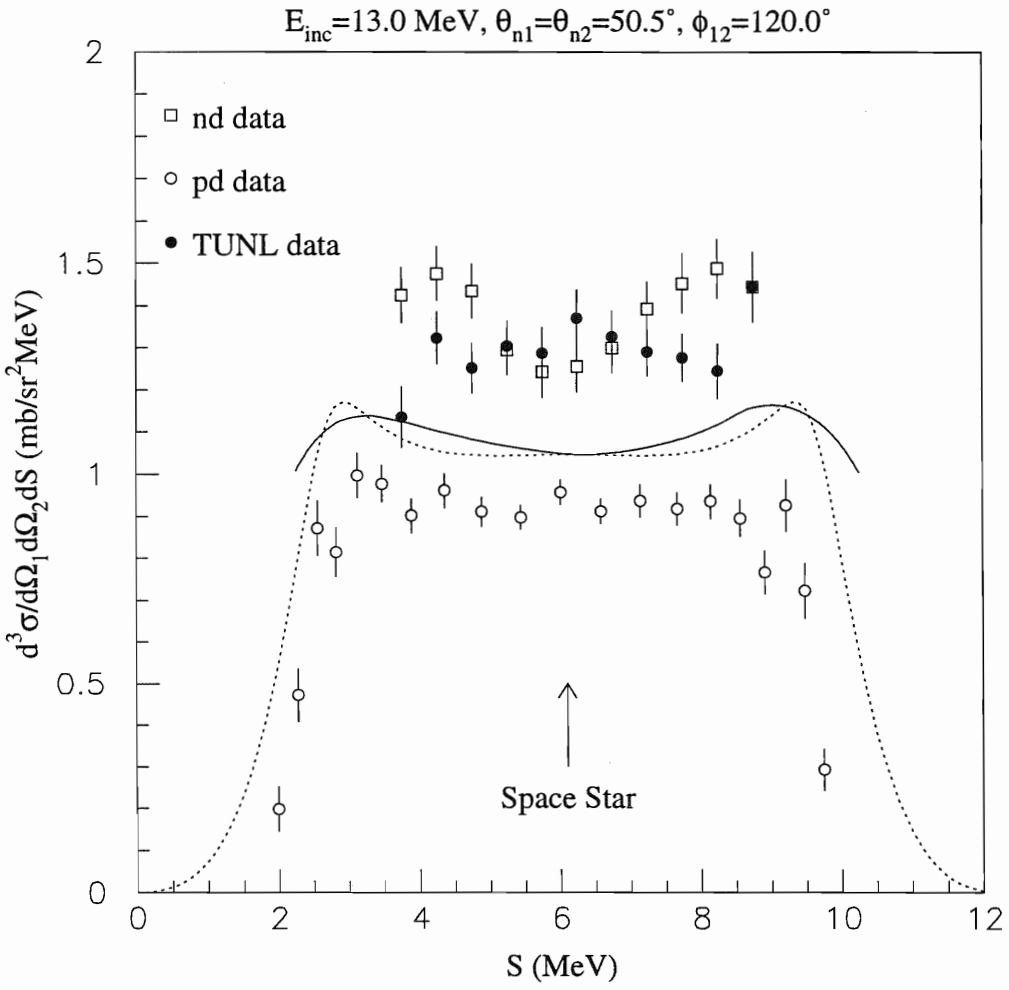

Figure 5.7: Results for SST. Dashed curve is point scattering calculation. Solid curve is finite geometry calculation. Previous nd data are from [Str89]. Previous pd data are from [Rau91].

A

Neutron Detection Efficiency Measurements

Prior to making the cross-section measurements of the n+d→n+n+p reaction, it was necessary to determine the absolute neutron detection efficiency of each of the eleven liquid, organic scintillators. Neutrons do not cause any direct ionization of matter, therefore neutron detection in organic scintillators is based on the measurement of ionization caused by secondary charged particles from neutron scattering and neutron-induced nuclear reactions. Consequently the efficiency varies with the incident neutron energy. Because it is possible for the neutron to react in the detector but not deposit its full energy within the volume of the detector, the efficiency depends on the threshold level set on the pulse height [Dro72].

The neutron energy range relevant to the breakup reaction was 0.4-10 MeV. In order to cover this entire energy range with one measurement technique, we used the neutrons emitted from the spontaneous fission of ^{252}Cf. The detection of the fission fragments made it possible to use time-of-flight (TOF) techniques to determine the energy of the detected neutrons [Böt90a]. The energy distribution of the neutrons emitted from ^{252}Cf has been thoroughly investigated [Böt83, Poe83, Bol87, Böt90b] and the shape of the spectrum is well known and can be taken as a standard [Frö87, Man87].

The ^{252}Cf source was housed in a cylindrical gas scintillator. The walls of the scintillator were 0.79 mm thick brass. The scintillator was 7.30 cm long × 5 cm

in diameter followed by a 2.54 cm radius dome. By positioning the ^{252}Cf source at the center of the dome, the correction for neutron attenuation in the scintillator housing was identical for all detector angles. The scintillator was filled to 254 Torr with Argon and was viewed by a fast 5 cm diameter photomultiplier tube (PMT). The source was a 2-μg deposit of ^{252}Cf at the center of a 12.7 mm diameter by 0.127 mm thick platinum foil. The active area of the source was 5 mm in diameter. A 50 mg/cm^2 layer of gold was electroplated onto the ^{252}Cf to prevent the loss of ^{252}Cf by recoil. The center of the ^{252}Cf was positioned at the center of curvature of the dome of the gas scintillator with the deposit facing the PMT.

Two measurements were performed with this source and scintillator. The first measurement involved an array of all eleven scintillators used for the breakup measurement. The detectors were positioned around the gas scintillator in an arc of radius 3 m. The total angular spread of the was well below 180° to minimize effects due to the non-uniformity of the surface of the platinum foil. As a compromise between limiting the total angular span of the array and minimizing cross-talk between the detectors, they were placed 13° apart. The source and the neutron detectors were supported on wooden scaffolds approximately 3 m above the floor. This placed the detectors midway between the floor and the ceiling.

Background measurements were made by placing a shadowbar midway between the source and a detector. The shadowbars were designed to reduce the flux of 10 MeV neutrons by a factor of 6000. The shadowbars were conical in shape and consisted of a 50.8 cm long copper section followed by a 45.7 cm long polyethylene section. To allow simultaneous foreground and background measurements, only three shadowbars were in place at any time. The shadowbars were positioned on detectors 52° apart.

Just as in the breakup measurements, the signals from two detectors were fanned into each set of detector electronics. For each coincidence between events in the gas scintillator and any neutron detector, 20 parameters were stored in the computer: the pulse height in the fission detector (1), TOF for each pair of detectors (6), the pulse height for each pair of detectors (6), pulse shape for each pair of detectors (6) and a hit register (1) to provide routing information. The data were stored in event-mode to allow a more complete analysis off-line.

The off-line analysis of these data showed problems with the electronics of four of the eleven detectors. New measurements were made for those four detectors and for

two others to allow comparison to the previous measurements. For this experiment only two detectors were measured simultaneously and each detector had completely independent electronics (see Fig. A.1). Due to non-isotropic detection of the fission fragments in the gas scintillator only relative efficiencies could be obtained from these measurements. All detectors of the same type (see Sec. 2.3) were found to have the same detection efficiency. Fig. A.2 shows the relative efficiencies for four detectors in comparison to a Monte-Carlo simulation [Die82]. The Monte-Carlo code was obtained from the Physikalisch-Technische Bundesanstalt (PTB) and was one which had previously exhibited good results for other experiments [Cub89].

To determine the absolute detection efficiency the ^{2}H(d,n)^{3}He reaction was used. The efficiencies of three of the eleven neutron detectors were measured using a deuterium gas cell filled to one atmosphere absolute. The gas cell pressure was measured with a precision pressure gauge in order to accurately determine the number of target nuclei available for the ^{2}H(d,n)^{3}He reaction. The total BCI was counted to determine the number of deuterons incident on the gas cell. Two detectors were measured at the same time in order to compare the results with the previous relative efficiency measurement. One detector was placed at 0° and the other was placed at 60°. This also allowed a larger energy range to be covered than if the measurement was made only at 0°. The flightpath for each detector was approximately 475 cm.

The number of target nuclei in the gas cell was calculated by

$$N_t = \frac{P \cdot length \cdot density}{R \cdot T} \tag{A.1}$$

where

P = the pressure in the gas cell,
$length$ = the length of the gas cell,
$density$ = the density of the gas in the cell,
R = the gas constant,
T = the temperature of the gas cell.

The total BCI was converted to the number of deuterons incident on the target, I. The attenuation of the neutrons was calculated using the neutron total cross sections for the materials between the gas cell and the detectors and was compared to similar

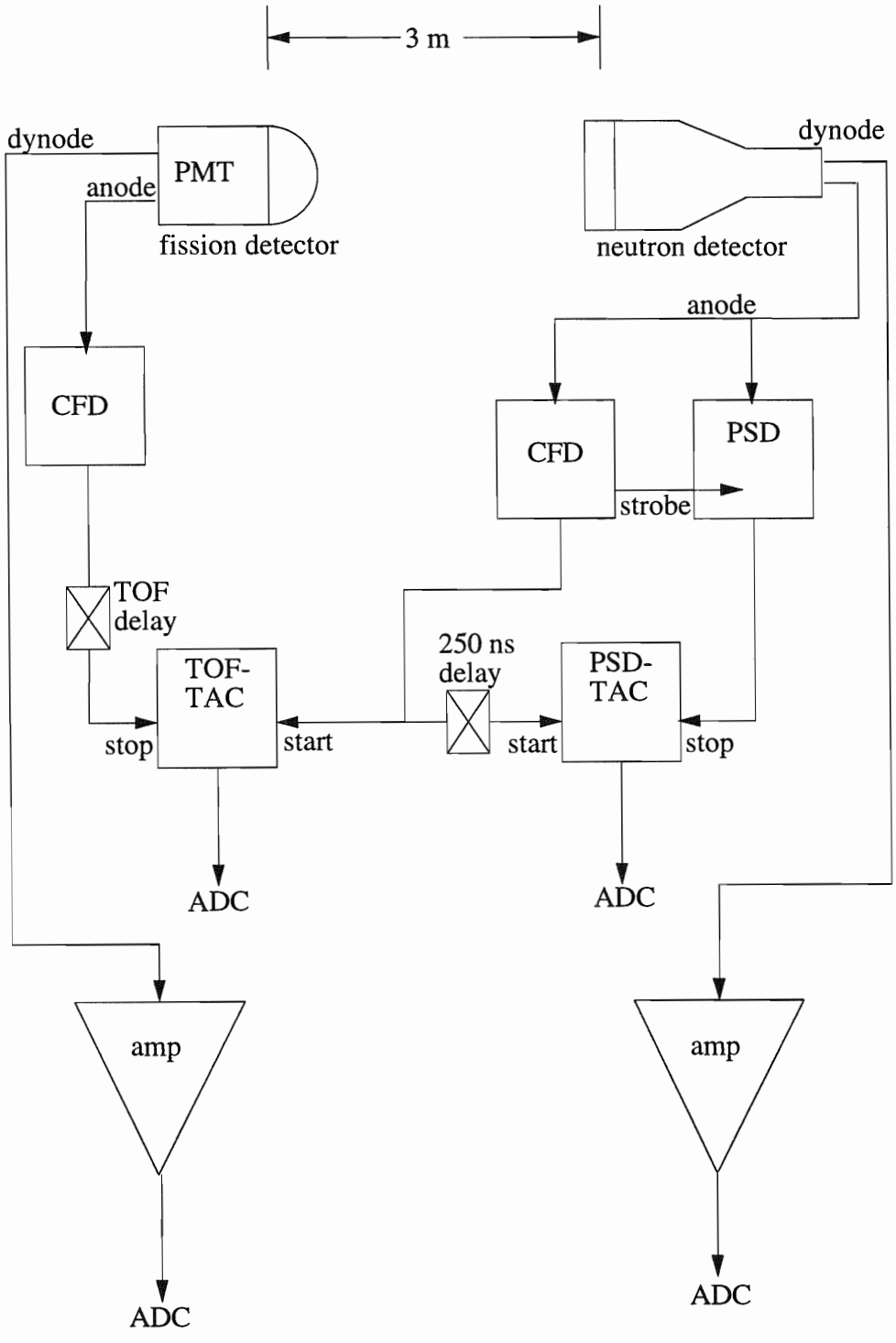

Figure A.1: Electronics setup for efficiency measurements with the ^{252}Cf source.

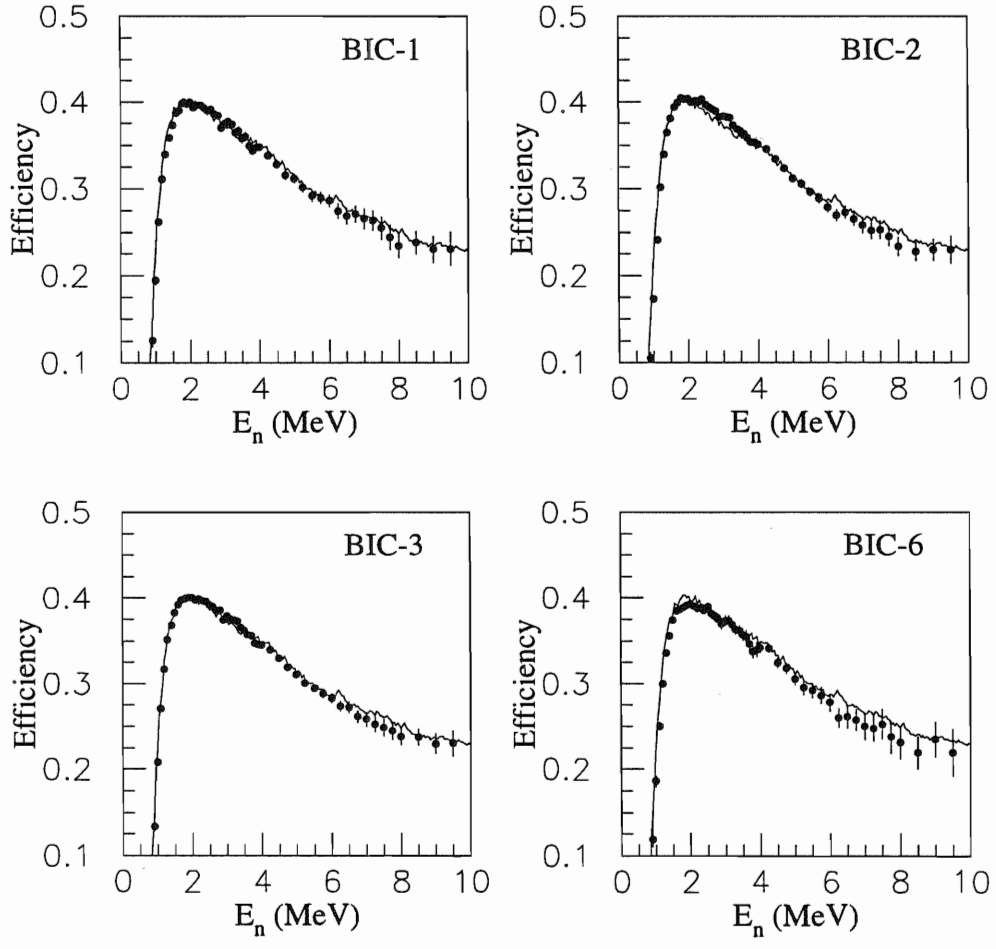

Figure A.2: The relative neutron detection efficiencies as a function of energy for four detectors. The solid curve is the prediction of the Monte Carlo simulation. The data are normalized to the simulation. All detectors use the same normalization factor.

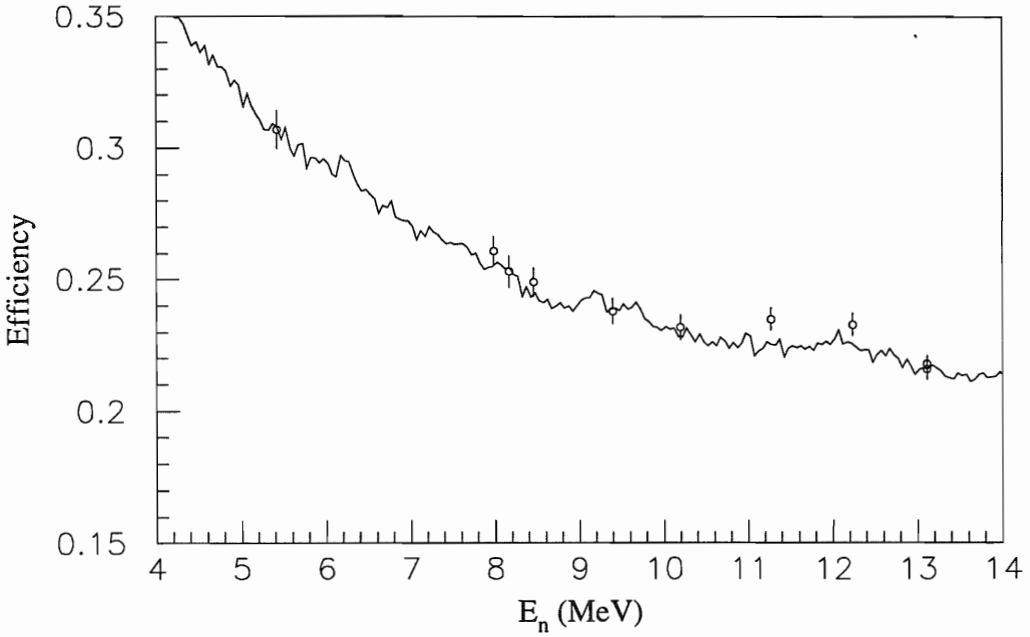

Figure A.3: Absolute neutron detection efficiencies from ^{2}H(d,n)^{3}He measurements at TUNL in comparison to prediction from PTB Monte Carlo.

calculations from [Ped86]. The cross section for the ^{2}H(d,n)^{3}He reaction was obtained from [Dro78]. The efficiency was then calculated from the experimental yields.

$$\epsilon = \frac{Y}{\frac{d\sigma}{d\Omega}(\theta) \cdot \alpha \cdot d\Omega \cdot N_t \cdot I} \tag{A.2}$$

To verify our results, two detectors were sent to Braunschweig, Germany where the PTB group made similar measurements using a cyclotron and the ^{2}H(d,n)^{3}He reaction. Their method differed in that the recoil pulse-height spectrum for each neutron energy was fit to produce a light response function for each detector. The yields for each spectrum were used to normalize the Monte-Carlo calculated efficiency. Figure A.3 shows the results of the TUNL ^{2}H(d,n)^{3}He measurements in comparison to a Monte-Carlo simulation using the light response function determined by the results of the PTB group. The results of these independent measurements agreed to within statistics. These efficiencies were then used to correct the nd breakup cross sections.

B

Cross Section Tabulation

Tabulated results of the measurements described in this work.

	SST		CST		COLLa		COLLb	
S	σ	$\Delta\sigma$	σ	$\Delta\sigma$	σ	$\Delta\sigma$	σ	$\Delta\sigma$
3.25	–	–	–	–	–	–	1.1906	0.16891
3.75	1.1349	0.07266	–	–	–	–	1.3295	0.12807
4.25	1.3235	0.06241	–	–	1.2516	0.16843	1.0120	0.09541
4.75	1.2513	0.05844	–	–	1.4541	0.10152	0.7618	0.07638
5.25	1.3041	0.05905	–	–	1.8423	0.09741	0.7983	0.08338
5.75	1.2871	0.06105	–	–	1.2708	0.10126	0.8380	0.11128
6.25	1.3701	0.06740	–	–	1.0961	0.09416	0.8868	0.09942
6.75	1.3259	0.06072	–	–	0.8082	0.06619	1.1191	0.09171
7.25	1.2895	0.05845	0.7423	0.07348	0.7933	0.06042	1.5686	0.10379
7.75	1.2757	0.05642	0.5922	0.06179	0.7214	0.05868	2.2623	0.12003
8.25	1.2435	0.06495	0.6981	0.05891	1.0146	0.07871	2.6922	0.12939
8.75	1.4440	0.08352	0.6980	0.06108	0.7299	0.10862	2.2131	0.11362
9.25	–	–	0.7596	0.06249	1.2031	0.08547	1.5377	0.09413
9.75	–	–	0.8647	0.07109	1.8537	0.08359	0.9216	0.08056
10.25	–	–	0.8341	0.06764	2.1722	0.08571	0.6626	0.07712
10.75	–	–	0.8776	0.08790	2.1142	0.08198	0.6699	0.08076
11.25	–	–	–	–	1.5807	0.07944	0.4760	0.19191
11.75	–	–	–	–	1.0196	0.07560	–	–
12.25	–	–	–	–	0.7365	0.13523	–	–

Table B.1: Cross Section for nd breakup reaction. Cross section and error given in $\frac{\text{mb}}{\text{sr}^2\cdot\text{MeV}}$, arc-length in MeV. Tabulated error is statistical only.

C

Kinematic Tabulations

Some kinematic values of interest for the configurations studied in this work are given in Tabs. C.1 to C.4. The kinematically allowed locus is determined by the neutron detector angles and the incident neutron energy of 13.0 MeV. The neutron detector angles for each configuration are given in the captions. The values in the tables are defined as:

E_{n1} = lab energy of neutron one
E_{n2} = lab energy of neutron two
E_p = lab energy of the proton
E_{12} = relative energy of neutron one and neutron two
E_{13} = relative energy of neutron one and the proton
E_{23} = relative energy of neutron two and the proton
S = arc length along the kinematic locus
θ_p and ϕ_p = lab angles of the proton

Each of the configurations under study contains one point on the locus which was of special interest kinematically:

Space star point: S = 6.1 MeV
Coplanar star point: S = 5.7 MeV
Collinear point (COLLa): S = 7.4 MeV
Collinear point (COLLb): S = 5.1 MeV

Space Star Kinematics								
Laboratory Energy			Relative Energy			Arc	Proton Lab Angle	
E_{n2}	E_{n1}	E_p	E_{12}	E_{23}	E_{13}	S	θ_p	ϕ_p
1.00	5.13	4.64	2.82	1.77	5.07	3.1	45	-26
1.20	5.12	4.45	2.90	1.78	4.99	3.3	46	-29
1.40	5.09	4.29	2.96	1.82	4.89	3.5	47	-32
1.60	5.02	4.15	3.01	1.88	4.77	3.7	48	-34
1.80	4.94	4.03	3.05	1.96	4.65	3.9	48	-37
2.00	4.84	3.93	3.09	2.06	4.52	4.1	49	-39
2.20	4.73	3.85	3.12	2.17	4.38	4.3	49	-42
2.40	4.60	3.77	3.15	2.29	4.23	4.6	50	-44
2.60	4.47	3.71	3.17	2.42	4.07	4.8	50	-47
2.80	4.32	3.66	3.19	2.56	3.91	5.1	50	-49
3.00	4.16	3.62	3.20	2.71	3.75	5.3	51	-52
3.20	3.98	3.59	3.21	2.88	3.58	5.6	51	-55
3.40	3.80	3.57	3.22	3.04	3.40	5.9	51	-57
3.60	3.61	3.57	3.22	3.22	3.22	6.1	51	-60
3.80	3.40	3.57	3.22	3.40	3.04	6.4	51	-63
4.00	3.18	3.59	3.21	3.59	2.86	6.7	51	-66
4.20	2.95	3.63	3.20	3.79	2.67	7.0	51	-69
4.40	2.69	3.69	3.18	4.00	2.48	7.4	50	-72
4.60	2.41	3.77	3.15	4.22	2.29	7.7	50	-76
4.80	2.08	3.90	3.10	4.46	2.10	8.1	49	-80
5.00	1.66	4.11	3.02	4.74	1.90	8.5	48	-85
5.00	0.59	5.19	2.61	5.15	1.90	9.6	42	-80

Table C.1: Kinematics for SST with θ_{n1}=50.5°, ϕ_{n1}=0.0°, θ_{n2}=50.5°, ϕ_{n2}=120.0°. Arc length and energies given in MeV, angles given in degrees.

Coplanar Star Kinematics							
Laboratory Energy			Relative Energy			Arc	Lab Angle
E_{n2}	E_{n1}	E_p	E_{12}	E_{23}	E_{13}	S	θ_p
3.40	6.94	0.43	3.31	2.95	3.40	5.3	82
3.50	6.81	0.47	3.29	3.06	3.31	5.5	83
3.60	6.67	0.51	3.26	3.18	3.22	5.7	84
3.70	6.53	0.55	3.23	3.29	3.13	5.8	85
3.80	6.39	0.59	3.21	3.41	3.04	6.0	86
3.90	6.24	0.63	3.18	3.53	2.95	6.2	87
4.00	6.10	0.68	3.16	3.64	2.86	6.3	88
4.10	5.95	0.72	3.14	3.76	2.77	6.5	89
4.20	5.81	0.77	3.11	3.87	2.67	6.7	90
4.30	5.66	0.82	3.09	3.99	2.58	6.9	89
4.40	5.50	0.87	3.07	4.11	2.48	7.1	88
4.50	5.35	0.93	3.05	4.22	2.39	7.2	87
4.60	5.19	0.98	3.03	4.34	2.29	7.4	86
4.70	5.03	1.04	3.01	4.46	2.19	7.6	85
4.80	4.87	1.10	2.98	4.58	2.10	7.8	84
4.90	4.71	1.17	2.96	4.70	2.00	8.0	83
5.00	4.54	1.24	2.95	4.81	1.90	8.2	82
5.10	4.36	1.31	2.93	4.93	1.80	8.4	81
5.20	4.19	1.39	2.91	5.05	1.70	8.6	80
5.30	4.00	1.47	2.89	5.17	1.60	8.8	79
5.40	3.81	1.56	2.87	5.29	1.50	9.0	78
5.50	3.61	1.66	2.85	5.41	1.40	9.3	77
5.60	3.41	1.77	2.83	5.53	1.30	9.5	75
5.70	3.18	1.89	2.81	5.65	1.20	9.7	74
5.80	2.95	2.03	2.79	5.77	1.10	10.0	72
5.90	2.68	2.20	2.77	5.90	0.99	10.3	70
6.00	2.37	2.41	2.74	6.03	0.89	10.6	68
6.10	1.90	2.77	2.70	6.18	0.79	11.1	65
6.00	0.95	3.83	2.56	6.21	0.89	12.0	55

Table C.2: Kinematics for CST with θ_{n1}=17.0°, ϕ_{n1}=0.0°, θ_{n2}=50.5°, ϕ_{n2}=180.0°. Arc length and energies given in MeV, angles given in degrees.

Collinear Kinematics							
Laboratory Energy			Relative Energy			Arc	Lab Angle
E_{n2}	E_{n1}	E_p	E_{12}	E_{23}	E_{13}	S	θ_p
1.00	6.27	3.50	4.61	0.61	4.44	4.0	34
1.20	6.39	3.19	4.88	0.49	4.30	4.2	33
1.40	6.46	2.92	5.11	0.41	4.14	4.4	32
1.60	6.50	2.68	5.31	0.37	3.98	4.7	31
1.80	6.51	2.47	5.49	0.36	3.81	4.9	30
2.00	6.49	2.28	5.65	0.38	3.63	5.1	28
2.20	6.45	2.12	5.80	0.42	3.44	5.3	26
2.40	6.40	1.98	5.93	0.48	3.25	5.5	24
2.60	6.32	1.85	6.05	0.56	3.06	5.7	22
2.80	6.23	1.75	6.14	0.65	2.86	5.9	20
3.00	6.12	1.66	6.23	0.77	2.66	6.1	17
3.20	5.99	1.59	6.30	0.90	2.45	6.4	14
3.40	5.84	1.54	6.36	1.05	2.24	6.6	11
3.60	5.68	1.50	6.40	1.22	2.03	6.9	7
3.80	5.49	1.48	6.43	1.41	1.82	7.1	4
4.00	5.29	1.49	6.44	1.62	1.60	7.4	0
4.20	5.06	1.52	6.43	1.85	1.38	7.7	4
4.40	4.80	1.58	6.39	2.10	1.16	8.1	8
4.60	4.50	1.67	6.33	2.39	0.94	8.4	12
4.80	4.15	1.83	6.22	2.72	0.72	8.8	16
5.00	3.71	2.07	6.04	3.13	0.50	9.3	20
5.20	2.98	2.60	5.63	3.76	0.27	10.1	25
5.00	1.55	4.23	4.36	4.80	0.50	11.5	30
4.80	1.24	4.73	3.97	4.97	0.72	11.9	30
4.60	1.02	5.15	3.66	5.06	0.94	12.2	30
4.40	0.86	5.52	3.38	5.11	1.16	12.4	29
4.20	0.72	5.86	3.14	5.14	1.38	12.7	29
4.00	0.61	6.17	2.91	5.15	1.60	12.9	28
3.80	0.51	6.47	2.70	5.14	1.82	13.1	28

Table C.3: Kinematics for COLLa with θ_{n1}=50.5°, ϕ_{n1}=0.0°, θ_{n2}=62.5°, ϕ_{n2}=180.0°. Arc length and energies given in MeV, angles given in degrees.

Collinear Kinematics							
Laboratory Energy			Relative Energy			Arc	Lab Angle
E_{n2}	E_{n1}	E_p	E_{12}	E_{23}	E_{13}	S	θ_p
1.00	7.74	2.04	5.52	0.46	3.67	2.8	33
1.20	7.73	1.85	5.73	0.47	3.46	3.0	30
1.40	7.68	1.70	5.90	0.52	3.24	3.2	27
1.60	7.60	1.58	6.05	0.60	3.01	3.4	24
1.80	7.49	1.49	6.17	0.71	2.78	3.6	20
2.00	7.35	1.42	6.26	0.85	2.55	3.9	16
2.20	7.19	1.39	6.34	1.01	2.31	4.1	12
2.40	7.00	1.38	6.40	1.19	2.07	4.4	8
2.60	6.78	1.40	6.43	1.40	1.83	4.7	4
2.80	6.53	1.44	6.44	1.64	1.58	5.0	1
3.00	6.26	1.52	6.42	1.90	1.34	5.4	5
3.20	5.94	1.64	6.38	2.20	1.09	5.7	9
3.40	5.57	1.81	6.29	2.54	0.84	6.2	13
3.60	5.12	2.06	6.14	2.93	0.58	6.6	17
3.80	4.53	2.44	5.89	3.44	0.33	7.3	21
3.80	2.20	4.77	4.20	5.13	0.33	9.6	26
3.60	1.76	5.41	3.73	5.35	0.58	10.1	26
3.40	1.46	5.91	3.36	5.47	0.84	10.5	25
3.20	1.23	6.34	3.04	5.53	1.09	10.8	24
3.00	1.04	6.73	2.76	5.57	1.34	11.0	23
2.80	0.89	7.09	2.50	5.58	1.58	11.3	23
2.60	0.76	7.42	2.26	5.57	1.83	11.5	22
2.40	0.64	7.73	2.04	5.55	2.07	11.8	21

Table C.4: Kinematics for COLLb with θ_{n1}=39.0°, ϕ_{n1}=0.0°, θ_{n2}=75.5°, ϕ_{n2}=180.0°. Arc length and energies given in MeV, angles given in degrees.

D

Detector Efficiency Tabulations

Tables D.1 to D.4 show the neutron detection absolute efficiencies for four of the detectors used in the breakup cross-section measurement.

Energy	Efficiency	$\Delta\epsilon$	Energy	Efficiency	$\Delta\epsilon$	Energy	Efficiency	$\Delta\epsilon$
0.70	0.02026	0.04818	2.50	0.40980	0.00311	4.75	0.33340	0.00409
0.80	0.04300	0.01876	2.60	0.40651	0.00322	5.00	0.32197	0.00431
0.90	0.10919	0.00691	2.70	0.40417	0.00335	5.25	0.31550	0.00496
1.00	0.17884	0.00452	2.80	0.40127	0.00336	5.50	0.30550	0.00527
1.10	0.24924	0.00349	2.90	0.39423	0.00356	5.75	0.29822	0.00586
1.20	0.31099	0.00298	3.00	0.39518	0.00355	6.00	0.28766	0.00629
1.30	0.35017	0.00284	3.10	0.39479	0.00376	6.25	0.27813	0.00714
1.40	0.37652	0.00270	3.20	0.39375	0.00378	6.50	0.28164	0.00786
1.50	0.39253	0.00270	3.30	0.38490	0.00384	6.75	0.27298	0.00789
1.60	0.40642	0.00267	3.40	0.38045	0.00413	7.00	0.26632	0.00975
1.70	0.41204	0.00267	3.50	0.37749	0.00418	7.25	0.25966	0.00974
1.80	0.41722	0.00270	3.60	0.37482	0.00451	7.50	0.26044	0.01103
1.90	0.41580	0.00278	3.70	0.36954	0.00456	7.75	0.25247	0.01184
2.00	0.41662	0.00278	3.80	0.36536	0.00461	8.00	0.24078	0.01141
2.10	0.41298	0.00283	3.90	0.36443	0.00504	8.50	0.23466	0.01145
2.20	0.41379	0.00296	4.00	0.36216	0.00378	9.00	0.23669	0.01276
2.30	0.41243	0.00292	4.25	0.35681	0.00334	9.50	0.23700	0.01631
2.40	0.41550	0.00309	4.25	0.35681	0.00334			

Table D.1: Absolute neutron detection efficiency for detector R1 with pulse-height threshold of $\frac{1}{4}$ x Cs. Errors are statistical only.

Energy	Efficiency	$\Delta\epsilon$	Energy	Efficiency	$\Delta\epsilon$
0.70	0.02152	0.06086	3.40	0.38356	0.00535
0.80	0.06469	0.01707	3.50	0.37433	0.00543
0.90	0.13144	0.00782	3.60	0.37696	0.00578
1.00	0.20327	0.00537	3.70	0.36544	0.00594
1.10	0.27460	0.00425	3.80	0.36040	0.00605
1.20	0.32595	0.00378	3.90	0.36330	0.00653
1.30	0.35517	0.00365	4.00	0.36447	0.00486
1.40	0.37537	0.00351	4.25	0.35365	0.00435
1.50	0.39036	0.00356	4.50	0.34359	0.00486
1.60	0.40504	0.00345	4.75	0.33053	0.00530
1.70	0.40804	0.00347	5.00	0.32646	0.00553
1.80	0.41684	0.00351	5.25	0.31619	0.00643
1.90	0.41612	0.00362	5.50	0.30529	0.00681
2.00	0.41889	0.00363	5.75	0.30319	0.00750
2.10	0.41185	0.00369	6.00	0.29969	0.00790
2.20	0.41513	0.00385	6.25	0.28748	0.00905
2.30	0.41516	0.00381	6.50	0.28131	0.01023
2.40	0.41123	0.00407	6.75	0.28389	0.01003
2.50	0.40821	0.00407	7.00	0.27811	0.01235
2.60	0.40979	0.00418	7.25	0.27626	0.01206
2.70	0.40467	0.00438	7.50	0.26698	0.01403
2.80	0.40194	0.00438	7.75	0.25595	0.01500
2.90	0.38716	0.00471	8.00	0.24561	0.01448
3.00	0.39262	0.00465	8.50	0.24923	0.01398
3.10	0.39454	0.00489	9.00	0.24122	0.01631
3.20	0.39141	0.00491	9.50	0.24173	0.02059
3.30	0.38154	0.00500			

Table D.2: Absolute neutron detection efficiency for detector R3 with pulse-height threshold of $\frac{1}{4}$ x Cs. Errors are statistical only.

Energy	Efficiency	$\Delta\epsilon$	Energy	Efficiency	$\Delta\epsilon$
0.70	0.02149	0.04985	3.40	0.37998	0.00386
0.80	0.06765	0.01220	3.50	0.37590	0.00389
0.90	0.13882	0.00556	3.60	0.37069	0.00423
1.00	0.21562	0.00383	3.70	0.36914	0.00423
1.10	0.28100	0.00307	3.80	0.36087	0.00434
1.20	0.32894	0.00275	3.90	0.35912	0.00474
1.30	0.36430	0.00262	4.00	0.35816	0.00355
1.40	0.38241	0.00252	4.25	0.35236	0.00314
1.50	0.39766	0.00253	4.50	0.34246	0.00350
1.60	0.40699	0.00250	4.75	0.33149	0.00382
1.70	0.41229	0.00251	5.00	0.32253	0.00403
1.80	0.41417	0.00255	5.25	0.31249	0.00464
1.90	0.41525	0.00261	5.50	0.30554	0.00492
2.00	0.41578	0.00261	5.75	0.29928	0.00538
2.10	0.41208	0.00265	6.00	0.29344	0.00576
2.20	0.41423	0.00276	6.25	0.28411	0.00651
2.30	0.41131	0.00273	6.50	0.28283	0.00731
2.40	0.41046	0.00292	6.75	0.27127	0.00734
2.50	0.40699	0.00291	7.00	0.26798	0.00921
2.60	0.40416	0.00300	7.25	0.26189	0.00909
2.70	0.40055	0.00315	7.50	0.25761	0.01049
2.80	0.40051	0.00313	7.75	0.25418	0.01120
2.90	0.38839	0.00335	8.00	0.24657	0.01040
3.00	0.39299	0.00333	8.50	0.24591	0.01031
3.10	0.38988	0.00355	9.00	0.23849	0.01227
3.20	0.38891	0.00358	9.50	0.23853	0.01552
3.30	0.38724	0.00357			

Table D.3: Absolute neutron detection efficiency for detector L1 with pulse-height threshold of $\frac{1}{4}$ x Cs. Errors are statistical only.

Energy	Efficiency	$\Delta\epsilon$	Energy	Efficiency	$\Delta\epsilon$
0.70	0.02577	0.06568	3.40	0.38363	0.00714
0.80	0.05849	0.02179	3.50	0.37902	0.00726
0.90	0.12651	0.00981	3.60	0.37684	0.00777
1.00	0.19759	0.00697	3.70	0.36764	0.00799
1.10	0.26558	0.00560	3.80	0.35808	0.00816
1.20	0.31791	0.00500	3.90	0.36027	0.00881
1.30	0.35631	0.00478	4.00	0.36312	0.00659
1.40	0.37710	0.00462	4.25	0.36222	0.00577
1.50	0.39710	0.00460	4.50	0.34417	0.00655
1.60	0.40859	0.00456	4.75	0.33727	0.00707
1.70	0.40962	0.00461	5.00	0.32408	0.00749
1.80	0.41274	0.00469	5.25	0.31302	0.00870
1.90	0.41487	0.00480	5.50	0.30955	0.00916
2.00	0.41607	0.00481	5.75	0.30355	0.01020
2.10	0.41375	0.00489	6.00	0.29488	0.01078
2.20	0.41137	0.00515	6.25	0.27577	0.01244
2.30	0.41131	0.00507	6.50	0.27700	0.01392
2.40	0.40944	0.00541	6.75	0.27358	0.01380
2.50	0.41275	0.00537	7.00	0.26511	0.01704
2.60	0.40472	0.00560	7.25	0.26310	0.01682
2.70	0.40166	0.00586	7.50	0.26792	0.01891
2.80	0.39869	0.00586	7.75	0.25181	0.02083
2.90	0.39199	0.00621	8.00	0.24452	0.01974
3.00	0.39603	0.00618	8.50	0.23244	0.02004
3.10	0.39602	0.00654	9.00	0.24911	0.02191
3.20	0.39137	0.00660	9.50	0.23242	0.02928
3.30	0.38556	0.00669			

Table D.4: Absolute neutron detection efficiency for detector L3 with pulse-height threshold of $\frac{1}{4}$ x Cs. Errors are statistical only.

Energy	Efficiency	$\Delta\epsilon$	Energy	Efficiency	$\Delta\epsilon$
0.70	0.01267	0.00109	3.70	0.33398	0.00196
0.80	0.01044	0.00096	3.80	0.33247	0.00197
0.90	0.00873	0.00083	3.90	0.33304	0.00215
1.00	0.00871	0.00083	4.00	0.33200	0.00160
1.10	0.00778	0.00071	4.25	0.33067	0.00140
1.20	0.01293	0.00051	4.50	0.32195	0.00152
1.30	0.04301	0.00059	4.75	0.31294	0.00162
1.40	0.08331	0.00066	5.00	0.30304	0.00165
1.50	0.12602	0.00078	5.25	0.29863	0.00187
1.60	0.16975	0.00088	5.50	0.28923	0.00192
1.70	0.21044	0.00098	5.75	0.28078	0.00208
1.80	0.24801	0.00107	6.00	0.27068	0.00214
1.90	0.27145	0.00115	6.25	0.26138	0.00235
2.00	0.29196	0.00119	6.50	0.26660	0.00263
2.10	0.30641	0.00123	6.75	0.26091	0.00257
2.20	0.31892	0.00132	7.00	0.25415	0.00311
2.30	0.32692	0.00131	7.25	0.24895	0.00303
2.40	0.33625	0.00142	7.50	0.25122	0.00345
2.50	0.33872	0.00142	7.75	0.24215	0.00360
2.60	0.34004	0.00146	8.00	0.23390	0.00332
2.70	0.34232	0.00153	8.50	0.22510	0.00324
2.80	0.34309	0.00153	9.00	0.22474	0.00361
2.90	0.34223	0.00160	9.50	0.21965	0.00460
3.00	0.34394	0.00160	10.00	0.21328	0.00515
3.10	0.34553	0.00170	10.50	0.20817	0.00586
3.20	0.34660	0.00171	11.00	0.19719	0.00689
3.30	0.34167	0.00171	11.50	0.19324	0.00876
3.40	0.33998	0.00181	12.00	0.19939	0.01006
3.50	0.33773	0.00183	12.50	0.17596	0.01174
3.60	0.33714	0.00197			

Table D.5: Absolute neutron detection efficiency for detector R1 with pulse-height threshold of $\frac{1}{2}$ x Cs. Errors are statistical only.

Energy	Efficiency	$\Delta\epsilon$	Energy	Efficiency	$\Delta\epsilon$
0.70	0.01416	0.00194	3.70	0.32752	0.00246
0.80	0.01004	0.00168	3.80	0.32513	0.00247
0.90	0.00916	0.00148	3.90	0.32906	0.00270
1.00	0.00794	0.00116	4.00	0.33072	0.00202
1.10	0.01063	0.00094	4.25	0.32356	0.00177
1.20	0.02766	0.00079	4.50	0.31769	0.00192
1.30	0.06012	0.00080	4.75	0.30652	0.00202
1.40	0.10289	0.00091	5.00	0.30470	0.00210
1.50	0.14646	0.00107	5.25	0.29591	0.00236
1.60	0.18858	0.00117	5.50	0.28563	0.00241
1.70	0.22562	0.00128	5.75	0.28151	0.00264
1.80	0.26061	0.00139	6.00	0.27605	0.00273
1.90	0.28459	0.00150	6.25	0.26738	0.00301
2.00	0.30194	0.00154	6.50	0.26413	0.00334
2.10	0.31016	0.00158	6.75	0.26649	0.00332
2.20	0.32470	0.00169	7.00	0.26313	0.00401
2.30	0.33242	0.00170	7.25	0.25958	0.00389
2.40	0.33678	0.00181	7.50	0.25285	0.00441
2.50	0.33787	0.00181	7.75	0.24174	0.00449
2.60	0.34243	0.00188	8.00	0.23409	0.00417
2.70	0.34159	0.00195	8.50	0.23500	0.00411
2.80	0.34192	0.00194	9.00	0.22823	0.00461
2.90	0.33115	0.00202	9.50	0.22415	0.00577
3.00	0.33947	0.00203	10.00	0.24125	0.00676
3.10	0.34314	0.00216	10.50	0.21588	0.00774
3.20	0.34129	0.00215	11.00	0.20919	0.00909
3.30	0.33660	0.00214	11.50	0.21707	0.01222
3.40	0.33929	0.00231	12.00	0.19251	0.01330
3.50	0.33275	0.00230	12.50	0.19818	0.01636
3.60	0.33534	0.00247			

Table D.6: Absolute neutron detection efficiency for detector R3 with pulse-height threshold of $\frac{1}{2}$ x Cs. Errors are statistical only.

Energy	Efficiency	$\Delta\epsilon$	Energy	Efficiency	$\Delta\epsilon$
0.70	0.01107	0.00161	3.70	0.33185	0.00179
0.80	0.01100	0.00140	3.80	0.32488	0.00180
0.90	0.00904	0.00109	3.90	0.32535	0.00196
1.00	0.00864	0.00090	4.00	0.32782	0.00146
1.10	0.00700	0.00060	4.25	0.32437	0.00128
1.20	0.02557	0.00060	4.50	0.31695	0.00139
1.30	0.06269	0.00061	4.75	0.30967	0.00148
1.40	0.10392	0.00067	5.00	0.30238	0.00152
1.50	0.14754	0.00079	5.25	0.29375	0.00169
1.60	0.19102	0.00086	5.50	0.28704	0.00175
1.70	0.22925	0.00094	5.75	0.27914	0.00188
1.80	0.26037	0.00102	6.00	0.27252	0.00197
1.90	0.28236	0.00108	6.25	0.26375	0.00216
2.00	0.29998	0.00112	6.50	0.26557	0.00240
2.10	0.30871	0.00115	6.75	0.25588	0.00234
2.20	0.32378	0.00122	7.00	0.25326	0.00288
2.30	0.32859	0.00121	7.25	0.24986	0.00278
2.40	0.33455	0.00131	7.50	0.24524	0.00317
2.50	0.33732	0.00130	7.75	0.24116	0.00335
2.60	0.33881	0.00134	8.00	0.23387	0.00305
2.70	0.33912	0.00140	8.50	0.23292	0.00301
2.80	0.34063	0.00140	9.00	0.22212	0.00334
2.90	0.33270	0.00146	9.50	0.22544	0.00419
3.00	0.34143	0.00148	10.00	0.22384	0.00490
3.10	0.34078	0.00156	10.50	0.21422	0.00584
3.20	0.34138	0.00157	11.00	0.20975	0.00660
3.30	0.34258	0.00156	11.50	0.20092	0.00906
3.40	0.33667	0.00167	12.00	0.20787	0.01063
3.50	0.33398	0.00167	12.50	0.24126	0.01252
3.60	0.33180	0.00180			

Table D.7: Absolute neutron detection efficiency for detector L1 with pulse-height threshold of $\frac{1}{2}$ x Cs. Errors are statistical only.

Energy	Efficiency	$\Delta\epsilon$	Energy	Efficiency	$\Delta\epsilon$
0.70	0.01469	0.00184	3.70	0.32382	0.00325
0.80	0.01147	0.00171	3.80	0.31635	0.00323
0.90	0.01040	0.00139	3.90	0.31956	0.00352
1.00	0.00642	0.00125	4.00	0.32476	0.00266
1.10	0.00829	0.00093	4.25	0.32632	0.00233
1.20	0.01928	0.00082	4.50	0.31209	0.00253
1.30	0.05334	0.00093	4.75	0.30886	0.00268
1.40	0.09253	0.00110	5.00	0.29672	0.00274
1.50	0.13830	0.00131	5.25	0.28923	0.00308
1.60	0.17993	0.00148	5.50	0.28429	0.00320
1.70	0.21579	0.00162	5.75	0.27653	0.00347
1.80	0.24751	0.00177	6.00	0.26942	0.00358
1.90	0.26990	0.00189	6.25	0.25341	0.00386
2.00	0.29016	0.00197	6.50	0.25821	0.00437
2.10	0.30175	0.00203	6.75	0.25394	0.00428
2.20	0.31325	0.00217	7.00	0.24627	0.00513
2.30	0.31983	0.00216	7.25	0.24444	0.00502
2.40	0.32488	0.00232	7.50	0.24956	0.00577
2.50	0.33178	0.00234	7.75	0.23677	0.00599
2.60	0.33107	0.00241	8.00	0.23236	0.00551
2.70	0.33347	0.00252	8.50	0.21908	0.00531
2.80	0.33239	0.00251	9.00	0.22619	0.00611
2.90	0.32855	0.00263	9.50	0.21427	0.00764
3.00	0.33575	0.00265	10.00	0.22229	0.00877
3.10	0.33704	0.00281	10.50	0.21528	0.01010
3.20	0.33575	0.00282	11.00	0.22003	0.01262
3.30	0.33190	0.00282	11.50	0.15297	0.01295
3.40	0.33244	0.00300	12.00	0.17639	0.01646
3.50	0.33089	0.00303	12.50	0.18298	0.01902
3.60	0.32875	0.00321			

Table D.8: Absolute neutron detection efficiency for detector L3 with pulse-height threshold of $\frac{1}{2}$ x Cs. Errors are statistical only.

Energy	Efficiency	$\Delta\epsilon$	Energy	Efficiency	$\Delta\epsilon$
0.70	0.00750	0.00078	3.70	0.24484	0.00166
0.80	0.00683	0.00065	3.80	0.24747	0.00168
0.90	0.00562	0.00061	3.90	0.25285	0.00185
1.00	0.00535	0.00063	4.00	0.25653	0.00139
1.10	0.00432	0.00062	4.25	0.26068	0.00122
1.20	0.00319	0.00049	4.50	0.25821	0.00134
1.30	0.00248	0.00043	4.75	0.25624	0.00143
1.40	0.00241	0.00036	5.00	0.25185	0.00148
1.50	0.00202	0.00029	5.25	0.24992	0.00168
1.60	0.00214	0.00031	5.50	0.24518	0.00174
1.70	0.00177	0.00028	5.75	0.23925	0.00189
1.80	0.00323	0.00025	6.00	0.23201	0.00195
1.90	0.00845	0.00033	6.25	0.22360	0.00214
2.00	0.02248	0.00039	6.50	0.22843	0.00240
2.10	0.04494	0.00050	6.75	0.22335	0.00235
2.20	0.06793	0.00062	7.00	0.21736	0.00283
2.30	0.09097	0.00070	7.25	0.21456	0.00276
2.40	0.11478	0.00083	7.50	0.21371	0.00313
2.50	0.13518	0.00088	7.75	0.20878	0.00329
2.60	0.15466	0.00098	8.00	0.20497	0.00307
2.70	0.17162	0.00106	8.50	0.20009	0.00299
2.80	0.18641	0.00111	9.00	0.20053	0.00337
2.90	0.19873	0.00120	9.50	0.19602	0.00427
3.00	0.21308	0.00124	10.00	0.18948	0.00475
3.10	0.22315	0.00134	10.50	0.18353	0.00533
3.20	0.22997	0.00137	11.00	0.17314	0.00636
3.30	0.23201	0.00139	11.50	0.16810	0.00789
3.40	0.23616	0.00149	12.00	0.17573	0.00941
3.50	0.24010	0.00152	12.50	0.14856	0.01045
3.60	0.24347	0.00164			

Table D.9: Absolute neutron detection efficiency for detector R1 with pulse-height threshold of 1 x Cs. Errors are statistical only.

Energy	Efficiency	$\Delta\epsilon$	Energy	Efficiency	$\Delta\epsilon$
0.70	0.00704	0.00118	3.70	0.24513	0.00209
0.80	0.00729	0.00096	3.80	0.24668	0.00213
0.90	0.00710	0.00104	3.90	0.25276	0.00234
1.00	0.00514	0.00091	4.00	0.25769	0.00176
1.10	0.00382	0.00068	4.25	0.25884	0.00155
1.20	0.00318	0.00082	4.50	0.25765	0.00170
1.30	0.00334	0.00059	4.75	0.25331	0.00181
1.40	0.00444	0.00059	5.00	0.25587	0.00189
1.50	0.00268	0.00061	5.25	0.25131	0.00215
1.60	0.00203	0.00038	5.50	0.24436	0.00220
1.70	0.00316	0.00041	5.75	0.24248	0.00240
1.80	0.00539	0.00037	6.00	0.23657	0.00250
1.90	0.01890	0.00052	6.25	0.22800	0.00273
2.00	0.04012	0.00062	6.50	0.22904	0.00306
2.10	0.06304	0.00073	6.75	0.23324	0.00305
2.20	0.08855	0.00089	7.00	0.22811	0.00369
2.30	0.11192	0.00098	7.25	0.22433	0.00355
2.40	0.13549	0.00113	7.50	0.21946	0.00401
2.50	0.15481	0.00120	7.75	0.20968	0.00414
2.60	0.17331	0.00132	8.00	0.20621	0.00384
2.70	0.18818	0.00142	8.50	0.20664	0.00379
2.80	0.20064	0.00147	9.00	0.20458	0.00433
2.90	0.20641	0.00156	9.50	0.19963	0.00539
3.00	0.22190	0.00162	10.00	0.21054	0.00625
3.10	0.23007	0.00175	10.50	0.19258	0.00717
3.20	0.23541	0.00176	11.00	0.17656	0.00831
3.30	0.23417	0.00177	11.50	0.19321	0.01091
3.40	0.24364	0.00193	12.00	0.15861	0.01165
3.50	0.24400	0.00193	12.50	0.16702	0.01410
3.60	0.24952	0.00209			

Table D.10: Absolute neutron detection efficiency for detector R3 with pulse-height threshold of 1 x Cs. Errors are statistical only.

Energy	Efficiency	$\Delta\epsilon$	Energy	Efficiency	$\Delta\epsilon$
0.70	0.00907	0.00104	3.70	0.24721	0.00151
0.80	0.00613	0.00090	3.80	0.24576	0.00154
0.90	0.00519	0.00075	3.90	0.24816	0.00168
1.00	0.00421	0.00065	4.00	0.25399	0.00126
1.10	0.00345	0.00061	4.25	0.25699	0.00112
1.20	0.00240	0.00054	4.50	0.25633	0.00122
1.30	0.00247	0.00043	4.75	0.25466	0.00131
1.40	0.00230	0.00041	5.00	0.25217	0.00136
1.50	0.00134	0.00046	5.25	0.24673	0.00152
1.60	0.00275	0.00034	5.50	0.24350	0.00159
1.70	0.00303	0.00031	5.75	0.23778	0.00170
1.80	0.00604	0.00031	6.00	0.23200	0.00178
1.90	0.01598	0.00036	6.25	0.22565	0.00196
2.00	0.03464	0.00043	6.50	0.22760	0.00218
2.10	0.05781	0.00052	6.75	0.21968	0.00214
2.20	0.08307	0.00063	7.00	0.21943	0.00259
2.30	0.10567	0.00069	7.25	0.21571	0.00252
2.40	0.12919	0.00080	7.50	0.21296	0.00284
2.50	0.14879	0.00085	7.75	0.21199	0.00304
2.60	0.16742	0.00093	8.00	0.20616	0.00279
2.70	0.18143	0.00101	8.50	0.20409	0.00273
2.80	0.19481	0.00104	9.00	0.19959	0.00304
2.90	0.20260	0.00110	9.50	0.20071	0.00388
3.00	0.21765	0.00115	10.00	0.19533	0.00439
3.10	0.22550	0.00124	10.50	0.19181	0.00512
3.20	0.23133	0.00127	11.00	0.18089	0.00614
3.30	0.23656	0.00128	11.50	0.17681	0.00794
3.40	0.23902	0.00138	12.00	0.17939	0.00951
3.50	0.24049	0.00139	12.50	0.18851	0.01046
3.60	0.24354	0.00151			

Table D.11: Absolute neutron detection efficiency for detector L1 with pulse-height threshold of 1 x Cs. Errors are statistical only.

Energy	Efficiency	$\Delta\epsilon$	Energy	Efficiency	$\Delta\epsilon$
0.70	0.00764	0.00110	3.70	0.23954	0.00274
0.80	0.00726	0.00113	3.80	0.23831	0.00277
0.90	0.00590	0.00100	3.90	0.24064	0.00302
1.00	0.00371	0.00109	4.00	0.25125	0.00231
1.10	0.00541	0.00094	4.25	0.25734	0.00204
1.20	0.00386	0.00084	4.50	0.25000	0.00223
1.30	0.00320	0.00061	4.75	0.25344	0.00239
1.40	0.00417	0.00077	5.00	0.24592	0.00246
1.50	0.00273	0.00059	5.25	0.24279	0.00278
1.60	0.00270	0.00062	5.50	0.24122	0.00290
1.70	0.00221	0.00040	5.75	0.23495	0.00316
1.80	0.00431	0.00044	6.00	0.22956	0.00326
1.90	0.01369	0.00060	6.25	0.21281	0.00349
2.00	0.02966	0.00069	6.50	0.22212	0.00400
2.10	0.05192	0.00088	6.75	0.21680	0.00391
2.20	0.07593	0.00107	7.00	0.21080	0.00467
2.30	0.09647	0.00119	7.25	0.20973	0.00458
2.40	0.11849	0.00139	7.50	0.21500	0.00527
2.50	0.14284	0.00152	7.75	0.20507	0.00548
2.60	0.15928	0.00164	8.00	0.20643	0.00511
2.70	0.17633	0.00181	8.50	0.19566	0.00492
2.80	0.18719	0.00185	9.00	0.19704	0.00564
2.90	0.19131	0.00198	9.50	0.19156	0.00709
3.00	0.21238	0.00208	10.00	0.19621	0.00818
3.10	0.21984	0.00223	10.50	0.18514	0.00932
3.20	0.22525	0.00227	11.00	0.19179	0.01147
3.30	0.22905	0.00231	11.50	0.13102	0.01193
3.40	0.23317	0.00247	12.00	0.16470	0.01525
3.50	0.23641	0.00252	12.50	0.12873	0.01577
3.60	0.23942	0.00270			

Table D.12: Absolute neutron detection efficiency for detector L3 with pulse-height threshold of 1 x Cs. Errors are statistical only.

References

[Alt67] E. O. Alt, P. Grassberger, and W. Sandhas. Nuclear Physics, **B2**(1967) 167.

[Alt94] E. O. Alt and M. Rauh. *How Large Coulomb Effects Are to be Expected in the Proton-Deuteron Breakup Reaction?* In Franz Gross, editor, 14^{th} *International IUPAP Conference on Few Body Problems in Physics*, pages 15–17, 1994.

[Bol87] J. W. Boldeman. *Review of Measurements of the Prompt Fission Neutron Spectrum from the Spontaneous Fission of* ^{252}*Cf.* Technical Report IAEA-TECDOC-410, IAEA, 1987.

[Böt83] R. Böttger, H. Klein, A. Chalupka, and B. Strohmaier. *The Neutron Energy Spectrum from the Spontaneous Fission of* ^{252}*Cf in the Energy Range 2 MeV* $\leq E_n \leq$ *14 MeV.* In K. H. Böckhoff, editor, *Nuclear Data for Science and Technology*, pages 484–487. D. Reidel Publishing Company, 1983.

[Böt90a] R. Böttger, H. Klein, A. Chalupka, and B. Strohmaier. *Investigation of the Spectral Fluence of Neutrons From Spontaneous Fission of* ^{252}*Cf by Means of Time-of-Flight Spectrometry.* Nuclear Science and Engineering, **106**(1990) 377–398.

[Böt90b] R. Böttger, H. Märten, D. Richter, D. Seeliger, W. D. Fromm, and H. Klein. *The* ^{252}*Cf(sf) Neutron Spectrum in the 5- to 20-MeV Energy Range.* Nuclear Science and Engineering, **106**(1990) 353–366.

[Can83] Canberra Industries, Inc., Meriden, Connecticut. *Pulse Shape Discriminator Model 2160A*, 1983.

[Coo79] S. A. Coon, M. D. Scadron, P. C. McNamee, B. R. Barrett, D. W. E. Blatt, and B. H. J. McKellar. *The Two-Pion-Exchange Three-Nucleon Potential and Nuclear Matter.* Nuclear Physics, **A317**(1979) 242–278.

[Cub89] J. Cub, E. Finckh, K. Gebhardt, K. Geissdörfer, R. Lin, J. Strate, and H. Klein. *The Neutron Detector Efficiency of NE213 Detectors Measured by Means of a ^{252}Cf Source.* Nuclear Instruments and Methods, **A274**(1989) 217–221.

[Day81] B. Day. *Three-body correlations in nuclear matter.* Physical Review, **C24**(1981) 1203.

[deT73] R. de Tourreil and D. W. L. Sprung. *Super-Soft-Core Nucleon-Nucleon Interaction with π-, ρ- and ω-exchange Contributions.* Nuclear Physics, **A201**(1973) 193.

[Die82] G. Dietze and H. Klein. *Monte Carlo Codes for the Calculation of Neutron Response Functions and Detection Efficiencies for NE-213 Scintillation Detectors.* Technical Report PTB-ND-22, Physikalisch-Technische Bundesanstalt, 1982.

[Dil71] W. Dilg, L. Koester, and W. Nistler. *The Neutron-Deuteron Scattering Lengths.* Physics Letters, **36B**(1971) 208.

[Dro72] M. Drosg. *Accurate Measurement of the Counting Efficiency of a NE-213 Neutron Detector Between 2 and 26 MeV.* Nuclear Instruments and Methods, **105**(1972) 573–584.

[Dro78] M. Drosg. *Unified Absolute Differential Cross Sections for Neutron Production by the Hydrogen Isotopes for Charged-Particle Energies Between 6 and 17 MeV.* Nuclear Science and Engineering, **67**(1978) 190–220.

[Fad61] L. D. Faddeev. *Scattering Theory for a Three-Particle System.* Soviet Physics JETP, **12**(1961) 1014–1019.

[Fri83] J. L. Friar. *Three Body Forces.* In *AIP Conference Proceedings 97*, pages 378–389. Indiana University, 1983. Proceedings of Conference on the Interaction Between Medium Energy Nucleons in Nuclei.

[Fri90] J. L. Friar, B. F. Gibson, G. Berthold, W. Glöckle, Th. Cornelius, H. Witała, J. Haidenbauer, Y. Koike, G. L. Payne, J. A. Tjon, and W. M. Kloet. *Benchmark Solutions for a Model Three-Nucleon Scattering Problem.* Physical Review C, Nuclear Physics, **42**(1990) 1838–1840.

[Frö87] F. H. Fröhner. *Watt Spectrum Fit to ^{252}Cf Prompt Fission Neutron Data.* In *Proc. IAEA Advisory Group Meeting on Nuclear Theory for Fast Neutron Data Evaluation*, 1987.

[Fur72] M. Furić. *Two-Particle Coincidence Measurements of Four Body Break-up.* Nuclear Instruments and Methods, **98**(1972) 301–307.

[Geb93] K. Gebhardt, W. Jäger, C. Jeitner, M. Vitz, E. Finckh, T. N. Frank, Th. Januschke, W. Sandhas, and H. Haberzettl. *Experimental and theoretical investigation of the $^2H(n,nnp)$ reaction and of the neutron-neutron scattering length.* Nuclear Physics, **A561**(1993) 232–250.

[Gib88] B. F. Gibson and B. H. J. McKellar. *The Three-Body Force in the Trinucleons.* Few-Body Systems, **3**(1988) 143–170. Progress Report.

[Gla74] D. W. Glasgow, D. E. Velkley, J. D. Brandenberger, M. T. McEllistrem, H. J. Hennecke, and D. V. Breitenbecher. *Shielding for Fast Neutron Scattering Experiments of High Sensitivity.* Nuclear Instruments and Methods, **114**(1974) 521–534.

[Glö83] W. Glöckle. *The Quantum Mechanical Few-Body Problem.* Texts and Monographs in Physics. Springer-Verlag, 1983.

[Glö90] W. Glöckle, H. Witała, and Th. Cornelius. *Three Nucleon Scattering - A Test for Nuclear Dynamics.* Nuclear Physics, **A508**(1990) 115c–130c.

[Gou81] C. R. Gould, L. L. Holzsweig, S. E. King, Y. C. Lau, R. V. Poore, N. R. Roberson, and S. A. Wender. *The XSYS Data Acquisition System at Triangle Universities Nuclear Laboratory.* IEEE Transactions in Nuclear Science, **NS-28**(1981) 3708–3714.

[Gro94] R. Großmann, G. Nitzsche, H. Patberg, L. Sydow, S. Vohl, and H. Paetz gen. Schieck. *Comparison of the Breakup Cross Section of Reactions D(p,pp)n and D(n,nn)H at E_{lab} = 10.5 MeV.* In Franz Gross, editor, 14^{th} *International IUPAP Conference on Few Body Problems in Physics*, pages 66–69, 1994.

[Gus82] P. P. Guss. *Elastic and Inelastic Scattering Cross Sections and Analyzing Powers for ^{58}Ni, ^{60}Ni, ^{116}Sn, and ^{120}Sn.* Ph.D. thesis, Duke University, 1982.

[Hon86] G. M. Honoré. *Neutron Scattering Cross Section and Analyzing Power Measurements for ^{40}Ca and ^{89}Y and Comprehensive Optical Model Analyses.* Ph.D. thesis, Duke University, 1986.

[How84] C. R. Howell. *Neutron Scattering from ^{28}Si and ^{32}S: Cross Sections and Analyzing Powers from 8 to 40 MeV.* Ph.D. thesis, Duke University, 1984.

[How88] C. R. Howell, W. Tornow, I. Ŝlaus, P. D. Felsher, M. L. Roberts, H. G. Pfützner, Anli Li, K. Murphy, R. L. Walter, J. M. Lambert, P. A. Treado, H. Witała, W. Glöckle, and T. Cornelius. *Rigorous Calculations and Measurements of $A_y(\theta)$ for n+d Elastic-Scattering and Breakup Processes.* Physical Review Letters, **61**(1988) 1565–1568.

[Hüb93] D. Hüber, H. Witała, and W. Glöckle. *Momentum-Space Calculations for Three-Nucleon Scattering Including a Three-Nucleon Force.* Few-Body Systems, **14**(1993) 171–190.

[Lac80] M. Lacombe, B. Loiseau, J. M. Richard, R. Vinh Mau, and J. Côté. *Parametrization of the Paris N-N Potential.* Physical Review, **C21**(1980) 861.

[Leo92] W. R. Leo. *Techniques for Nuclear and Particle Physics Experiments.* Springer-Verlag, second edition, 1992.

[Mac89] R. Machleidt. *The Meson Theory of Nuclear Forces and Nuclear Structure.* Advances in Nuclear Physics, **19**(1989) 189–376.

[Man87] W. Mannhart. *Status of the ^{252}Cf Fission Neutron Spectrum Evaluation with Regard to Recent Experiments.* Technical Report IAEA-TECDOC-410, IAEA, 1987.

[Mar86] J. Martino. *The Isospin Structure of the 3-Nucleon Form Factors.* In B. L. Berman and B. F. Gibson, editors, *The Three-Body Force in the Three-Nucleon System (Lecture Notes in Physics, Vol 260)*, page 129. Springer, 1986.

[Mei84a] W. Meier. *Berechnung des Neutron-Deuteron-Aufbruchwirkungsquersnittes Unter Einschluss eines Dreinukleonenpotentials.* Ph.D. thesis, Ruhr-Universität Bochum, 1984.

[Mei84b] W. Meier and W. Glöckle. *The neutron induced deuteron break-up process with the inclusion of a three-nucleon force.* Physics Letters, **138B**(1984) 329–332.

[Pat94] H. Patberg, R. Großmann, G. Nitzsche, L. Sydow, S. Vohl, and H. Paetz gen. Schieck. *Study of the Breakup Reaction D(p,pp)n at E_p = 19.0 MeV.* In Franz Gross, editor, 14^{th} *International IUPAP Conference on Few Body Problems in Physics*, pages 145–148, 1994.

[Ped86] R. S. Pedroni. *Cross Sections and Analyzing Powers in the 8-17 MeV Range for Neutron Scattering from $^{54,56}Fe$, $^{58,60}Ni$, ^{93}Nb and ^{120}Sn.* Ph.D. thesis, Duke University, 1986.

[Pic92] A. Picklesimer, R. A. Rice, and R. Brandenburg. *Δ Degrees of Freedom in Trinuclei. V. Exotic Contributions.* Physical Review C, **46**(1992) 1178–1182.

[Poe83] W. P. Poenitz and T. Tamura. *Investigation of the Prompt-Neutron Spectrum for Spontaneously-Fissioning ^{252}Cf*.* In K. H. Böckhoff, editor, *Nuclear Data for Science and Technology*, pages 465–472. D. Reidel Publishing Company, 1983.

[Rau91] G. Rauprich, S. Lemaître, P. Niessen, K. R. Nyga, R. Reckenfelderbäumer, L. Sydow, and H. Paetz gen. Schieck. *Study of the Kinematically Complete*

Breakup Reaction $^2H(\vec{p},pp)n$ *at* E_p = *13.0 MeV with Polarized Protons.* Nuclear Physics, **A535**(1991) 313–330.

[Rei80a] W. L. Reiter and G. Stengl. *A Long Term Stable Reference Light Source using LED's for Stabilization of Scintillation Spectrometers.* Nuclear Instruments and Methods, **173**(1980) 275–282.

[Rei80b] W. L. Reiter and G. Stengl. *A Stabilizing System for Scintillation Spectrometers with a Light Emitting Diode and a PIN Photodiode.* Nuclear Instruments and Methods, **169**(1980) 469–476.

[Rob81] N. R. Roberson and S. E. Edwards. *Interface for the TUNL VAX Data Acquisition Facility.* IEEE Transactions in Nuclear Science, **NS-28**(1981) 3834–3837.

[Sau86] P. U. Sauer. *Many-nucleon Forces and Currents Derived from the Explicit Treatment of* Δ*-isobar and Pion Degrees of Freedom.* In B. L. Berman and B. F. Gibson, editors, *The Three-Body Force in the Three-Nucleon System (Lecture Notes in Physics, Vol 260)*, page 129. Springer, 1986.

[Sil93] Silena: Società Industriale Per L'Elettronica Avanzata, Silena, Spain. *Mod. 4418/V CAMAC 8-Input ADC*, 1993.

[Ste89] M. Stephan, K. Bodek, J. Krug, W. Lübcke, S. Obermanns, H. Rühl, M. Steinke, D. Kamke, H. Witała, Th. Cornelius, and W. Glöckle. *Neutron induced deuteron breakup cross section at 10.3 MeV.* Physical Review C, **39**(1989) 2133–2137.

[Str89] J. Sträte, K. Geissdörfer, R. Lin, W. Bielmeier, J. Cub, A. Ebneth, E. Finckh, K. Friess, G. Fuchs, K. Gebhardt, and S. Schindler. *Differential Cross Section of the* $^2H(n,nnp)$ *Reaction at* E_n*=13 MeV.* Nuclear Physics, **A501**(1989) 51–85.

[Tor86] W. Tornow, W. Arnold, J. Herdtweck, and G. Mertens. *Measurement of the Response of the Deuterated Scintillators NE 232 and NE 230 to Protons and Deuterons.* Nuclear Instruments and Methods, **A244**(1986) 477–482.

[Wei93] G. J. Weisel, 1993. Private Communication.

[Wir84] R. B. Wiringa, R. A. Smith, and T. A. Ainsworth. *Nucleon-Nucleon Potentials with and without $\Delta(1232)$ Degrees of Freedom.* Physical Review, **C29**(1984) 1207.

[Wit88a] H. Witała, Th. Cornelius, and W. Glöckle. *Elastic Scattering and Break-Up Processes in the* n-d *System.* Few-Body Systems, **3**(1988) 123–134.

[Wit88b] H. Witała, Th. Cornelius, and W. Glöckle. *Faddeev Calculations with Meson-Exchange N-N Interactions for the* n-d *Break-up Process.* Few-Body Systems, **5**(1988) 89–105.

[Wit89a] H. Witała, W. Glöckle, and Th. Cornelius. *Nucleon-induced deuteron breakup: Analysis of 14.1 MeV data by rigorous Faddeev calculations with meson-exchange NN interactions.* Physical Review C, **39**(1989) 384–390.

[Wit89b] H. Witała, W. Glöckle, and Th. Cornelius. *Rigorous Faddeev Calculations for Elastic Neutron-Deuteron Scattering Around 8 MeV c.m. Energy.* Nuclear Physics, **A491**(1989) 157.

Biography

Henry Rossignol Setze III

Personal

Born in New Orleans, Louisiana, November 2, 1959

Education

B.S. Physics, University of Alabama at Birmingham,
Birmingham, Alabama, 1988
A.M. Physics, Duke University, Durham, North Carolina, 1991

Academic Positions

Teaching Assistant, UAB, 1987–1988
Teaching Assistant, Duke University, 1988–1990
Research Assistant, Duke University, 1990–1994

Memberships

American Physical Society

Publications

T. J. Wdowiak, L. D. Brasher, E. L. Robinson, G. C. Flickinger, and H. R. Setze. *Formation of particulates by ion bombardment of cryogenic ice mixtures.* In E. Bussoletti, C. Fusco and G. Longo, editors, *Experiments on Cosmic Dust Analogues.* Kluwer, Dordrecht, 1988.

H. R. Setze, C. R. Howell, R. T. Braun, D. E. González Trotter, A. H. Hussein, C. D. Roper, F. Salinas, I. Ŝlaus, W. Tornow, B. Vlahovic, R. L. Walter, G. Mertens, J. M. Lambert, H. Witała. *Cross-Section Measurements of the Space-Star Configuration in n-d Breakup at 13.0 MeV.* In F. Gross, editor, 14^{th} *International IUPAP Conference on Few Body Problems in Physics.* 1994.

R. T. Braun, W. Tornow, D. E. González Trotter, C. R. Howell, C. D. Roper, F. Salinas, H. R. Setze, R. L. Walter. *Neutron-Proton Analyzing Power at 12 MeV and charged πNN Coupling Constant.* In F. Gross, editor, 14^{th} *International IUPAP Conference on Few Body Problems in Physics.* 1994.

C. R. Howell, W. Tornow, H. R. Setze, R. T. Braun, D. E. González Trotter, C. D. Roper, R. S. Pedroni, S. M. Grimes, C. E. Brient, N. Al-Niemi, F. C. Goeckner. *Resolution of Discrepancy Between Backward Angle Cross-Section Data for Neutron-Deuteron Elastic Scattering*, Few-Body Systems **16**, 127-142, 1994.